Optical singularities and nonlinear effects near plasmonic nanostructures

Anouk Karlijn de Hoogh

Optical singularities and nonlinear effects near plasmonic nanostructures

Proefschrift

ter verkrijging van de graad van doctor
aan de Technische Universiteit Delft,
op gezag van de Rector Magnificus prof. ir. K.C.A.M. Luyben,
voorzitter van het College voor Promoties,
in het openbaar te verdedigen op maandag 12 december 2016 om 12:30 uur

door

Anouk Karlijn DE HOOGH

ingenieur in moleculaire levenswetenschappen,
Universiteit Wageningen
geboren te Naaldwijk, Nederland.

Dit proefschrift is goedgekeurd door de

promotor: prof. dr. L. Kuipers

Samenstelling promotiecommissie:

Rector Magnificus,	voorzitter
Prof. dr. L. Kuipers,	Technische Universiteit Delft
Onafhankelijke leden:	
Prof. dr. Y.M. Blanter,	Technische Universiteit Delft
Prof. dr. J. Gómez Rivas,	Technische Universiteit Eindhoven
Prof. dr. H.P. Urbach,	Technische Universiteit Delft
Prof. dr. ir. H.S.J. van der Zant,	Technische Universiteit Delft
Overige leden:	
Dr. N. Rotenberg,	Max Planck Institute for the Science of Light, Erlangen, Duitsland

This research is part of the research program of the
"Stichting Fundamenteel Onderzoek der Materie" (FOM),
which is financially supported by the
"Nederlandse Organisatie voor Wetenschappelijk Onderzoek" (NWO).

This work was carried out at:
NanoOptics Group,
FOM-Institute for Atomic and Molecular Physics (AMOLF)
Science Park 104, 1098 XG Amsterdam, The Netherlands,
where a limited number of copies of this thesis is available.

Printed by: Ipskamp drukkers, Enschede

Cover: Artistic impression of surface plasmon polaritons scattering from a subwavelength hole and calculated field maps above the structure, indicating singularities.

ISBN 978-94-92323-12-5

An electronic version of this dissertation is available at
http://repository.tudelft.nl/dissertations

Voor mijn ouders

If you're not prepared to be wrong, you'll never come up with anything original.
Sir Ken Robinson

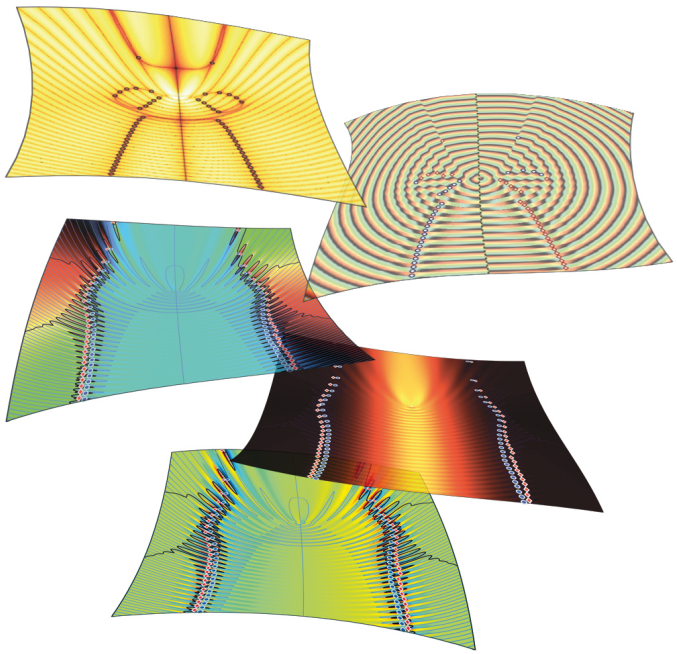

Contents

Chapter 1

Introduction

1.1 Active control of structured light

Control of light has been advantageous to humankind since antiquity [1]. While archeological findings indicate the use of lens-shaped elements, such as rock crystals, already millenia before Christ [2], the earliest written evidence of "a burning glass" dates back to ancient Greece. A famous myth stems from 212 BC [3], when Archimedes was speculated to have protected his home city Syracuse, using multiple hexagonal mirrors to focus the sun's rays to set fire to attacking Roman ships. Supposedly, he actively and dynamically controlled the location of the focus by mechanically rotating his sun reflecting mirrors, so as to set on fire a chosen Roman ship. Whether or not Archimedes could have used mirrors to destroy an entire wooden ship about 50 meters from the coast, the technology of creating fire using optical lenses or mirrors was all but a myth [2]. In ancient times it was used to cauterize wounds and light sacred fires in temples [4]. Since then, we have manipulated light also in other ways through its interaction with material [5]. Using advanced shaped lenses and mirrors in telescopes, microscopes or other equipment, we have extended the range of our own visual perception [6, 7].

In modern times the ability to actively control light has enabled a large number of technologies, crucial for today's society. Light-based technologies include data transport over the internet through optical fibers [8], obtaining energy from sunlight [9], advances in medical treatment and analysis tools [10], and the creation of artificial (sustainable) light-sources [11]. These everyday applications have established a clear concept that actively controlling light opens new pathways for innovations in science and technology. One major way to manipulate and structure light is to use the properties of materials to control light through light-matter interactions [5]. Until recently it was considered that the smallest scale to which light could be controlled was determined by the wavelength of light in naturally occurring materials [12], implying

therefore also a limitation in the precision of light-based technologies. The creation of artificial materials, by structuring materials with subwavelength features, allowed researchers to control the properties of light beyond the wavelength limitation, giving rise to the field of nanophotonics [13].

Whereas properties of light (e.g. amplitude and phase) in normal beams vary gradually in space on a lengthscale given by the wavelength, around nanostructures such properties can vary over length scales smaller than this [14, 15]. Furthermore, the light fields can be much richer in structure and can exhibit fascinating patterns, of which Airy beams [16] or knotted light fields [17, 18] are but examples. Structured light can act as a platform for interesting phenomena on unthinkably small length scales, such as enhancing the emission of fluorescent molecules with nanoantennas [19], focusing optical energy onto a nanosized particle [20] or even slowing down light in photonic crystals [21]. The direction of light fields, typically denoted as the polarization, is another property of light which can be influenced in the vicinity of nanostructures. Local areas can occur in structured light where the polarization is perfectly circular, either left- or right-handed [22]. By positioning light emitting objects with a given handedness in the vicinity of such regions, their emission direction can be controlled [23]. Structured light can also act as a local boost for nonlinear effects, hereby creating a confined source for new light frequencies [24].

One promising platform to create structured light is the field of plasmonics, where the optical properties of metal nanostructures can be exploited to achieve control of light. Plasmonic structures are famous for their ability to confine light to deep subwavelength volumes [25]. Such confinement goes hand-in-hand with increased light intensities, which are known to enhance the effective nonlinear response [24]. Likewise, on such confined length scales, light can be expected to contain more highly structured optical features, such as optical vortices [26] or other kinds of optical singularities [27, 28].

1.2 Wave singularities

Waves are found all throughout nature, of which ocean, sound and light waves are only examples. Such waves, whether being of electromagnetic (e.g. light, x-ray, microwave) or mechanical (water, sound) origin, can interfere constructively, where wave fields from different contributions (sources, reflections, diffracted waves) are added, or destructively where they cancel out. Waves are described with a variety of parameters, which, under certain conditions can become undefined (singular) at a position in space: a wave singularity [29]. A well-known example of such a phenomenon in light fields is the occurrence of caustics, lines along which rays of light are focused, which are often observed at the bottom of the swimming pool. Caustics are a classic singular example because its brightness is predicted to be infinite, and no clear direction of propagation is defined [15]. Vortices, another kind of singularity, occur at points of pure darkness, where the phase is undefined [30]. Singularities can occur as a result of wave interference. Vortices, for instance, can be found in the dark zones of laser

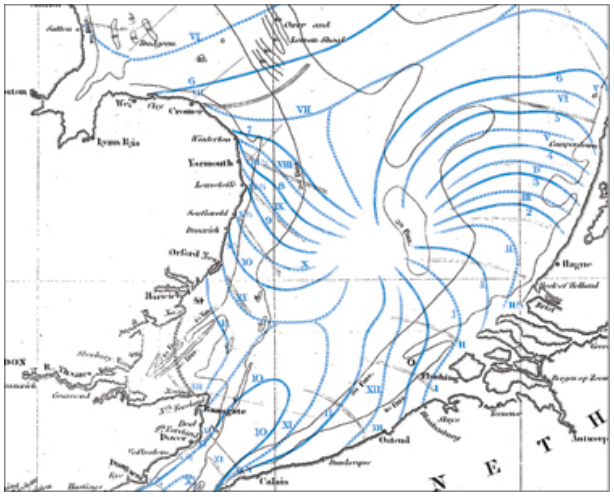

Figure 1.1: Distribution of tides in the North sea, between The Netherlands and England. Along cotidal lines (shown in blue), the tide is simultaneously high at a certain time. Each line therefore represents a different hour on the day, where the amplitude of the wave pattern in the sea is equal. Image with permission taken from [33].

speckles [31, 32].

Another example of a wave singularity was discovered already in the 1830s by William Whewell on ocean and sea waves [34]. Studying how the heights of the tides varied at different positions and times, he drew maps with different lines of equal tides at a certain hour, which he named cotidal lines. Along such lines, the height of the sea is equal and each line represents a different time during the day, e.g. each hour in a 12-hour period (Fig. 1.1). Whewell understood that the complexity of the pattern he observed, was due to the interference of waves following different routes to reach the same point in the ocean or sea. He made a peculiar observation when connecting all the lines of equal tide into a single point, where he concluded that the water height is equal at all time and the tide consequently disappears. However, all 360 degrees surrounding this point of undefined tide, all different cotidal lines were found, resulting in rotating tide over time. It appeared that in the North sea, two of such rotary points of undefined tide were found, of which one is shown in Fig. 1.1. Considering that Whewell's cotidal lines are actually contours of the wavefronts of the tide over a 12-hour period, what he discovered was the first example of a phase singularity.

Phase singularities in optics

Similar field patterns to Whewell's maps can be observed also in optics where the electric (or magnetic) field can exhibit phase singularities. In a scalar description the

electric field can be described by a wave, according to

$$\mathbf{E}(\mathbf{r}) = A(\mathbf{r})e^{i(\theta(\mathbf{r}))}, \tag{1.1}$$

with $A(\mathbf{r})$ the amplitude of the wave, and $\theta(\mathbf{r})$ the phase of the wave. A phase singularity, in literature also known as an optical vortex, is a point where $\theta(\mathbf{r})$ is undefined [15]. An undefined phase occurs at a point $\mathbf{r}'$ where the amplitude of the associated field $A(\mathbf{r}')$ is identically zero. They are generally identified by looking for positions where different lines of constant phase intersect (or in the example of Whewell, intersection of different timelines of equal tide).

Phase singularities can arise in the complicated field patterns of interfering waves. A well-known example of interfering waves is the double-slit experiment, first discovered by Thomas Young in 1801. He used a plane wave to illuminate two slits, hereby creating two sources of cylindrical diffraction. When considering this experiment in two dimensions, the amplitude patterns contain light and dark bands of bright and dim intensity (Fig 1.2a). At the position of the dark bands, the phase jumps along lines, which are called phase dislocations (Fig 1.2b). The addition of a third slit causes a more complex interference pattern. In this scenario, light vanishes at points instead of lines. It is at exactly these positions, that in the phase pattern lines of equal phases meet at single points [14].

At the position of a phase singularity, the phase is undefined. However, close around the singularity, the entire range of phases of 2π is found. The singularity hence carries a topological index s,

$$s = \frac{1}{2\pi} \oint_C d\theta. \tag{1.2}$$

The topological index in Eq. 1.2 is defined as the integer number of rotations that the phase θ undergoes as one traverses a closed path C around the singularity in a counter-clockwise manner [15]. In the close-up of Fig 1.2d, the top singularity can be assigned a topological charge of $s = -1$ as the phase decreases following the loop. Likewise, the bottom singularity carries a topological charge of $s = +1$. In Fig 1.2d, 3 positive and 3 negative singularities are marked by red and blue dots respectively.

The rotary behavior of the tides in the North sea at the singularity, indicates that objects could be rotated around this point. Likewise, optical phase singularities on the nanoscale could potentially be used for nanoparticle movement. Rotating particles around chosen locations and controlling the rotation speed and direction via the topological charge is highly beneficial for new applications in biomedicine [35].

Polarization singularities

In addition to phase singularities, another type of singularity occurs in light fields when its vector nature is taken into account: polarization singularities. Polarization singularities are, by definition, points where a specific parameter that describes the polarization of the light field is degenerate/undefined. There are different types of polarization singularities, which depend on what aspect of the polarization is singular, i.e. the handedness or the orientation of the light [15, 36].

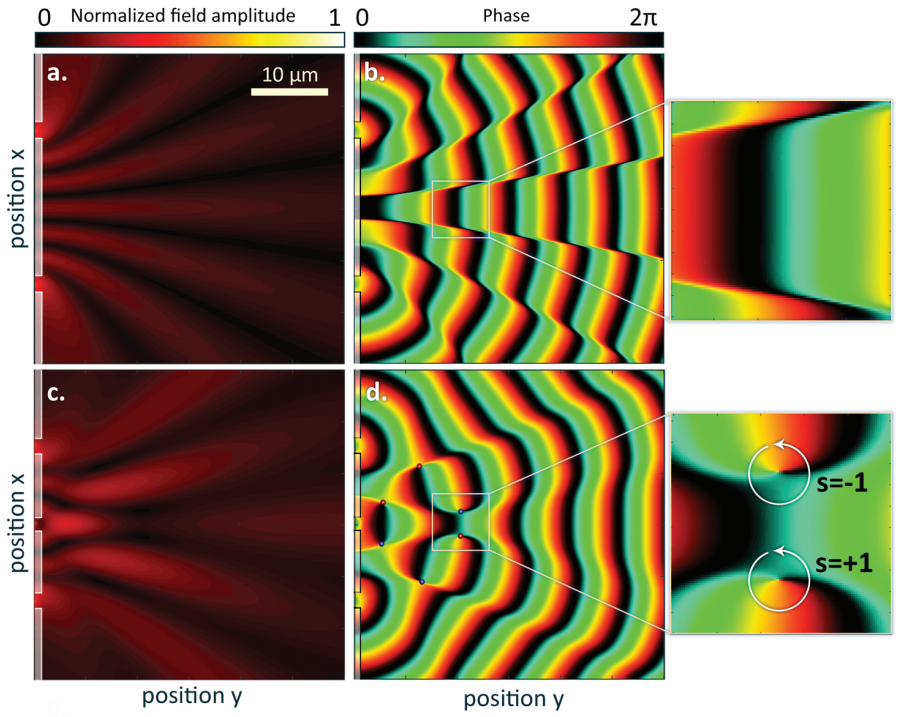

Figure 1.2: The amplitude and the phase of interfering rays of light through 2 (a and b) and 3 (c and d) slits. A close-up of the phase in b. and d. shows 2 distinct phase singularities using 3 slits. The singularities carry a topological charge s of ± 1, where the positive(negative) singularities are marked by red(blue) dots. Wave dislocations can be observed for only 2 slits.

Polarization ellipse

Although polarization singularities are actual properties of the total vector field consisting of three field directions, it is possible to consider polarization singularities within a plane, taking only two components into account [37]. The electric in-plane field components can then be described as [12, 38]:

$$\begin{aligned} E_y &= A_y \cos(\tau + \theta_y), and \\ E_x &= A_x \cos(\tau + \theta_x), \end{aligned} \tag{1.3}$$

where A_i and θ_i are the amplitude and the phase, respectively, of the two components and τ denotes the accumulated phase:

$$\tau = \omega t - \mathbf{kr}. \tag{1.4}$$

Here, ω is the angular frequency, t the time, $\mathbf{k}$ the wavevector and $\mathbf{r}$ the position in space. In order to eliminate τ, Eq. 1.3 can be rewritten as:

$$\begin{aligned} \frac{E_y}{A_y} &= \cos\tau\cos\theta_y - \sin\tau\sin\theta_y, and \\ \frac{E_x}{A_x} &= \cos\tau\cos\theta_x - \sin\tau\sin\theta_x. \end{aligned} \tag{1.5}$$

Which can be rearranged as

$$\begin{aligned} \frac{E_y}{A_y}\sin\theta_x - \frac{E_x}{A_x}\sin\theta_y &= \cos\tau\sin(\theta_x - \theta_y), and \\ \frac{E_y}{A_y}\cos\theta_x - \frac{E_x}{A_x}\cos\theta_y &= \sin\tau\sin(\theta_x - \theta_y). \end{aligned} \tag{1.6}$$

Addition and squaring of the two equations results in an equation of an ellipse:

$$\left(\frac{E_y}{A_y}\right)^2 + \left(\frac{E_x}{A_x}\right)^2 - 2\frac{E_y}{A_y}\frac{E_x}{A_x}\cos\delta = \sin^2\delta, \tag{1.7}$$

where $\delta = \theta_x(r) - \theta_y(r)$ is the phase difference between E_x and E_y respectively at position r. In other words, dependent on the phase difference and the amplitude ratio of the in-plane fields, the vector of the light, at any point, traces out an ellipse as described by Eq. 1.7 and illustrated in Fig. 1.3 (left). As can be seen in the figure, the shape of the polarization ellipse can be described by two angular variables: the ratio between the short and long axis, u/v, which is a measure of the ellipticity ε, and the orientation angle of the ellipse, denoted by α. By applying a coordinate transformation from xy to uv, the equations for ε and α can be derived [12], resulting in:

$$\varepsilon(r) = \tan\left\{\sin^{-1}\left[\sin\left(2\psi(r)\right)\sin\left(\delta(r)\right)\right]/2\right\}, and \tag{1.8}$$

$$\alpha(r) = \left\{\tan^{-1}\left[\tan\left(2\psi(r)\right)\cos\left(\delta(r)\right)\right]/2\right\}, \tag{1.9}$$

where, $\psi(r) = \tan^{-1}\left[A_x(r)/A_y(r)\right]$. Although many combinations of the ellipticity and orientation angle are possible, a few special cases are easily distinguishable, such as when the polarization becomes linear or circular. These special cases will be further discussed in section 1.2.

Poincaré sphere

An alternative way to fully describe all possible polarization states of light fields is the Poincaré sphere [12]. To understand how the different polarization states are represented, we can imagine the Poincaré sphere as a globe (Fig. 1.4). Here, the spherical coordinates are related to the previously described parameters of the

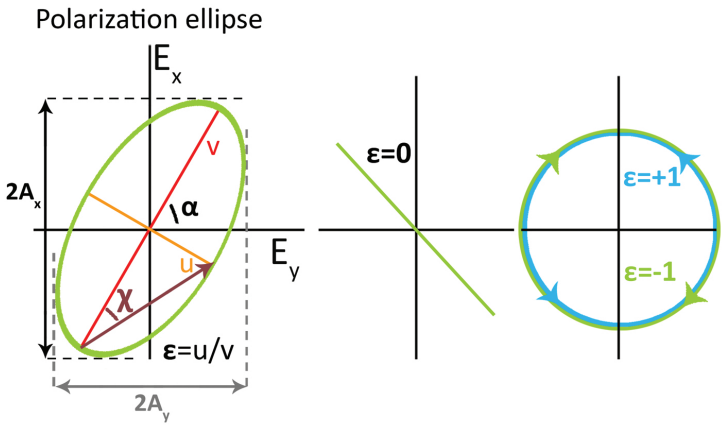

Figure 1.3: Polarization singularities of in-plane electric field components E_x and E_y. At each position in space the electric in-plane components E_x and E_y are described by a polarization ellipse (left). Here, the ellipticity ε is a measure for the shape of the ellipse, and defined as the ratio between the short axis u over the long axis v of the ellipse. When the polarization becomes linear, the handedness of the ellipse becomes undefined, which happens at $\varepsilon = 0$ (middle). The orientation angle α can have any value for linear polarization. For circular polarization, on the other hand, α is undefined (right). The ellipticity is then -1 or 1, where the sign corresponds to right- or left-handed polarization respectively.

polarization ellipse. More specifically, the azimuthal angle is proportional to the orientation angle (exactly 2α), and the polar angle is related to the ellipticity ε (exactly $2\chi = 2arctan(\varepsilon)$). All along the equator ($\chi = 0$) we find linearly polarized light where the ellipticity is 0. The North and the South pole represent left- and right-circularly polarized light ($\varepsilon = +1$ and -1), respectively. In fact, any point on the entire Northern Hemisphere in our coordinate system represents left-handed polarized light (χ is larger than 0, blue half of the globe in Fig. 1.4), and the Southern Hemisphere right-handed polarized light (χ is smaller than 0, red half of the globe in Fig. 1.4). The poles are connected by lines, meridians, along which the ellipticity varies, given by the value of 2χ, while the ellipse orientation remains constant. In addition to meridians, we find latitudes, parallel to the equator. Along those, the ellipticity is constant, but the orientation angle 2α ranges from 0 to π.

In the Poincaré sphere of Fig. 1.4, a chosen polarization state is illustrated with a blue dot on the sphere. The value for 2α can be obtained from the azimuthal angle (horizontal black arrow) with the Cartesian S1-axis and the value for 2χ is given by the polar angle from the equator (vertical orange angle). Additionally, the total in-plane intensity of the light is given by I, the square of the field amplitude, and determines the diameter of the sphere. Note that due to the unconventional way of drawing the polarization ellipse with E_y on the x-axis and E_x on the y-axis, a switch in left-and right-handed light is explained between the Northern and Southern Hemisphere.

By switching from spherical coordinates to Cartesian coordinates it becomes clear

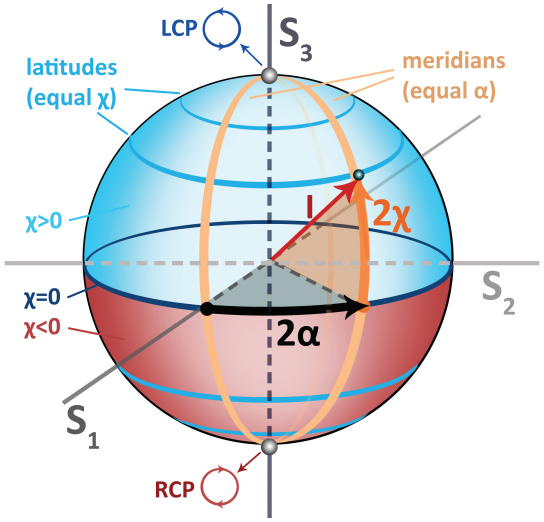

Figure 1.4: The polarization described by the Poincaré sphere using the parameters from the polarization ellipse, ε and α. In Cartesian coordinates, x, y and z are given by the Stokes parameters, S1, S2, and S3 (Eq.1.10). The North and South pole are marked by silver dots, the equator is the dark blue horizontal circle in the middle of the globe and the other latitudes are shown in light blue circles. The equator separates the northern and southern Hemisphere for right- and left-handed polarized light. Two meridians are drawn (vertical yellow circles) along which epsilon varies from -1 (South pole) to 0 (equator) to 1 (North pole), where each meridian represents a single value for α, which is constant all along the meridian. A typical polarization state is illustrated (blue dot), with a certain value for α, ε and intensity I.

that any point on the the Poincaré sphere has Cartesian coordinates given exactly by the Stokes parameters. In terms of the spherical parameters 2χ and 2α, the Stokes parameters are given by:

$$\begin{aligned} S_0 &= I, \\ S_1 &= I\cos 2\chi \cos 2\alpha, \\ S_2 &= I\cos 2\chi \sin 2\alpha, \\ S_3 &= I\sin 2\chi, \end{aligned} \tag{1.10}$$

where S_1, S_2 and S_3 represent the Cartesian x, y and z axes and S_0 represents a normalization parameter related to the total energy in the system.

To complete the picture and connect the Poincaré sphere with the polarization ellipse, it is also possible to describe the Stokes parameters in terms of the original

in-plane fields E_x and E_y, according to:

$$\begin{aligned} S_0 &= A_y^2 + A_x^2, \\ S_1 &= A_y^2 - A_x^2, \\ S_2 &= 2A_y A_x \cos\delta, \\ S_3 &= 2A_y A_x \sin\delta. \end{aligned} \tag{1.11}$$

C-points and L-lines

Polarization singularities are found at positions where either the handedness or the orientation of the polarization ellipse is undefined [15, 36]. The ellipticity of the polarization ellipse, ε (Eq. 1.8), ranges from -1 to $+1$. The sign of ε corresponds to right- and left-circularly polarized light, respectively. When $\varepsilon = 0$, the polarization of light is linear and the handedness is undetermined, which defines one class of polarization singularities, called L-singularities. For those singularities, the in-plane field vector can still have all orientations, but the phase difference $\delta = m\pi$ with m an integer value. As L-singularities in two-dimensional field patterns occur along lines, they are referred to as L-lines.

The orientation of the long axis of the polarization ellipse, α (Eq. 1.9), is measured from the y-axis towards the x-axis, and it ranges from $-\pi/2$ to $\pi/2$. When the orientation of the polarization ellipse α is undefined, we find the second type of singularities, known as a C-point as in two-dimensional field patterns they occur in points. This type of singularity necessarily occurs at positions where the polarization is circular, and the ellipticity $\varepsilon = \pm 1$. Local circular polarization occurs when two conditions are met: the amplitudes $E_x = E_y$ and the phase difference $\delta = \pm\pi/2$.

Analogous to phase singularities, C-points carry a topological charge s, which is defined as

$$s = \frac{1}{2\pi} \oint_C d\alpha. \tag{1.12}$$

The topological charge of a C-point is defined as the number of rotations that the orientation angle α undergoes as one traverses a closed path C around the C-point in a counter-clockwise manner [15]. Because the polarization field is continuous everywhere on the path, the ellipse must return to its original orientation in one full circuit; however, the ellipse orientation is symmetric under 180 degree rotations, giving rise to non-integer indices. Specifically, C-points carry a charge in multiples of $1/2$.

At the nanoscale, the propagation of light waves differs drastically from the paraxial optics approach and plane wave propagation, and often strong gradients of the light field can be found on a spatial scale of less than a free space wavelength. Vector fields near nanostructures can contain all three components of the electric field. In such fields, it is possible to find local positions or areas where the handedness or the orientation of the light becomes undefined.

Recent developments have shown that polarization singularities in nanophotonic structures can be used to direct the emission of quantum dots. In these studies,

entire areas close to C points exhibit left or right handedness that could in turn be used to to control the directionality of emission of quantum dots described by left or right circular dipoles, according to the handedness of the dipole [22, 23]. Moreover, polarization singularities can be used to provide active control over quantum dot properties towards possible photon-spin entanglement [39].

1.3 Nonlinear optics

When light propagates through a medium, the applied electric field **E** polarizes the electrons in the medium within the dipole approximation by inducing a harmonic motion of the electrons. When the motion of the electrons in response to the applied electric force becomes anharmonic (for example, due to high electric fields), then this anharmonic regime can give rise to nonlinear optical effects [40]. The nonlinear response of the medium expands the linear relation between the polarization of a material and the electric field with a Taylor series of anharmonic terms. More specifically, the polarization of a material $P(\omega)$, given in dipole moment per unit volume, is related to the applied electric field $E(\omega)$, following

$$\begin{aligned} P(\omega) &= \epsilon_0 \Big[\chi^{(1)}E(\omega) + \chi^{(2)}(\omega,\omega_1,\omega_2)E(\omega_1)E(\omega_2) \\ &\quad +\chi^{(3)}(\omega,\omega_1,\omega_2,\omega_3)E(\omega_1)E(\omega_2)E(\omega_3) + ...\Big]. \end{aligned} \tag{1.13}$$

where ϵ_0 is the vacuum permittivity. For simplicity a scalar description is used in Eq.1.13. In this equation, $\chi^{(m)}$ is the susceptibility of the order m of a material; a measure of how easily a material's electrons polarize in response to the electric field. In linear optics, a medium is merely characterized by a linear relation between the polarization and the electric field through $P = \epsilon_0\chi^{(1)}E$. This first term in equation 1.13, describing the linear behavior, is provided by the first order susceptibility, $\chi^{(1)}$. In general, when nonlinear terms can be neglected, the linear susceptibility $\chi^{(1)}$, is also used to provide the refractive index n and the permittivity ϵ by $\chi^{(1)} + 1 = n^2 = \epsilon/\epsilon_0 \cdot \mu/\mu_0$, and hence determines many properties of the medium, such as refraction and absorption. Nonlinear responses, based on higher order susceptibilities, can give rise to a host of interesting optical phenomena, such as wave-mixing effects which, in turn, lead to frequency conversion.

1.3.1 Second-order nonlinearities

Second-order responses, which arise from $\chi^{(2)}$ nonlinearities, are the lowest order of nonlinear responses. For second-order effects, the polarization equation is determined by the second-order susceptibility. A well known second-order response, which was also the first nonlinear process to be demonstrated in optics, is second-harmonic generation (SHG) which can be described by

$$P(2\omega) = \epsilon_0\chi^{(2)}E(\omega)^2. \tag{1.14}$$

Its discovery dates back to 1961 by Peter Franken [41], shortly after the construction of the first laser by Theodore H. Maiman [42]. In this process, the frequency ω of a monochromatic wave is converted by frequency-doubling to its second harmonic at 2ω, illustrated in Fig. 1.5, initially observed by shining the output of a ruby laser into a quartz sample.

Another nonlinear process, caused by the second-order susceptibility, is spontaneous parametric downconversion. Here, light traveling through a nonlinear material with a frequency of ω_1, is split into a pair of beams with frequencies ω_2 and ω_3, whereby the law of energy-conservation is maintained via $\omega_1 = \omega_2 + \omega_3$. Multiple solutions for energy-conservation are possible (see Fig. 1.5), forming entangled wave-pairs [43] with coupled directions and frequencies ω_2 and ω_3.

As Eq. 1.14 shows, the polarization for second-harmonic generation depends quadratically on the applied electric field. This has immediate consequences for the potential of this nonlinear effect to occur in a specific medium. Certain materials have an atomic composition which contain inversion symmetry about the center: they are centrosymmetric. As all properties of the material are symmetric, when $E \to -E$, so should $P \to -P$, leading to an additional equation for the polarization

$$-P^{(2)} = \epsilon_0 \chi^{(2)}(-E)^2 = \epsilon_0 \chi^{(2)}(E)^2. \tag{1.15}$$

Both equations, Eq. 1.14 and Eq. 1.15, can only occur, when $\chi^{(2)} = 0$, and consequently no second-harmonic generation could occur, within the dipole approximation. However, when the centrosymmetry is broken, for instance by the material itself (i.e. a non-centrosymmetric material), second-order processes are no longer forbidden. Note also, that in the bulk of centrosymmetric media, second-harmonic generation can occur when quadrupolar interactions are considered.

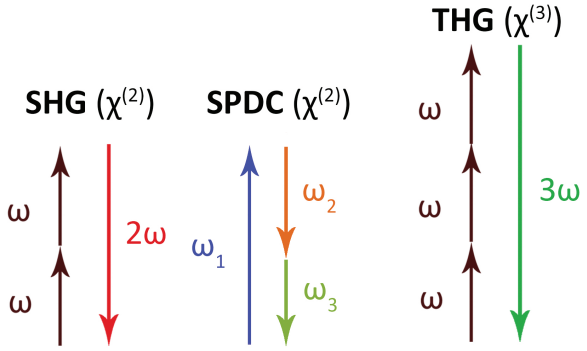

Figure 1.5: Energy level diagrams of three nonlinear processes. Left, second-harmonic generation (SHG), the frequency-doubling of light with a frequency of ω to 2ω. Middle, spontaneous parametric down conversion (SPDC), where light with a frequency of ω_1 splits into light of ω_2 and ω_3. Right, third-harmonic generation (THG), where the incident frequency ω is tripled to 3ω .

1.3.2 Third-order nonlinearities

In centrosymmetric materials, the lowest order nonlinear contribution arises from the third-order nonlinear polarization. Third-order nonlinearities also give rise to new frequencies, where sums and differences of triplets of frequencies are converted. The most basic process, where a monochromatic wave of frequency ω creates a response at a frequency of 3ω, is called third-harmonic generation (see Fig. 1.5). Third-harmonic generation has a cubic dependence on the incident electric field, following:

$$P(3\omega) = \epsilon_0 \chi^{(3)} E(\omega)^3. \tag{1.16}$$

Many other higher-order nonlinear responses exist, but their discussion is beyond the scope of this thesis.

Nonlinear optics at the nanoscale has recently generated enormous interest as a route towards fully integrated nanophotonic devices, which requires active manipulation and control of nanoscale optical signals. Due to the small lengthscales of nanostructures, nonlinear signals are inherently weak as long co-propagation of the fields to generate nonlinear gain is precluded. One way to increase the efficiency of nonlinear processes, is to exploit plasmonic nanostructures, which are known to strongly confine light fields with concomitant high field enhancements.

1.4 Surface plasmon polaritons

1.4.1 Wood's anomalies

The fundamentals of plasmonics, as studied today, finds its origin more than one century ago. When studying the spectral patterns of an incandescent lamp reflected from a metallic grating in 1902, Robert W. Wood made a peculiar observation [44]. When illuminating the periodic grating with p-polarized (TM) light under an angle θ relative to the metallic surface, Wood observed narrow dark bands in the reflection spectra (schematically illustrated in Fig. 1.6). At this stage, an explanation for this phenomenon, called Wood's anomaly, was not found, and it was for long considered a strong disadvantage of gratings.

It was not until the late '50s that the next step in understanding Wood's anomaly was taken by several researchers. An important progression was the theory proposed by David Pines, who related the energy losses experienced by beams passing through metals to collective oscillations of the free electron in the metal, and hence named the energy quantization of these oscillations 'plasmons' [45]. The actual existence of bulk plasmons was proven shortly after by Steinmann [46]. In 1957 Rufus Ritchie then predicted the existence of self-sustained collective oscillations at metal surfaces [47]. Two years later, this was experimentally detected in a series of electron energy-loss experiments by Powell [48]. These experiments firstly explained the combination of matter excitation and electromagnetic waves in what is nowadays known under the name *surface plasmon polariton* (SPP). In hindsight we now realize that Wood was the first to discover the surface plasmon polariton, as light in a narrow spectral

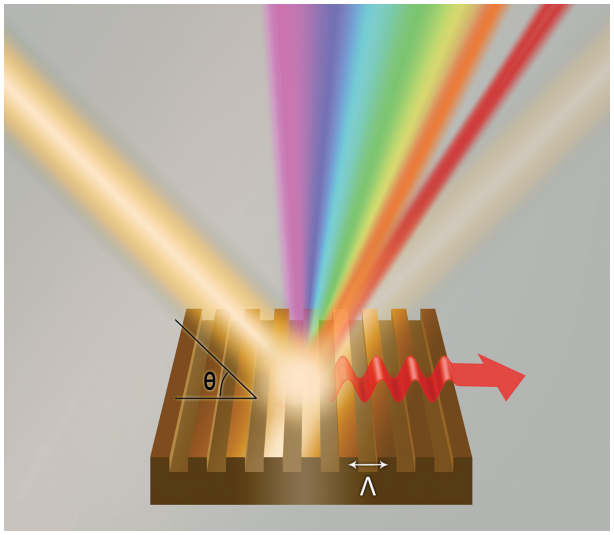

Figure 1.6: Schematic illustration of Wood's anomaly. A beam of white light illuminates a periodic metallic grating. Dependent on the angle of illumination with respect to the grating, a narrow spectral region is missing in the diffraction pattern. The light missing in the diffraction is coupled to a propagating surface plasmon polariton mode.

region in his white-light source that got 'caught' onto the grating surface. Since the first observation of Wood's anomalies over a century ago, the field of plasmonics has transformed into a major research topic in nanophotonics.

1.4.2 Surface plasmon polaritons

Since firstly observed by R. Woods, our ability to couple light fields into surface plasmon polaritons and to control or engineer their properties has largely increased our knowledge of these waves. Surface plasmon polaritons are surface waves propagating at the boundary between a metal and a dielectric, meaning that the electromagnetic fields exponentially decay away from the boundary [25]. A schematic illustration of the electric field lines of the SPP wave is shown in Fig 1.7a. In this illustration, the interface is normal to the z-axis and the propagation direction is taken along the x-axis. SPPs are transverse-magnetic waves, with a magnetic field component H_y transverse to the propagation direction. The electric field predominantly points out-of-the-plain (z) and decays exponentially away from the interface into the metal and the dielectric, as shown in the inset to Fig 1.7a to illustrate the decaying trend general to all field components. SPPs also contain an in-plane electric vector along the propagation direction E_x. While the out-of-plain field is always larger than the in-plane field, the exact ratio of the field amplitudes is dependent on the light frequency and material parameters. For SPPs at a metal-dielectric interface [49] and for a given

light frequency ω, the wavevector k of SPPs propagating in the x-direction is related to the wavevector of the incident light k_0 as:

$$k_x = k'_x + ik''_x = k_0\sqrt{\frac{\epsilon_d\epsilon_m}{\epsilon_d + \epsilon_m}}, \tag{1.17}$$

in which $k_0 = \omega/c$, with c the speed of light in vacuum and the dielectric constants of the dielectric and the metal are given by ϵ_d and ϵ_m, respectively. The out-of-plane wavevector of the SPP can be calculated from requiring the conservation of momentum and is found to be:

$$k_z = k'_z + ik''_z = k_0\sqrt{\frac{\epsilon_d}{\epsilon_d + \epsilon_m}}. \tag{1.18}$$

The dispersion relations of propagating SPPs on a gold-air and a gold-glass interface, resulting from Eq. 1.17, are shown in Fig 1.7b in solid black and aquamarine curves. Real frequencies ω are used to calculate complex wavevectors and the optical properties of gold were taken from literature [50]. The refractive indices for glass and air were taken to be n=1 and n=1.5 respectively. In this graph, the curves represent the real part of the wavevector k'_x. Additionally, the light lines are shown for free-space light traveling through air (dashed black line) and through glass (dashed aquamarine line), which relate the frequency and the wavevector through $\omega = \frac{ck_0}{n_d}$, where $k_0 = 2\pi/\lambda$ and n_d the refractive index of the dielectric. What can be observed in this graph, for both dispersion curves, is that for small frequencies, the dispersion curve lies close to the light line and the SPPs therefore behave photon-like. As the frequency increases, the dispersion curve bends away from the light line, indicating that the SPPs have a higher wavevector than light propagating at the same frequencies. The higher wavevectors result in shorter SPP wavelengths and in a faster decay of the electromagnetic fields away from metal-dielectric boundary. For ideal metals, i.e. without Ohmic losses described by the Drude model the SPP wavevector will tend to increase indefinitely while the frequency approaches the SPP frequency (ω_{SPP}). For the real metal here shown, gold, the wavevector increases for frequencies up to $3.5 \cdot 10^{15} rad/s$, because the imaginary part of the dielectric function of gold above this threshold becomes comparable to the real component and the curve bends back at the ω_{SPP}.

The propagation length ℓ_p of SPPs, the length over which the SPP intensity decays by a factor of 1 over e, is related to the imaginary part of the plasmonic wavevector function in Eq. 1.17, following:

$$\ell_p = \frac{1}{2k''_x}. \tag{1.19}$$

The propagation length decreases with the increasing wavevector of SPPs. This can be intuitively understood by realizing that, as the SPP wavevector increases, more and more of the electromagnetic field resides inside the metal where it is affected by resistive damping. While the strongest field confinements of SPPs are achievable at high frequencies (visible frequencies), the largest propagation lengths are found at low

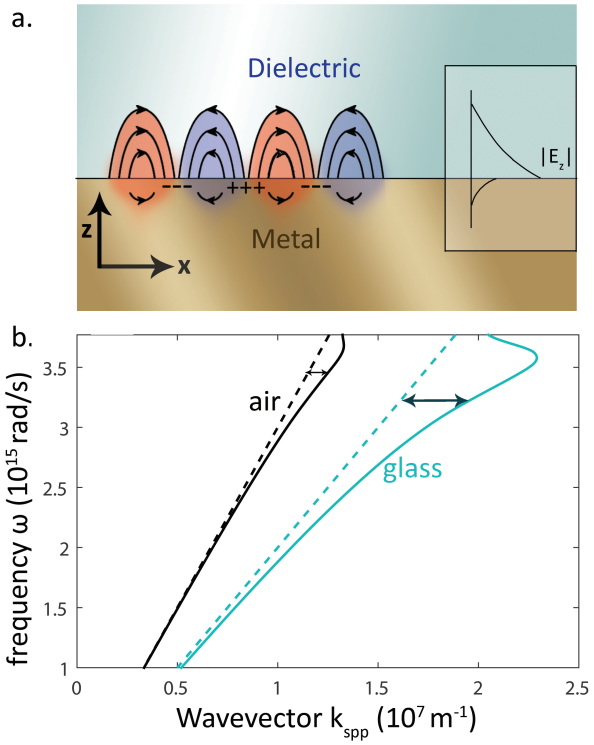

Figure 1.7: (a) Illustration of the propagation of SPPs on a metal-dielectric interface. The electric field orientations are depicted with black lines and arrows. Areas of positive and negative charges are marked by + and - signs near the metal-dielectric interface. The inset shows the decay of the electric amplitude normal to the metal surface, which peaks at the interfaces and decays exponentially into the dielectric and into the metal. (b) The dispersion relation for SPPs are shown in solid lines on an Au-air (black curve) and on an Au-glass (aquamarine curve) interface. The light lines for air and glass are depicted in dashed black and aquamarine lines respectively. The momentum mismatch between the light line and the SPPs are given at chosen frequencies for Au-air SPPs and Au-glass SPPs by black and aquamarine arrows.

frequencies (near-IR and IR frequencies). This fact immediately highlights one of the main challenges in plasmonics, which is to find the best compromise between a high field confinement and a long propagation length.

The momentum mismatch, in Fig 1.7b indicated by the horizontal black and aquamarine arrows, precludes direct excitation of SPPs with free-space light. To couple to the SPP mode, the momentum mismatch has to be bridged. One possible technique is the use of a grating coupler, with a period Λ. For illumination of a grating with incident light with a wavevector k_0 under an angle θ the grating assisted

phasematching to an SPP wave with wavevector k'_x can be written as

$$k'_x = k_0 \sin\theta + mG. \tag{1.20}$$

Here, $G = \frac{2\pi}{\Lambda}$ represents the wavevector of the grating, of which multiples (m integer) can be added or subtracted from the incident parallel wavevector to match it to the SPP wavevector at the same frequency. This relation describes Wood's observation of missing light frequencies in the diffracted spectra from a grating. In fact, Wood discovered the grating-assisted excitation of SPPs: Eq. 1.20 explains the phasematching condition when light in a narrow spectral region in the reflection pattern disappears because it has been coupled to SPPs. Dependent on the angle θ of the white illumination source with respect to the grating, light with a different frequency is phasematched and excites SPPs at the interface.

So far, the properties of planar SPPs, propagating in the x-direction, were described for the ideal case of an infinite plane wave illumination. In the scope of this thesis it is important to mention that in the experiments we have illuminated a grating-coupler with an incident Gaussian light source. As a result the excited SPP beam has a Gaussian transverse cross section (across y). Unlike SPPs with a planar wavefront and a clear direction of propagation, Gaussian SPPs effectively contain a (small) distribution of angles around the central direction of propagation which gives rise to transverse electric fields. The electric fields of a Gaussian SPP beam, propagating over a metal surface in the x-direction, result from the Fourier sum of plane waves [51], and are given by:

$$\begin{aligned}
\mathbf{E}_x^{in}(x,y,z) &= -C\frac{\omega_{spp}}{k_0\kappa_{spp}} e^{i\omega_{spp}z} \sum_{\kappa_y,\kappa_x} \kappa_x e^{-(\sigma^2/2)\kappa_y^2} e^{i(\kappa_x x+\kappa_y y)}, \\
\mathbf{E}_y^{in}(x,y,z) &= -C\frac{\omega_{spp}}{k_0\kappa_{spp}} e^{i\omega_{spp}z} \sum_{\kappa_y,\kappa_x} \kappa_y e^{-(\sigma^2/2)\kappa_y^2} e^{i(\kappa_x x+\kappa_y y)}, \\
\mathbf{E}_z^{in}(x,y,z) &= C\frac{\kappa_{spp}}{k_0} e^{i\omega_{spp}z} \sum_{\kappa_y,\kappa_x} e^{-(\sigma^2/2)\kappa_y^2} e^{i(\kappa_x x+\kappa_y y)},
\end{aligned} \tag{1.21}$$

where it is sufficient to limit the summation as $k_y \in [-k_0, k_0]$. Further, in Eq.1.21 $\kappa_{spp} = k_0\sqrt{(\epsilon+1)/\epsilon} = \sqrt{k_x^2 + k_y^2}$ and $w_{spp} = -k_0\sqrt{\epsilon+1}$ are the in-plane and out-of-plane components of the SPP wavevector, where $k_0 = 2\pi/\lambda$ is the free-space wavevector at a given frequency λ and ϵ is the dielectric constant of gold. The amplitude is given by C and the width of the Gaussian is determined by σ.

1.4.3 SPPs scattering from subwavelength holes

Arguably, one of the simplest plasmonic structures which can perturb an electromagnetic wave, is a single subwavelength hole in an optically thick gold layer. The perturbation of the electromagnetic fields near the hole results from the interaction of the incident fields with the free electrons in the metal boundary of the hole, which

can to first order be described as induced dipoles. Dependent on the polarization of the incident fields, a set of electric and magnetic dipoles are created, which determine the patterns of the scattered SPP waves.

The dipoles that are created at the hole positions are excited by the incident light, according to

$$\begin{aligned} \mathbf{p} &= \alpha_E \mathbf{E}^{\text{in}}, \\ \mathbf{m} &= \alpha_H \mathbf{H}^{\text{in}}, \end{aligned} \tag{1.22}$$

where $\alpha_{E(H)}$ is the electric (magnetic) polarizabilty of the hole, which can be measured or calculated [52].

In this dipole approximation, the equation of the scattered SPP wave can be written as [51]

$$\begin{aligned} \mathbf{E}^s(r) &= -\frac{2\pi i \epsilon e^{iw_{spp}z}}{\sqrt{1+\epsilon}(1-\epsilon)} \left[k_0^2 \kappa_{spp} H_1^{(1)}\left(\kappa_{spp} r'\right)\left(\sin\varphi m_x - \cos\varphi m_y\right) \right. \\ &\quad \left. -ik_0 \kappa_{spp}^2 H_0^{(1)}\left(\kappa_{spp} r'\right) p_z \right] \left(\hat{r} - \frac{\kappa_{spp}}{w_{spp}} \hat{z} \right). \end{aligned} \tag{1.23}$$

Here, $H_m^{(1)}$ are the Hankel functions, $r' = \sqrt{(x-x_0)^2 + (y-y_0)^2}$ correspond to the displacement from the hole position $\mathbf{r}_0 = (x_0, y_0)$, and $\hat{\mathbf{r}} = (\cos\varphi\hat{\mathbf{x}}, \sin\varphi\hat{\mathbf{y}})$, and φ is the angle from $\hat{\mathbf{x}}$ towards $\hat{\mathbf{y}}$. The in-plane electric dipoles are masked by the in-plane magnetic dipoles, hence their contribution can be neglected and their components are not included in Eq. 1.23.

In the context of this thesis we induce dipoles in a subwavelength hole with various incident electromagnetic fields. One method is to first excite a Gaussian SPP wave using a grating with a period Λ. The Gaussian SPP wave, $\mathbf{E}^{in}$, propagates in the direction of a subwavelength hole. The electric and magnetic fields of the incident SPP wave induce specific dipoles with orientations related to electric and magnetic fields of the SPP wave. The dipoles act as the source of the scattered field, $\mathbf{E}^s$. As sketched in Fig. 1.8a, the total field in the region surrounding the hole is the superposition of the incident and scattered field as $\mathbf{E}^T = \mathbf{E}^{in} + \mathbf{E}^s$. For the frequencies used in this thesis, the dominant incident field components of $\mathbf{E}^{in}$ are H_y and E_z. As a result two dipole orientations dominate the plasmonic response of the hole in this scenario: the in-plane magnetic dipole m_y and the out-of-plane electric dipole p_z. The term related to the magnetic dipole m_x in Eq. 1.23 will not contribute significantly to the scattered field in this excitation scheme. Therefore, the dipoles are simply $p_z = \alpha_{E_z}^{in}(r_0)$ and $m_y = \alpha_H H_y^{in}(r_0)$, where the polarizability $\alpha_{E(H)}$ that determines the response of the hole to the incident electric (magnetic) field has been calculated [52] and measured [51].

Second, the scattering of SPPs from a subwavelength hole was induced by a weakly focused light source, normal to the gold surface from the bottom of the substrate on the hole. This system can be easily extended to a system containing multiple holes.

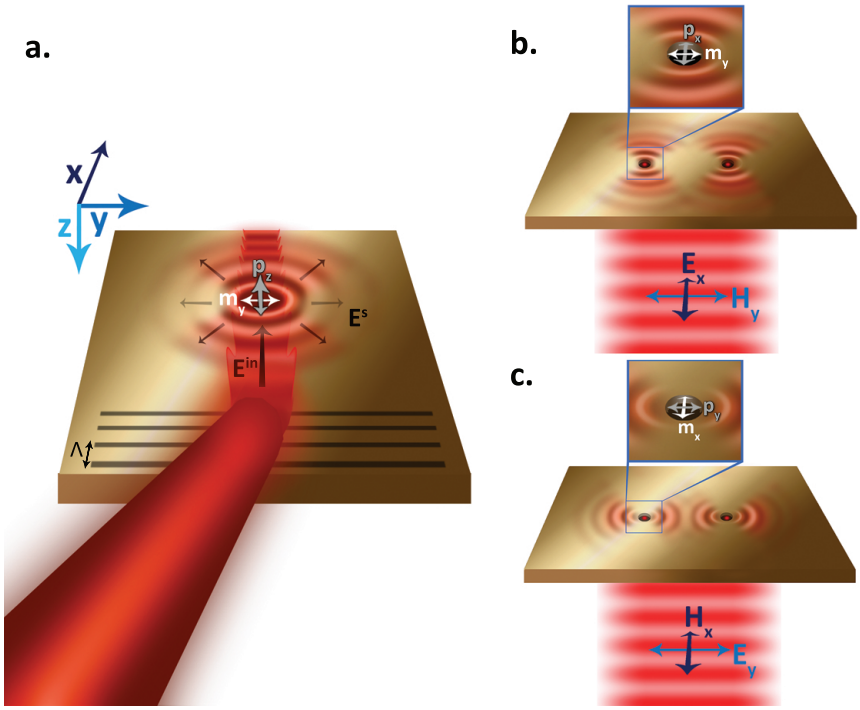

Figure 1.8: Scattering of light from single and multiple subwavelength holes in an optically thick film of gold. (a) An incident SPP beam E^{in} traveling over a gold surface towards a hole induces an in-plane magnetic dipole m_y and an out-of-plane electric dipole p_z, causing a scattering pattern E^s. (b) and (c) An incident beam, normal to the gold surface, illuminates 2 holes that are positioned on a line in the y-direction. Dependent on the polarization of the beam, the magnetic dipole m_y (b) or m_x (c) is excited, together with the out-of-plane electric dipole p_z.

The orientation of the electric and magnetic field of the beam will determine which dipoles are excited. In Fig. 1.8b an illumination beam which is polarized in E_x and H_y induces an in-plane electric dipole p_x and a magnetic dipole m_y. By rotating the polarization of the incident beam to E_y and H_x, the dipoles that are induced are the in-plane electric dipole p_y and magnetic dipole m_x (Fig. 1.8c). As mentioned previously, the in-plane electric dipoles are masked by the in-plane magnetic dipoles, hence their contributions are neglected in both polarization schemes of Fig. 1.8b and c. The total electric and magnetic fields arise from the addition of scattered SPP waves, potentially from multiple radiation sources. Only when light is polarized as shown in Fig. 1.8c, the SPPs generated at one hole can act as an additional source term for the neighboring hole(s), as further discussed in appendix D.

1.4.4 SPPs on nanowires

Another structure that is well studied in literature is the plasmonic nanowire, which is a desirable structure as it can act as a plasmonic waveguide, a potential information carrier for nanoscale information transport. Plasmonic nanowires can strongly concentrate electromagnetic fields, whereby the plasmonic wavelength can shrink over an order of magnitude with respect to the optical wavelength at the same frequency [53, 54]. For instance, a cylindrical metallic wire embedded in a homogeneous dielectric material supports guided modes for any radius of the wire. The modes that are supported by such wires have a radial polarization, and are known as Sommerfeld modes [55, 56]. Whereas Sommerfeld waves are weakly guided at THz frequencies, at optical frequencies the equivalent of the Sommerfeld waves are strongly confined to the metal wire when the radius is limited to only 10's of nm. These plasmonic modes are guided along the nanowire. Due to the low field overlap of the radial fields of the nanowire mode with the fields of a conventional incident light beam (which typically has no phase and/or polarization structure across the beam), it is challenging to excite such wires with free-space radiation.

The implementation of an efficient excitation scheme is possible, when using a subtly different plasmonic nanowire structure. For rectangular nanowires on a dielectric surface, a comparable nanowire mode exists, which is a guided Sommerfeld-like SPP wave. In Fig. 1.9a, a schematic illustration shows the nature of the SPP wave, supported by a rectangular gold nanowire with nanoscale dimensions on a glass substrate. A cross section along the length of the wire (depicted in the inset of Fig. 1.9a) shows that the electric fields and the charge distributions are similar to those of planar SPP modes, but with two interfaces of a metal and a dielectric medium (air and glass). In this crosscut, the SPPs have an E_x and E_z component. Away from the center axis of the nanowire, E_y also becomes non-zero. The result is a mode with a radial-like transverse field profile and a longitudinal field in the direction of the wire.

In Fig. 1.9b, cross-sections (yz-plane) of the normalized electric field are shown from simulations of gold nanowires with a rectangular cross-section and a height of 50 nm for 4 different widths and a free-space wavelength of $\lambda = 1550\ nm$. The electric fields are normalized by the total energy in the simulation box. Details about the simulations can be found in section A). For the largest width, fields are multiplied by 50 to be able to use the same scale bar for the intensity. On waveguides with nanoscale dimensions (first 3 images) we find that the highest fields are found at the sharp edges of the nanowire. Black arrows in the first image schematically indicate the radial-like field directions of the transverse electric field. From the cross sections it also becomes clear that a decrease of the nanowire dimensions results in an increased confinement of the electric fields.

The presence of a substrate has the advantage that the same SPP mode is supported for waveguide widths on the micrometer scale, where the electric field is mainly concentrated in the glass substrate. In the fourth image of Fig. 1.9b, the field distribution is shown for a 5 μm wide waveguide, where the black arrows schematically

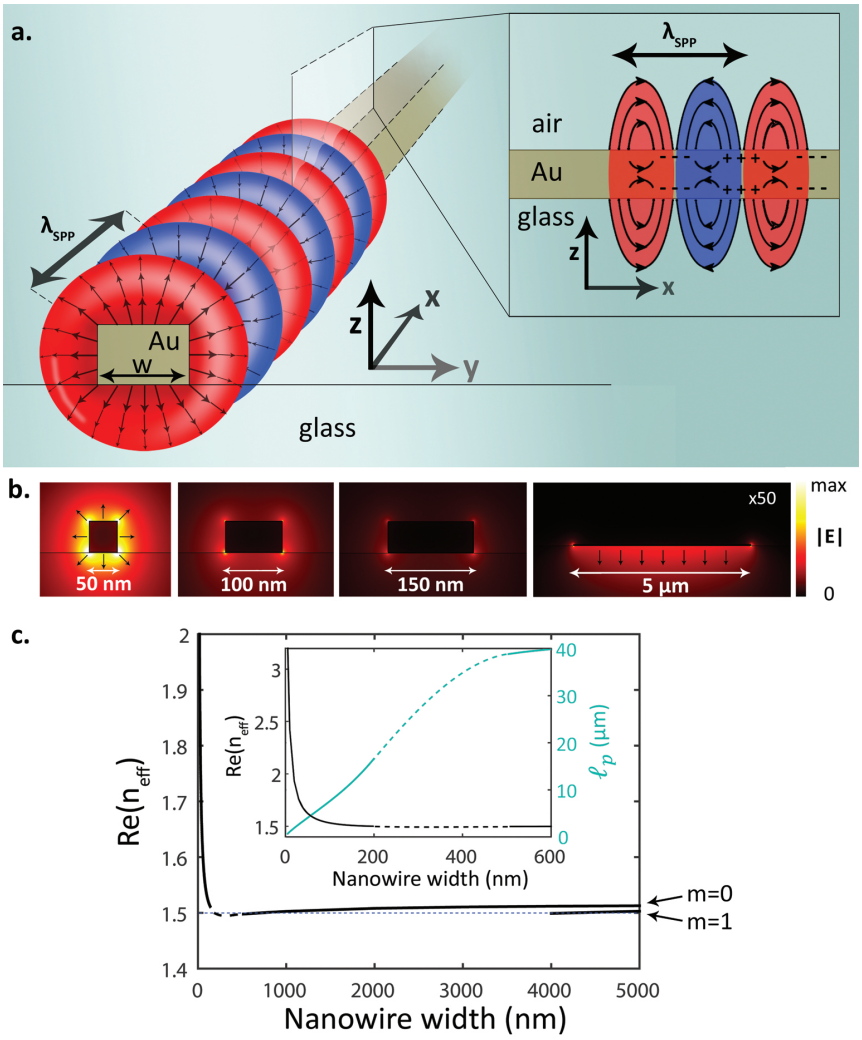

Figure 1.9: The guided mode of a rectangular Au waveguide on a glass substrate. (a) A schematic illustration of the electric field lines of the guided mode, the inset shows a cross section along the length and through the center of the waveguide. The plus and minus symbols illustrate the charge accumulation in the metal. (b) Cross-cuts of the normalized electric field intensity from simulations (Appendix A) for a waveguide of 50, 100, 150 nm and 5 μm wide, all 50 nm high using a free-space wavelength of 1550 nm, shown for cross sections in the yz-plane. Strong field confinement is observed for smaller nanowire dimensions. (c) The effective mode indices n_{eff} and propagation lengths ℓ_p as a function of waveguide width. n_{eff} of two modes are presented, where the m=1 mode has a cut-off at 4000 nm as the wire width reduces, and the fundamental plasmonic mode m=0 is supported by all widths. We therefore refer to the latter as the nanowire mode. The inset shows a close-up over the plasmonic (high n_{eff}) region of the nanowire mode. In both graphs, the dashed area shows the interpolated region where the mode is leaky.

indicate the electric field directions. The field profile of this mode has a much higher overlap integral with a typical incident far-field beam. Thus, excitation of the mode is readily achieved by, e.g., a grating, followed by the adiabatic conversion of the waveguide SPPs to that of the nanowire mode by gradually narrowing down the width of the waveguide along a taper [53, 57].

In Fig. 1.9c the real part of the effective mode index of two nanowire modes are plotted as a function of the nanowire width. The effective mode index n_{eff}, is related to the wavevector of the guided mode by $n_{eff} = k_{spp}/k_0$. We observe that, whereas the m=1 mode has a cut-off at 4000 nm as the wire width reduces, the fundamental plasmonic mode m=0 is supported by all widths, we henceforth call the latter the nanowire mode. The dashed blue line shows the refractive index of the glass surface, $n_{glass} = 1.50$. When narrowing the waveguide width, the effective mode index of the nanowire mode decreases subtly, reaching n_{eff} values lower than the refractive index of glass, hence leakage into the glass substrate can occur. When leakage happens under shallow incident angles, the reflectivity of the perfectly matched layers at the boundaries of the simulation box becomes nonzero. As a consequence, modes that show leakage under shallow angles cannot be reliably simulated and an interpolation is applied between the nanowire widths of 200-500 nm wide. As we further decrease the nanowire width from 200 to 0 nm, the nanowire mode gets more confined to the metal, as seen by an increasing effective mode index in Fig. 1.9c.

The confinement comes at a toll. As the fields are more concentrated in the metal, Ohmnic losses increase, hence decreasing the propagation length of the guided plasmons. In the inset of Fig 1.5c a close-up of the waveguides with dimensions up to 600 nm is shown, with n_{eff} (black line) and the propagation length ℓ_p (aquamarine line). Furthermore, the sensitivity of the field confinement to the nanowire dimensions offers adaptable parameters for a flexible interplay between loss and field confinement. In other worlds, it provides a certain degree of control over structured light fields.

1.5 Near-field microscopy

In section 1.4.2, we explained that the plasmonic wavevector k_{spp}, for guided modes propagating along the xy interface, is larger than the wavevector of light k_0 in vacuum. Consequently k_z is purely imaginary, giving rise to evanescent waves in the out-of-plane direction, z. Evanescent fields decay exponentially, typically within 10-100 nm away from the surface (section 1.4.2). In the ideal case of perfectly smooth metallic surfaces, no light is radiated into the far field, and an intermediate step is necessary to convert the near-field to far-field radiation. Moreover, the rich patterns in the fields near nanostructures exhibit features much smaller than the free space wavelength. To image such patterns at the nanoscale, a technique is needed that can measure optical fields with a sufficiently high resolution.

Intensity near-field microscopy

The first idea to develop an imaging instrument that could potentially beat the diffraction limit, was proposed by Edward H. Synge in 1928 [58]. In his original vision, he proposed to illuminate an opaque thin metal sheet containing a sub-wavelength hole, hereby creating an evanescent field on the other side of the sheet. By raster scanning this subwavelength light source at near-field distances from a sample, the interaction of the aperture in the sheet with the sample would be mapped, which would also provide information on the evanescent fields of the sample. This imaging system appeared to have a number of technical difficulties. For instance, due to the decaying near fields away from the sample's surface, the opaque sheet was required to be positioned with nanometer precision at a constant height in order to obtain reproducible near-field information. Moreover, the subwavelength hole only allowed for a low intensity throughput. Technology had to undergo serious developments for several decades before the actual first near-field image could be recorded.

The first optical near-field microscope was patented by Dieter Pohl [59], and the concept was based on the scanning of an extremely narrow aperture probe, rather than an entire sheet. The first images taken with the aperture indicated a resolution of $\lambda/20$ [60]. Interestingly, Synge already proposed this improved version of aperture probe near-field scanning microscopy, but realized that the technical advances at that time did not yet allow the actual implementation. Today, many different near-field scanning techniques exist to map the evanescent fields, of which the traditional aperture (probe) near-field scanning optical microscopy (a-NSOM) is just one profitable example to study features at the nanoscale. Credits for the improved implementation of the a-NSOM, which many researchers benefit from, also go to Betzig [61].

In this thesis, near-field measurements are presented using an aperture probe in collection mode. The sharp tip is created by heating and pulling an optical fiber, which is then covered with an optically thick layer of aluminum. The end of the tip is subsequently removed using a focused ion beam to produce an aperture [62]. The aperture size mainly governs the resolution of the near-field images. The aperture picks up evanescently decaying waves, by frustrating a small fraction of the waves and converting it to far-field radiation. Due to the rapidly decaying evanescent fields and the low collection efficiency of the tip, the probe has to be brought into close proximity to the sample (within 10's of nm in height) before it is raster-scanned across the sample. The near-field probe is kept at a constant height above the sample with a shear-force based mechanism [63]. The ideal aperture size is a trade-off between the collection efficiency, which benefits from larger apertures, and the resolution, for which smaller apertures are best. In our experiments the apertures typically have a diameter of $\lambda/8$, where λ is the free-space wavelength used in the experiment. This allows us to measure fields with a resolution beyond the diffraction limit with a reasonable signal-to-noise.

The mechanism of how even a standard circular aperture probe converts the evanescent fields to far-field radiation is far from trivial. Moreover, interaction be-

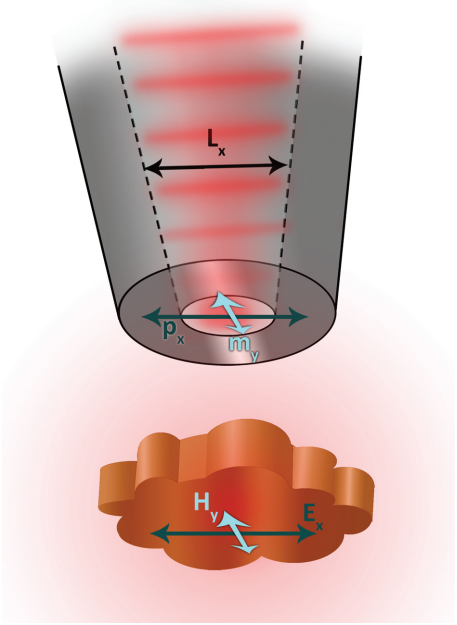

Figure 1.10: Schematic depiction of the conversion of a small fraction of near-field radiation to far-field radiation using an aperture based near-field scanning probe. The evanescent fields in the vicinity of the plasmonic structure induce dipoles at the apex of the probe. The induced in-plane dipole moments can couple to the propagating mode of the fiber, which can then be detected in the far field. In this sketch, the electric dipole in the x direction is shown as an example. The field which is detected L_x results from both E_x and H_y fields near the nanostructure. The same principle holds for y polarized light L_y (not illustrated), which arises from both E_y and H_x fields in the evanescent fields.

tween the near-field probe and the sample can influence the obtained optical signal. When such interactions are negligible, the electromagnetic near fields are assumed to interact with the aperture probe by inducing a dipolar charge distribution in the probe. In this approach, induced out-of-plane dipoles do not contribute to the detected signal, as their radiation pattern does not couple to the propagating mode of the fiber, attached to the probe. On the other hand, the in-plane dipoles exhibit a radiation pattern which can couple to the propagating mode in the fiber. Recently, it was found that both the electric and magnetic near fields can induce dipoles, which contribute to the measured signal [64]. In Fig. 1.10, the in-plane fields E_x and H_y of a nano object are illustrated to induce the dipoles p_x and m_y respectively, which both contribute to the detected signal associated with the x orientation, L_x. Likewise, the fields E_y and H_x contribute to the detected signal associated with the y orientation, by inducing the dipoles p_y and m_x in the probe [65].

Phase-resolved microscopy near-field microscopy

Recent developments in near-field microscopy enabled us to acquire more information than just the near-field intensities [66–69]. By implementing an interferometric approach, in which a signal collected from the sample is combined with a reference signal, both the amplitude and the relative phase of the light in the structure can be mapped (Fig. 1.11). Using a beam splitter, the incident light is separated, where the signal branch is formed by the light that is coupled to the sample and the resulting evanescent field is picked up with an aperture probe. The picked-up light is subsequently combined with the light in the reference branch and the interference signal is measured by a photodiode.

We use a heterodyne detection scheme in which the frequency of the reference branch is shifted by 40 kHz using two acoustic-optical modulators (AOMs). Combining the light in the reference and signal branch produces a beat signal at 40 kHz. This beat can be exploited to amplify the voltage signal on the photodetector using a lock-in amplifier, by allowing only signal in a narrow frequency band around the frequency difference, thus suppressing noise at frequencies outside the filter bandwidth. The complex signal L, constructed from the output voltages of the lock-in detector is related to the amplitude of the electric field of the reference A^R and the signal A^S following:

$$L \propto A^R A^S e^{i\Delta\phi}. \tag{1.24}$$

Here, $\Delta\phi = \phi^R - \phi^S$ is the phase difference between the reference and signal branch. From the equation it becomes clear that the amplitude of L is proportional to $A^R A^S$, rather than $(A^S)^2$, which is the case when the signal from the signal branch alone is measured on a photodiode. Hence, the heterodyne interferometric approach amplifies the signal by a factor of A^R/A^S.

Polarization-resolved near-field microscopy

In our plasmonic structures, the bound SPPs propagate in the xy-plane. In order to study polarization-dependent features, such as optical singularities, we need to resolve both orthogonal in-plane polarizations. In Fig. 1.11 three polarization-sensitive elements are added to the optical path for polarization-resolved mapping. Electromagnetic waves that enter an optical fiber may experience birefringence, due to stress applied to the fiber (e.g. bending or twisting). Linearly polarized radiation, picked up by the aperture probe, can therefore become elliptically polarized. To correct for this phenomenon, a $\lambda/4$ wave plate is adjusted such, that the elliptical light is projected back into linearly polarized light. The second half-wave plate, $\lambda/2_{(B)}$, then rotates the axis of the light in such a way that the fields associated with the x-oriented signal L_x, E_x and H_y are collected by detector D2. Conversely, the fields associated with the y-oriented signal L_y, E_y and H_x are collected by detector D1. The x- and y-oriented signals are separated by a polarizing beam splitter. In order to equally distribute the heterodyne gain over detector D1 and D2, another half-wave

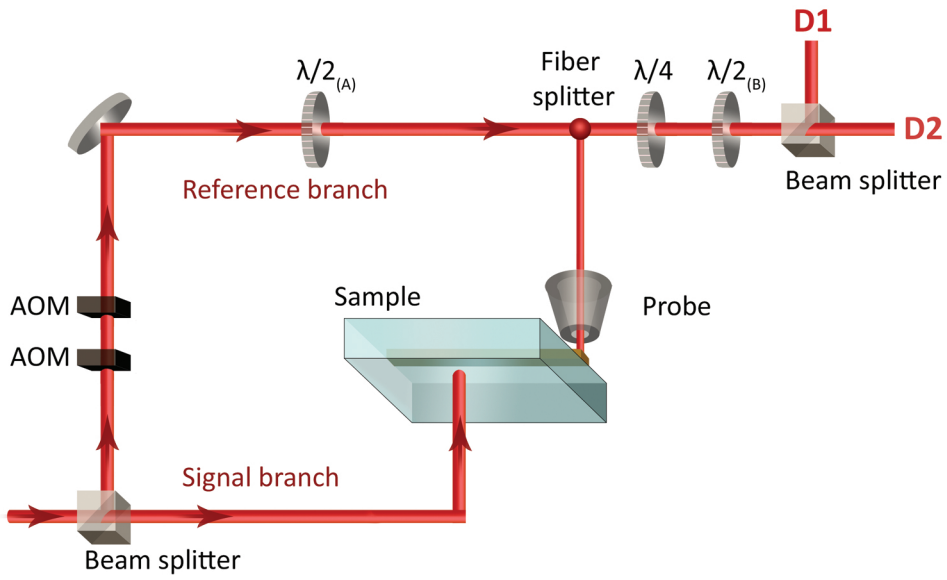

Figure 1.11: Schematic of phase- and polarization-sensitive near-field microscopy. An incident light source is split in a beam splitter, separating the beam into a signal and a reference branch. The signal beam couples to the sample (in this case from the bottom through a glass substrate). The evanescent waves are picked up with the aperture probe and subsequently converted into propagating modes in a single-mode detection fiber. The reference branch passes through two AOMs, where the frequency of light shifts by 40 kHz. The signal and reference branch are then combined and converted to free-space after which polarization optics separates the signals into L_x and L_y, detected by detector $D2$ and $D1$ respectively.

plate $\lambda/2_{(A)}$ is added to the setup, which balances the intensity of the reference branch over both detectors.

1.6 Outline of this thesis

This thesis describes experimental and theoretical studies on plasmonic structures where guided SPPs play a role. We investigate the potential for manipulation of light at the nanoscale, by controlling light's smallest optical features (singularities), and through wavelength conversion (harmonics generation).

In chapter 2 we investigate the potential of gold nanowires to act as a waveguide for nonlinear optical effects. We present the first observations of second- and third-harmonics on single plasmonic nanowires, generated at visible wavelengths. We confirm that the guided near-infrared surface plasmon polaritons act as the source of the harmonics. Further, we discuss the possible underlying mechanisms of second-harmonic generation, using simulations and spatially resolved measurements.

In chapter 3 we investigate the relation between the electric and magnetic fields from numerical simulations and the measured signal from a near-field microscope above a plasmonic nanowire. We use the optical reciprocity theorem to calculate expected measured signals from the simulated properties of the probe and the nanowire mode. We find good agreement between experiment and prediction. Additionally, we find that the sensitivity of the near-field probe to the magnetic and electric field are approximately equal.

In chapter 4 we present the results of our search for the simplest plasmonic system that contains and can be used to control optical singularities. We identify optical singularities in the electric field distributions near single subwavelength holes in a gold film, through both near-field measurements and theoretical modeling. We achieve control (in calculations) over the singularities, by simply tuning the hole diameter and the width of the incident illumination beam.

In chapter 5 we expand our plasmonic system from chapter 4 to a system containing multiple holes, positioned in series, and theoretically investigate the control over polarization singularities. We find that the light fields around 2 subwavelength holes are enough to create singularities when illuminated under the right conditions and that their number can be controlled through the distance between the holes. We find a quantization in the number of singularities that are created as the distance is increased. Subsequently, their creation and topological charge are described in detail.

Chapter 2

Harmonics generation by surface plasmon polaritons on single nanowires

In this chapter we present experimental observations of visible wavelength second- and third-harmonic generation on single plasmonic nanowires of variable widths. We identify that near-infrared surface plasmon polaritons, which are guided along the nanowire, act as the source of the harmonics generation. We discuss the underlying mechanism of this nonlinear process, using a combination of spatially resolved measurements and numerical simulations to show that the visible harmonics are generated via a combination of both local and propagating plasmonic modes. Our results provide the first demonstration of nanoscale nonlinear optics with guided, propagating plasmonic modes on a lithographically defined chip, opening up new routes towards integrated optical circuits for information processing.

This chapter is based on A. de Hoogh, A. Opheij, M. Wulf, N. Rotenberg and L. Kuipers, *Harmonics generation by surface plasmon polaritons on single nanowires*, ACS Phot.**3**, 1446 (2016).

2.1 Introduction

Nonlinear optics is of tremendous importance to modern, light-based technology [40]. Nonlinear optical phenomena, which lead to all-optical control of light fields or generation of new colors of light, are at the heart of applications, ranging from laser based techniques [70] and microscopy [71], to optical and quantum information processing [72]. The recent use of nanophotonics to bring nonlinear optics to the nanoscale [73, 74] has allowed researchers to migrate these technologies to compact, integrated optical chips. Moreover, as these devices have shrunk, the concentration of the light fields has necessarily grown, enhancing the electric fields and boosting inherently weak nonlinear effects [75, 76].

Plasmonic platforms, known for confining fields to highly subwavelength dimensions, are promising candidates for bringing nonlinear optics to the nanoscale [24, 77]. Research in this area has, to date, mainly focused on the use of localized surface plasmon resonances, which are found on metallic nanostructures, to enhance nonlinear effects [78–84]. For example, using plasmonic nanoantennas researchers have demonstrated efficient third-harmonic generation [80]. Likewise, coupled gold nanoparticles have been used to greatly increase the efficiencies of four-wave mixing [79]. Moreover, harmonic generation has been observed during transmission through a metallic hole array, where the aspect ratio of the hole controls the generation efficiency [84]. In contrast, little work has been done on nonlinear optics with surface plasmon polaritons (SPPs), plasmonic modes that propagate, and what has been demonstrated has been mainly limited to interface SPPs [85, 86], which are confined in only one dimension, or at the tip of a taper [87, 88]. A study of nonlinear effects using plasmonic modes of waveguides such as nanowires (NWs), with a well-defined, uniform guided mode that is confined to a small cross-sectional area, is, to date, lacking. However, nonlinear processes on such structures could be very beneficial as they can support extremely high bandwidth pulses [77, 89], allowing for high-intensity operation at low powers.

Here, we present the first experimental observations of a nonlinear optical effect, namely, harmonic generation by guided SPPs on single Au NWs. We use a combination of spectral and spatial far-field microscopy to resolve both second- and third-harmonic generation (SHG and THG), using fundamental femtosecond pulses at 1550 nm, on NWs with widths ranging from 90 to 550 nm. We identify the guided fundamental SPPs as the source of the harmonic generation, and discuss the processes that drive this nonlinear effect.

2.2 Harmonics generation on plasmonic nanowires

To study whether guided SPPs can be used to generate harmonics we use lithographically defined Au NWs on a BK7 substrate, as described in Appendix A. We select this system, which is shown in Fig. 2.1a, for several reasons. First, these NWs are known to support SPPs and, importantly, the fundamental plasmonic mode has no

cutoff; in fact, as the wire dimensions shrink, the mode is increasingly confined to the metal, becoming more plasmonic in nature (see Fig. 2.1b) [54]. Second, we can efficiently couple free-space radiation to the NW SPPs, first using a grating to excite glass-Au interface SPPs, which are subsequently adiabatically transformed to NW SPPs with a taper [53, 90]. Finally, these Au NWs can be fabricated in a highly controlled and reproducible manner using electron-beam lithography, enabling the development of nanoscale optical circuitry. Despite the centrosymmetric character of Au, it is reasonable to also expect second-order nonlinearities (the potential for SHG) when the structural symmetry is broken [91–93]. Such symmetry breaking occurs at the surfaces of the NWs where, conveniently, the plasmonic intensities are highest. At the same time, the symmetry of the NW geometry, as a whole, is also broken by the presence of the substrate. For our experiments, to study the effect of wire geometry on the harmonic generation, we fabricate 50 nm thick wires with widths ranging from 90 to 550 nm.

To achieve the relatively high intensities required for nonlinear optical experiments, we use an 80 MHz repetition rate, 120 fs pulsed Ti:sapphire laser (with an average illumination power of $\approx 15mW/s$, this results in a pulse energy on the order of $\approx 1.9e^{-7}$ J). This laser light is passed through an optical parametric oscillator, resulting in pulses with a central frequency of 1550 nm, which we use to illuminate the grating (Fig. 2.1a). As explained above, the resultant interface SPPs are then adiabatically converted to guided NW SPPs. A small fraction of the guided light on the NWs (either the fundamental, or any harmonics) will be scattered off the wire by residual surface roughness or fabrication imperfections. We collect the light that is scattered perpendicularly to the sample surface with a 0.65 NA microscope objective and send it either to a spectrometer or to a CCD camera. In the latter case, we use a combination of filters to first spectrally select the frequency ranges of the harmonics ($480 - 520$ nm and $750 - 800$ nm for the third- and second-harmonics, respectively). The resulting CCD images have a spatial resolution of 0.54 μm per pixel. We note that the fundamental cannot be mapped in this way, as, near the beginning of the NW, the residual signal from the incident laser beam is much brighter than the scattered fundamental SPPs (see Appendix B). When using the spectrometer, a slit is used to ensure that we only collect light that originates from the NW. In addition to the experiments, we also perform finite-element simulations (using the mode solver in COMSOL Multiphysics) to study the modes of the Au NWs. In these calculations, we use a refractive index of the BK7 glass substrate of 1.5 and take the complex refractive index of Au from literature [50]. From these calculations we can extract both the properties of the plasmonic modes (e.g. their effective mode index or propagation length), as well as their mode profiles. Examples of mode profiles, for the beginning and end of the taper, are presented in Fig. 2.1b. We observe that the gradual decrease of the NW width from 5 μm down to 150 nm results in electromagnetic field enhancements at the metal surface by a factor of approximately 15.

2.3 Far-field measurements

Having set out to detect harmonic generation from plasmonic NWs, we were pleasantly surprised to observe strong green light (as expected for the third harmonic of 1550 nm light) scattering from our sample while aligning our setup. By imaging the NW through a slit, we confirm that the source of the scattered, green light is indeed the NW and not, for example, the hole array.

When imaging our sample with different filters, we observe that the spatial maps of the scattered light (Fig. 2.1c) for the green and red light, which are expected to correspond to third- and second-harmonic generation, respectively, have nearly identical spatial distributions in the intensity of the SHG and THG along the nanowire. One noticeable difference, however, is that the TH signal, whose generation is expected to scale with the third power of the fundamental intensity, appears to fade more quickly along the NW than the SH signal, which scales as the second power. In the maps for a 150 nm wide NW, which we present in Fig. 2.1c, we observe scattering for over 10 μm along the NW. We observe SH and TH signal scattered along the wire, with distinguishable bright and dim areas. For a given nanowire, the locations of the bright and dim points of the SH and TH signal coincide, indicating that scattering of SH as well as TH seems to occur at the same points along the nanowire. However, the location of the bright points, and therefore the pattern of SH and TH, differs from nanowire to nanowire. Even nominally identical wires exhibited seemingly random and distinct distributions of bright spots. This observation indicates that the scattering is due to random fabrication roughness. AFM measurements on four NWs with different widths reveal an average root-mean-square value of 5-7 nm. In scanning electron micrographs of these different NWs (an example of which is shown in the top panel of Fig. 2.1c), we could not identify physical structures that would correlate with the observed optical patterns. Please note that as neither AFM nor SEM was able to identify clear scattering centers, they are either small, hard to identify in a trivial manner from geometry or even located at the glass-Au interface close enough to the sides of the nanowire that a signal in the collection direction could be generated. Furthermore, we envision that fabrication imperfections might even lie inside the NWs, due to the deposition process.

Next, we verified the plasmonic source of our visible signals by rotating the polarization of the incident light. We expect that visible light will only be detected when the sample is illuminated by p-polarized light (the only polarization that launches SPPs(ω) on the NW), and not with s-polarization, even when, in the latter case, significantly higher input powers are used. In Fig. 2.1d, we show an example of the distributions of red light along the NW for the two polarizations. Indeed, as expected, this signal is only visible when SPPs are launched, confirming that the source of the visible light is plasmonic. Similar results (not shown) were obtained with the green light. Finally, we observe that the distinct scattering pattern of a NW can be irreversibly altered by exceeding a certain illumination power, which permanently damages the structure. It is found that this damage threshold can vary by over an order of magnitude for different structures. Illumination powers of around 60 mW

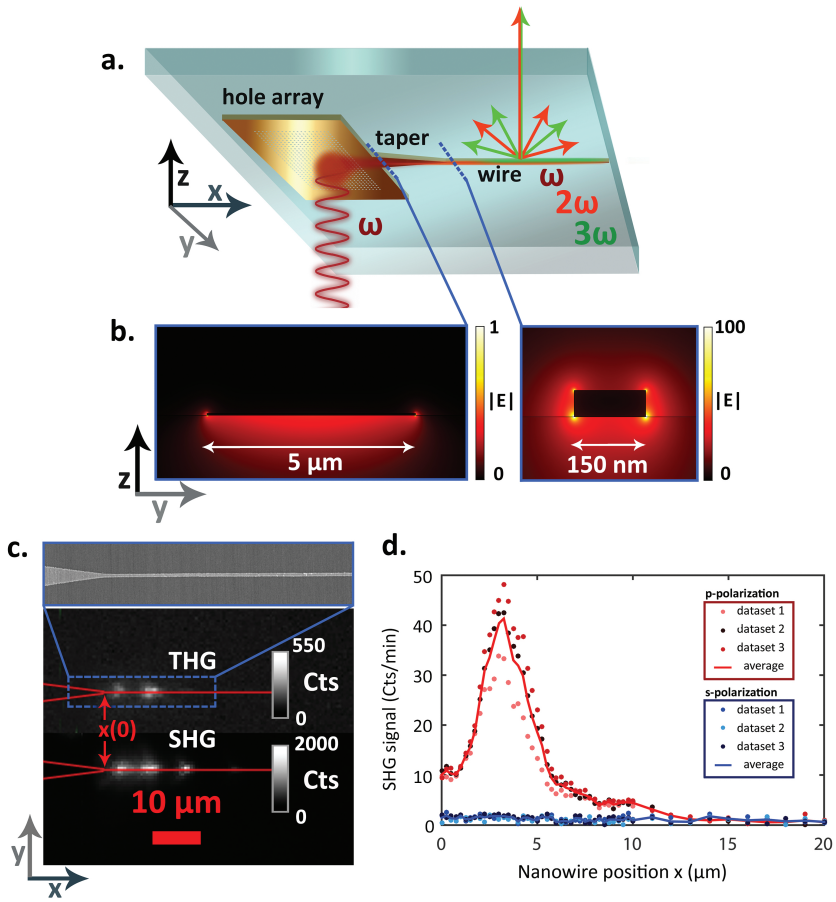

Figure 2.1: Harmonics generation on single Au nanowires on a glass substrate. (a) Schematic representation of the experiments. A hole array is illuminated from the Au-glass interface with p-polarized fs pulsed laser light, with a central wavelength $\lambda = 1550\ nm$. The interface SPPs, which propagate in the x direction, are adiabatically converted to NW SPPs by gradually reducing the width of the waveguide [25]. Visible light that scatters from the wire is collected on the Au-air side. (b) Normalized electric-field distributions obtained from FEM simulations of the fundamental SPP mode for a cross section of the nanowire with a thickness $t = 50\ nm$ and a width $w = 5\ \mu m$ (left) and $w = 150\ nm$ (right). (c) Examples of scattered visible light maps at $480-520\ nm$ (top) and $750-800\ nm$ (bottom), measured with a CCD camera. The scale bars represent spectrometer counts (Cts) per 5 minutes. The red overlay shows the end of the taper and the wire to guide the eye. Top blue box: a typical electron micrograph of an Au NW ($w = 150\ nm$). (d) SHG signal in spectrometer counts per minute, as a function of position for both p-and s-polarized excitations, shown with red and blue symbols, respectively. Although the excitation power of the s-polarized light is 3.75 times larger than that of the p-polarized light, SHG is only observed for the latter.

showed severe melting of 4 out of 5 structures on their hole arrays, in addition the taper separated irreversibly from the nanowire. Furthermore, we have observed a less severe degree of damage when using lower illumination powers. Here, the images of SHG and THG on the nanowire changed gradually over time. Sometimes, a steady state was reached after a certain exposure time and the intensity pattern along the nanowire remained unaltered afterwards. These nanowires looked visibly unaltered in the SEM, and we expect the changes to be in small roughness features that got 'annealed'. The general trend that we discovered was that illumination powers of up to 20 mW could be considered 'safe' for most nanowires. The results presented throughout this work are limited to those measurements where no signs of damage were observed on the structures during and after measurements.

We verify the nature of the strong visible signal that we observe to ensure that it is indeed caused by harmonic generation. A typical far-field spectrum of the scattered light, shown in Fig. 2.2a, contains two clear peaks at 775 and 517 nm, nicely corresponding to the expected wavelength of SHG and THG respectively, for a fundamental wavelength of 1550 nm. Moreover, the small spectral width of the peaks is indicative of nonlinear harmonic generation and not luminescence that, for gold, also results in the emission of visible light but with a much broader spectral signature [94].

To ensure that the scattered light results from SHG and THG we measure its intensity as a function of the incident laser power. The results of this power study are plotted in the inset to Fig. 2.2a on a double-log graph. The nonlinear SHG (THG) is supposed to scale with the second (third) power of the incident light [40]. Indeed, from a fit to the data in Fig. 2.2a, we find that the slopes of yield of the SHG (red circles) and THG (green circles) are 1.9 ± 0.1 and 3.0 ± 0.1, respectively. Furthermore, we have also varied the wavelength of the incident beam and confirmed that the second- and third-harmonic wavelengths are always found at 1/2 and 1/3 of the fundamental (Fig. 2.2b). Altogether, these results confirm that second- and third harmonics are generated by SPPs on the Au NW.

Since we know the source of the harmonics to be the fundamental SPPs, what remains to be determined is the physical process by which these harmonics, which we detect, are generated. One plausible cause for the observation of harmonics on the nanowire could be that harmonics are merely generated at the apex, where the plasmonic intensity is the strongest. In principle, the newly generated SPPs at 2ω and 3ω themselves could then propagate along the nanowire, without any further need for a source. In this case, the harmonic SPP signals in our experiment at $2\omega(3\omega)$ would then exhibit a decay length $\ell_{d,2\omega(3\omega)}$ approximately equal to the propagation length $\ell_{p,2\omega(3\omega)}$ of the plasmonic modes at $2\omega(3\omega)$ as derived from simulations. From the simulations we know that the propagation lengths for SPPs propagating along a nanowire of 150 nm wide, are $\ell_{p,\omega} = 11.6\ \mu m$, $\ell_{p,2\omega} = 2.6\ \mu m$ and $\ell_{p,3\omega} = 37.3\ nm$ for the fundamental, second and third harmonic respectively. The fact that $\ell_{p,3\omega} \ll \ell_{p,2\omega}$ is mainly due to the spectral distance of each respective harmonic to the d-band transition of gold. We find detectable signal for both SHG and THG for all nanowires, many micrometers along the propagation direction, of which an example is presented

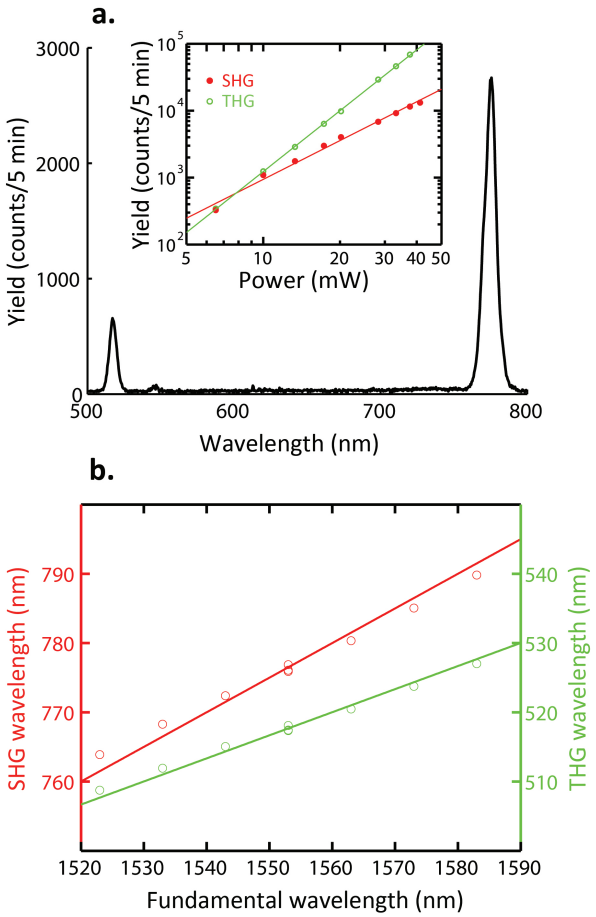

Figure 2.2: Harmonics generation on a 150 nm wide Au NW. (a) A typical far-field spectrum exhibits peaks at 775 nm (SHG) and 517 nm (THG), for a fundamental wavelength of 1550 nm and 20 mW incident power at 3 μm from the beginning of the wire. The inset shows the yield (in counts per 5 minutes) for the SHG (red circles) and THG (green circles) signal as a function of incident laser power. Spectra were collected 1 μm from the beginning of the wire. The solid lines are power fits, resulting in slopes of 1.9 ± 0.1 and 3.0 ± 0.1 for the SHG and the THG data, respectively. (b) A wavelength study shows that the SHG (THG) wavelength shifts as a function of the fundamental incident wavelength in red (green) circles. The red (green) solid lines are linear trends with a slope of 1/2(1/3) of the fundamental wavelength over the range 1520 to 1590 nm.

in Fig. 2.1c for a 150 nm wide nanowire. In order to collect harmonic signal of the magnitude observed in the experiment, even 10 μm away from the apex, the decay length $\ell_{d,2\omega(3\omega)}$ has to greatly exceed $\ell_{p,2\omega(3\omega)}$. Hence, the second and third harmonics must have a constant source of generation along the nanowire, and the harmonics cannot be merely generated at the apex.

There are three distinct processes left that can lead to free-space harmonics on our sample, which we sketch in Fig. 2.3a. Firstly, harmonics can be efficiently generated at local field hotspots, caused by imperfections in our sample (process I), resulting in 2ω photons radiating away from the sample. In this case, we would expect the SH point spread function to be sharply peaked at the position of the imperfections since this process relies on a local plasmon resonance (LPR).

The other two processes by which harmonics can be generated on the NW, which are denoted processes II and III in Fig. 2.3a, rely on propagating SPP modes and not LPRs. In process II, SHG converts the fundamental SPP to a 2ω SPP that also propagates on the NW. Due to surface roughness, this 2ω SPP is scattered into free-space photons that we can detect. Process III, meanwhile, is the direct conversion of fundamental SPPs into 2ω photons. Because both of these processes rely on propagating waves as sources, we expect that the detected SH will vary smoothly as a function of position on the NW, with the details of this spatial dependence being determined by the NW geometry. More specifically, we can expect the intensity of the generated second harmonics by process II and III to decay exponentially. The intensity of the fundamental SPPs decays exponentially along the wire, x, via $I_\omega(x) = I_0 e^{-x/\ell_{p,\omega}}$, with $\ell_{p,\omega}$ the propagation length of SPPs(ω). Because the intensity of the second and third harmonic depends on the intensity of the fundamental quadratically, $I_{2\omega} \propto I_\omega^2$, and cubically, $I_{3\omega} \propto I_\omega^3$, we expect for processes II and III that the position dependence of the second harmonic is described by $I_{2\omega}(x) = I_0 e^{-x/\frac{\ell_{p,\omega}}{2}}$ and $I_{3\omega}(x) = I_0 e^{-x/\frac{\ell_{p,\omega}}{3}}$. In other words, when guided fundamental plasmons act as the source of second and third harmonics, their decay lengths should be $1/2$ and $1/3$ the propagation length of the fundamental, following $\ell_{d,2\omega} = \frac{\ell_{p,\omega}}{2}$ and $\ell_{d,3\omega} = \frac{\ell_{p,\omega}}{3}$.

To confirm that the fundamental SPPs act as the source of the harmonics, we derive their decay length $\ell_{d,2\omega}$ from the decay of the second-harmonic intensity along the nanowire, which should follow $I_{2\omega}(x) \propto e^{-x/\ell_{d,2\omega}}$. Hence, we look for the spatial signature of the harmonic generation processes at low powers where the SH signal is greater than the TH signal (see inset to Fig. 2.2a), to avoid damaging the NWs. At these low powers, the TH signal from the NW is comparable to that from the glass interface [31], and consequently we henceforth restrict ourselves to studies of the SH. An example of the spatial intensity maps of the SH, here for four different 90 ± 10 nm wide NWs, is shown in Fig. 2.3b. Such maps are obtained by integrating the yield maps (e.g. Fig. 2.1c) along the NW width (over 6 pixels along $y \approx 3$ μm), for different x positions along the NW. In this figure, $x = 0$ μm (marked by the dashed line) is the beginning of the NW. Before the NW (x is smaller than 0 μm), as the taper width decreases (sketch above Fig. 2.3b), we observe that the SHG yield gradually increases to a maximum value near $x = 0$ μm. This increase shows that the plasmonic mode on

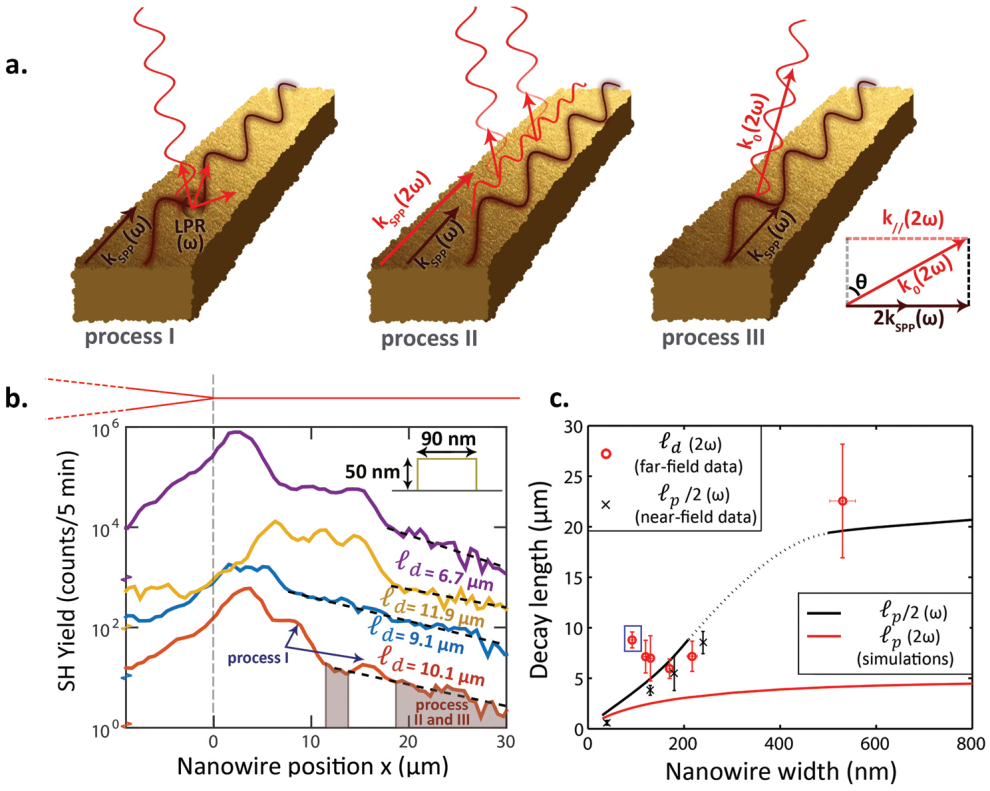

Figure 2.3: The spatial evolution of the second-harmonic generation on plasmonic nanowires. (a) Schematic depiction of three processes that can occur on the NWs, which result in 2ω photons radiating towards our detector. Process I is the local plasmon resonance (LPR) enhanced harmonic generation from defects in the sample. Process II is plasmonic second-harmonic generation, while in process III fundamental SPPs are directly converted into 2ω photons. Process III results in a coherent beam under a specific angle θ if phase-matching conditions (inset) are fulfilled. (b) Measured SH yield from four nominally identical 90 nm wide NWs (offset vertically for clarity). The NW begins at $x = 0$ μm, as shown in the sketch above the figure and indicated by the dashed gray line. In each curve, we observe peaks, which are indicative of HG via process I, and exponential decay, which is indicative of processes II and III. Fits, and the resultant decay length, ℓ_d, constants for the latter regions are shown for each curve. (c) Extracted ℓ_d of 2ω as a function of NW width (empty red circles). Also shown are the calculated $\ell_{p,2\omega}$ and $\ell_{p,\omega}/2$ for 2ω and ω SPPs, in red and black curves, respectively. We have included near-field measurements of the decay of the fundamental SPPs (black crosses). Note, however, that we plot $\ell_{p,\omega}/2$ rather than $\ell_{p,\omega}$, because of the anticipated $\ell_{d,2\omega} = \frac{\ell_{p,\omega}}{2}$.

the narrower width sections is better confined, resulting in larger field enhancements (e.g. see Fig. 2.1b) and hence more SHG.

On the NWs we observe two distinct types of features in the SH. At random locations along each NW we observe strong peaks in the harmonic signal (which are more easily observed on linear plots; see Appendix C). As an example, we have marked these peaks with arrows, on the first (red) curve. These, then, are locations where process I occurs, and harmonics are generated at hot-spots of defects.

In the SH signal, we also observe large regions where there are no large defects and the harmonic decays smoothly, as expected from processes II and III. For the SH signal of the first NW that we show in Fig. 2.3b (red curve), these are marked by shaded regions. In these semi-logarithmic plots, the spatial evolution of the SH signal appears linear, indicating that it decays exponentially. We can therefore extract a decay length, $\ell_{d,2\omega}$, for each NW trace, as is shown in Fig. 2.3b. By averaging over the traces of nominally identical wires, we determine a decay length for each specific wire geometry (see Appendix C). In the case of the 90 nm wide wires shown in Fig. 2.3b, this decay length is 8.8 ± 0.8 μm.

In this manner, we measure $\ell_{d,2\omega}$ for different width NWs, presenting the results in Fig. 2.3c (open red circles). In this figure we also give the calculated $\ell_{p,2\omega}$ for SPPs at 2ω, as well as $\ell_{p,\omega}/2$ for SPPs at ω (with red and black curves, respectively). Clearly, the measured $\ell_{d,2\omega}$ is always much larger than the propagation length of the 2ω SPPs, yet agrees well with $\ell_{p,\omega}/2$ of the ω SPPs. We do, however, observe a deviation between our measurements and calculations for the narrowest NWs. We do not know the origin of this deviation. We conjecture that this difference could arise from the fact that the quality of the Au could be different for these sub-100 nm wide wires. To validate the behavior of the fundamental SPPs, we included near-field measurements on these same sample of wires (taken from ref. [77]), which confirms that the calculated $\ell_{p,\omega}/2$ of the fundamental SPPs are correct in the plasmonic region (Fig. 2.3c, black crosses). Indeed, as can be seen from Fig. 2.3c, our measurements of $\ell_{d,2\omega}$ are in agreement with both the near-field measurements, and simulations, of $\ell_{p,\omega}/2$. This measured spatial dependence of the second-harmonic signal is therefore consistent with a process where the intensity of the generated second harmonic is dependent on the $I(\omega)^2$ at that same position. From the data, we conclude that the fundamental SPPs are the source of the observed harmonics and, indeed, harmonics are generated both from LPRs and SPPs.

To determine which of the two processes, II or III (see Fig. 2.3a), are responsible for the exponentially decaying signal, we consider the wavevectors of the light fields in our system. We show these wavevectors, which are associated with either SPPs or photons (as denoted by the subscripts SPP or 0, as a function of NW width in Fig. 2.4a. Here, we show the wavevectors for NW widths of up to 200 nm, since for wider NWs these wavevectors are almost constant as a function of NW width. In this plot we look for phase-matching between the fundamental SPPs, where we consider $2k_{SPP,\omega}$ (dashed black curve) since SHG requires two fundamental SPPs, and either the second harmonic SPPs or photons, denoted by $k_{SPP,2\omega}$ and $k_{0,2\omega}$ (red and blue curves, respectively). In other words, phase matching for processes II and

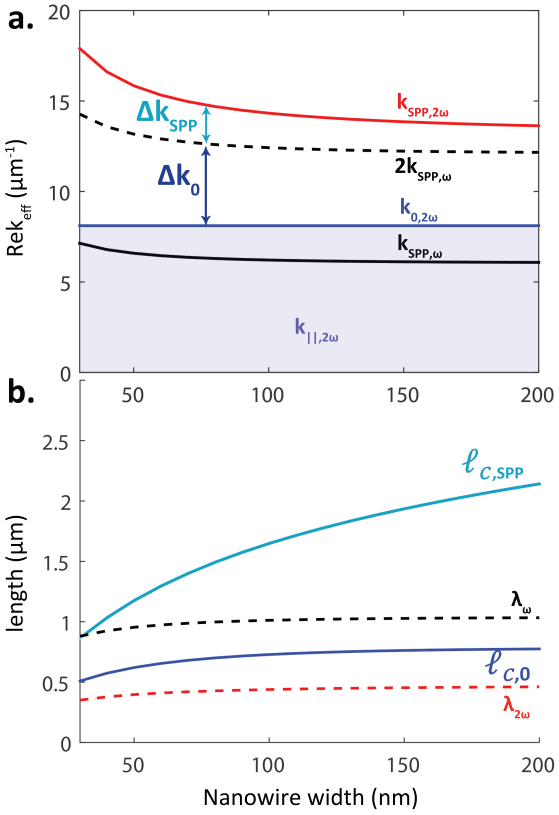

Figure 2.4: Phase-matching on plasmonic NWs. (a) The real part of the wavevector of the ω and 2ω SPPs (black and red curves), and of light in free-space (blue curve), as a function of NW width. The respective phase mismatch is marked by Δk. (b) Coherence lengths of the SPP(ω) to SPP(2ω), $\ell_{c,SPP}$, and SPP(ω) to photon(2ω), $\ell_{c,0}$, as a function of the NW width (solid curves). For comparison, we also show the effective wavelength of the ω and 2ω SPPs (dashed curves).

III requires geometries where $\Delta k_i = 2k_{SPP,\omega} - k_{i,2\omega} = 0$, where $k_{i,2\omega}$ can either be $k_{SPP,2\omega}$ or $k_{//,2\omega} = k_{0,2\omega}\sin\theta$ (as shown in the inset to Fig. 2.3a, and as a purple region in Fig. 2.4a, respectively). In fact, as can be seen clearly in Fig. 2.4a, our NWs do not support phase-matched harmonic generation of either 2ω photons or plasmons. For completeness we note that for NW widths between 227.3 and 670.5 nm, where the mode is leaky (see Fig. 2.3c), phase matching at near-grazing angles in the glass, can occur.

Interestingly, momentum mismatch does not preclude harmonic generation via processes *II* and *III*, it simply limits their efficiency. We therefore calculate the coherence length, $\ell_c = \pi/\Delta k$, which is the distance over which the phase of the

SH light relative to the fundamental changes by π radians. These curves are shown in Fig. 2.4b, along with the wavelength of the 2ω SPPs, $\lambda_{2\omega}$ (and of the ω SPPs, λ_ω for completeness) in dashed curves. Because for these NW widths $\lambda_{2\omega}$ and $\ell_{c,0}$ are comparable and very short, the generated SH light would undergo a rapid phase change and, in total, there would be no build-up of harmonic amplitude; consequently, we expect that process *III* (Fig. 2.3a) will be very weak. In contrast, $\ell_{c,SPP}$ is significantly larger than $\lambda_{2\omega}$ and hence we expect coherent build-up of 2ω SPPs. A signature of this coherence would be oscillations in the SH yield that would be best visible near the beginning of the NW where the maximum SH intensity is greatest. Unfortunately, due to the scattering from the random defects, these oscillations were masked in our measurements. We expect that this coherent buildup of 2ω SPPs would be more visible in near-field measurements. Indeed, preliminary near-field measurements of the spectral content of the light at the surface of the NWs reveal the presence of harmonics. A full near-field study of nonlinear plasmonics on NWs is, unfortunately, beyond the scope of the current work.

2.4 Conclusions and outlook

In summary, we have shown that guided modes of plasmonic NWs can be used for nonlinear optics. Although our NWs are composed of Au, a centrosymmetric material, we observe clear SH and TH signals. We observe a clear dependence of the spatial evolution of the harmonic signal on the NW geometry. Using these spatial maps and numerical simulations, we explore the possible processes by which the harmonics are generated, showing that scattering from LPR at imperfections and the creation of SH SPPs seem to dominate.

In all, the results presented in this chapter demonstrate the promise of nonlinear optics with guided plasmonic modes, potentially opening a new route towards future applications seeking to exploit nonlinear plasmonics [24]. In that vein, we suggest that using hybrid plasmonic NWs by adding a layer with large nonlinear coefficients, such as ITO [95], could greatly increase the harmonic yield. Likewise, by exploiting the inherently large bandwidths supported by our NWs [77, 96], ultrashort pulses can be used to increase the peak intensity without increasing the power consumption, again greatly increasing the nonlinear conversion efficiency. Such approaches could perhaps allow for the observation of weaker $\chi^{(2)}$ or $\chi^{(3)}$ nonlinear effects, such as spontaneous down-conversion or four-wave mixing [40], paving a new route towards the realization of integrated optical circuits for classical or quantum information processing.

Chapter 3

Imaging of electric and magnetic fields near plasmonic nanowires

Near-field imaging is a powerful tool to investigate the complex structure of light at the nanoscale. Recent advances in near-field imaging have indicated the possibility for the complete reconstruction of both electric and magnetic components of the evanescent field. In this chapter we study the electro-magnetic field structure of surface plasmon polariton waves propagating along subwavelength gold nanowires by performing phase- and polarization-resolved near-field microscopy in collection mode. By applying the optical reciprocity theorem, we describe the signal collected by the probe as an overlap integral of the nanowire's evanescent field and the probe's response function. As a result, we find that the probe's sensitivity to the magnetic field is approximately equal to its sensitivity to the electric field. Through rigorous modeling of the nanowire mode as well as the aperture probe response function, we obtain a good agreement between experimentally measured signals and a numerical model. Our findings provide a better understanding of aperture-based near-field imaging of the nanoscopic plasmonic and photonic structures and are helpful for the interpretation of future near-field experiments.

This chapter is based on I.V. Kabakova, A. de Hoogh, R.E.C. van der Wel, M. Wulf, B. le Feber and L.Kuipers, *Imaging of electric and magnetic fields near plasmonic nanowires*, Sci. Rep. **6**, 22665 (2016).

3.1 Introduction

In the past few decades the study of the light field near nanophotonic structures has evolved into an independent research area, revealing new fundamental aspects of light-matter interaction at the nanoscale and propelling research in various applied fields of classical and quantum optics [97–102]. Near fields are difficult to image as they are evanescent in nature and decay within 10s to 100s of nanometers away from the surface, so that they cannot be directly detected by a photodiode or imaged by a camera placed in the far field of the sample. In one of the near-field measurement techniques, known as near-field scanning optical microscopy (NSOM) [103], the detection is usually done by frustrating the evanescent field and converting it into far-field radiation by means of a scattering probe (s-NSOM) or a light-collecting aperture probe (a-NSOM). In any case, a probe is brought close to the surface of the structure and scanned across to map the near-field distribution. Typically such probes have dimensions of a fraction of a wavelength, enabling to measure fields with a resolution beyond the diffraction limit.

Near-field imaging is a particularly important characterization method for objects of a certain type: those with a nanoscopic size, and those that are intrinsically lossy [104, 105]. This is because many other measurement types, e.g. transmission measurement, are not applicable in this situation. It is, however, well known that the interpretation of an NSOM measurement is not always a straightforward task and several common artifacts of the near-field imaging have been previously pointed out [106]. It is therefore crucial to understand the process of the image formation for a variety of nanophotonic structures of different complexity and sizes.

Plasmonic nanostructures, being deeply subwavelength and lossy, are commonly investigated in the near-field regime [107–109]. So far several geometries, including plasmonic wires and tapers [109–111], nanoparticles [112] and holes [113–116], have been studied using NSOM. In these studies the signal collected by the near-field aperture probe was always attributed to the electric field. However, it has recently become apparent that the aperture probe of the near-field microscope is sensitive not only to the electric field but also to the magnetic field [117–123]. A study performed on photonic crystal waveguides (PhCWs) has shown that the probe sensitivity to the electric field component near a PhCW is approximately the same as that to the magnetic field. Both the electric and magnetic fields were observed to contribute to the process of image formation by the near-field microscope [117]. It is therefore important to treat information obtained through the near-field imaging with care and recognize the contributions of both fields in the measured signals.

In this chapter, we present a detailed study of the image formation in the a-NSOM measurement of plasmonic nanowires. Our study exploits the optical reciprocity theorem, the approach which has previously been used for PhCWs and that has resulted in the successful reconstruction of electric and magnetic components of the near field [117]. By considering the electric and magnetic field components of the nanowire mode as well as the complex response function of the aperture probe, we are able to reproduce the measured data with a good agreement. As for PhCWs,

here we find that the probe sensitivity to the electric field is approximately equal to its sensitivity to the magnetic field. This leads us to the conclusion that the signal measured in the near-field microscopy experiments on plasmonic nanostructures is a combination of both fields, electric and magnetic, in other words the magnetic field cannot be ignored.

Next we analyze how the probe's geometry influences the outcome of the imaging process. Two features need to be considered: (1) the complex nature of the probe's response, i.e. the probe cannot be approximated as a simple filter, and (2) the geometrical size of the probe's aperture being a factor of 2 larger than the nanowire width. As a result, the signal collected by the probe does not represent the electro-magnetic field of the nanowire mode at a single location, e.g. at the center of the aperture, but is proportional to the overlap integral of the local field and the probe's response function. As a result, the separation of the measured signals into individual electric and magnetic components becomes non-trivial. Our findings present a deeper understanding of the image formation in a-NSOM and the limitations associated with near-field measurements of photonic and plasmonic objects of nanoscopic sizes.

3.2 Numerical simulations

For the numerical modeling we used FDTD Solutions by Lumerical, to simulate the propagation of SPPs in our nanowire structure. We chose perfectly matched layers as the condition on all boundaries of the model. The nanowire mode was calculated using the Mode Expansion Monitor. This mode then was propagated along the length of the nanowire using a home-build code in Matlab to obtain in-plane field maps shown in Fig. 3.2. The simulation took into account the change of the tip's height during the measurement scan. Since the scan was made in the 'constant distance' mode, the probe followed the topography while scanning above the sample. For the simulation of the reciprocal fields we used the finite difference method implemented in COMSOL. The overlap integrals associated with Eq. 3.3, 3.2 and 3.1 were calculated using a home-build code in Matlab.

3.3 Near-field microscopy of plasmonic nanowires

In this work we use a scanning near-field microscope, operating in collection mode. This setup is capable of measuring the complex electro-magnetic field in planes above the sample by raster-scanning the aperture probe and collecting the signal collected by the probe [120]. The probe consists of an optical fiber taper with a diameter of approximately 200 nm and a 150 nm-thick aluminum coating. Such a probe diameter of $\lambda/7$ typically presents a trade-off between the resolution and the signal-to-noise ratio of the measurement. The resolution of the imaging technique is mostly determined by the probe's aperture.

The plasmonic nanowire is fabricated in a 50 nm-thick layer of gold, that is deposited on top of a glass substrate (Fig. 3.1a and b). The details of the sample

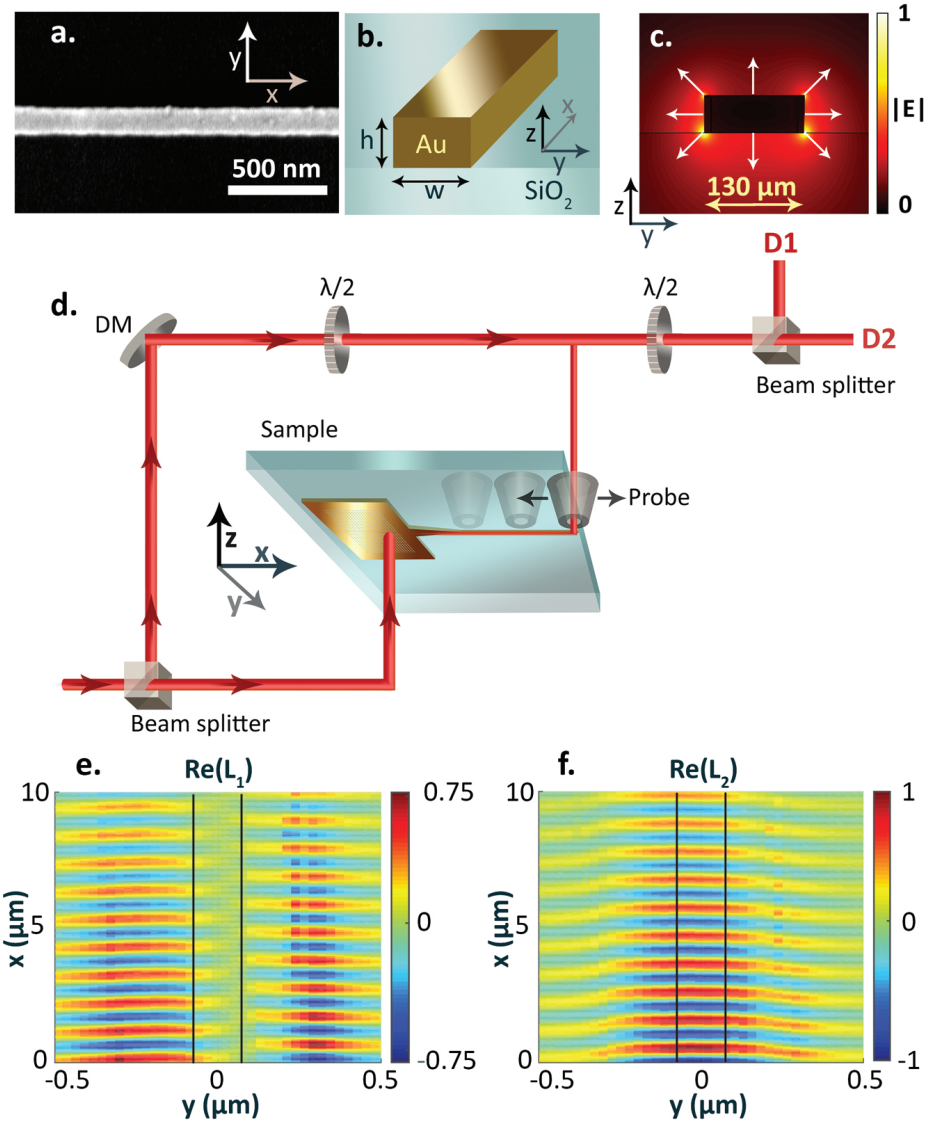

Figure 3.1: (a) Scanning electron microscope image of the beginning of the Au nanowire, (b) Schematic of a gold nanowire placed on a glass substrate. The nanowire is 130 nm in width (w) and 50 nm in height (h). (c) The calculated normalized intensity of a plasmonic mode, with arrows indicating the direction of the transverse electric field. The calculations are performed with COMSOL (d) Schematic of the scanning near-field microscope setup: DM - dielectric mirror, D1 and D2 are detectors that record y- and x-polarized electric fields.(e-f) Real parts of the complex signals L_1 and L_2 measured by detectors D1 and D2, respectively, for the probe scanning in the plane xy at the height 20 nm above the wire. The signal amplitudes are normalized to the maximum amplitude of L_2. Black lines indicate edges of the nanowire.

fabrication are described in Appendix A. Briefly summarized, the sample consists of a 2D hole array, terminated by a 20 μm-long taper, which funnels into a 130 nm-wide and 50 μm-long nanowire (schematic of the nanowire is presented in 3.1b. We use the hole array to excite surface plasmon polariton waves and direct them towards the taper. The distance between the holes and the hole radius is optimized for coupling of 1550 nm light. The adiabatic taper converts the initial waveguide mode, which is mainly confined to the interface between the glass substrate and the bottom surface of the gold taper, into a Sommerfeld-like nanowire mode [124]. At the chosen width and height of the nanowire, there is only one mode supported by it. The calculated spatial distribution of the normalized intensity of the electric field in such a plasmonic mode is depicted in Fig. 3.1c. This mode has approximately 'radial' polarization in the yz plane and has intensity maxima at the corners of the nanowire. The structure of this mode therefore resembles a Sommerfeld wave in a cylindrical metal wire and has been reported previously [111].

The NSOM probe, sensitive to the electro-magnetic near field, collects an optical signal for each probe position above the sample. This signal is then delivered by the optical fiber to detectors D1 and D2. A detailed explanation about our near-field setup is given in section 1.5; a simplified picture is sketched in Fig. 3.1d. In summary, our near-field microscope allows the measurement of both amplitude and phase of the evanescent field by implementing an interferometric approach, in which a signal collected from the sample is combined with a reference signal. By introducing polarization optics into the reference branch of the setup, we are able to distinguish between the orthogonal components of the in-plane near field. As has been discussed previously [117, 120], each detector provides a signal representation of a combination of the in-plane electric and magnetic field components. We ensure that all signal resulting from y-oriented electric field above the nanowire, E_y^{wire}, is collected by detector D1, and likewise E_x^{wire} is detected by D2. Conversely, any signal that arises from y-oriented magnetic field, H_y^{wire}, is detected by D2, and H_x^{wire} is picked up by D1.

Figures 3.1e and f present the real parts of the complex signals L_1 and L_2, which are constructed from the signals measured by the two detectors D1 and D2 respectively. As presented in Fig. 3.1c, $L_1(\mathbf{r})$ and $L_2(\mathbf{r})$ result from the interference between the near-field signal at each position $\mathbf{r}$ and the reference signal, and can be written as $L_{1,2}(\mathbf{r}) = A_{1,2}(\mathbf{r})e^{(i\phi)}$, where ϕ is the phase difference between two arms of the interferometer. The height of the aperture probe for this set of measurements was kept approximately at 20 nm above the sample. We find that the y-polarized signal (L_1) is anti-symmetric and has a node at $y = 0$, whereas the x-polarized signal (L_2) is symmetric and has a non-zero magnitude at the center of the wire. This agrees with the description of the mode structure for nanoscale plasmonic nanowires reported previously [111]. The maximum amplitude of the signal L_2 is slightly larger than that of L_1. The presence of a significant signal L_2, which is associated with longitudinally-polarized fields, demonstrates the profound deviation of the highly confined nanowire mode from a transverse wave. A small tilt is noticeable to the left side in the measurement data, which can be clearly seen in Fig. 3.1f. It is caused

by a slight misalignment of the wire with regard to the scanning x axis, but it is not critical for the rest of the discussion.

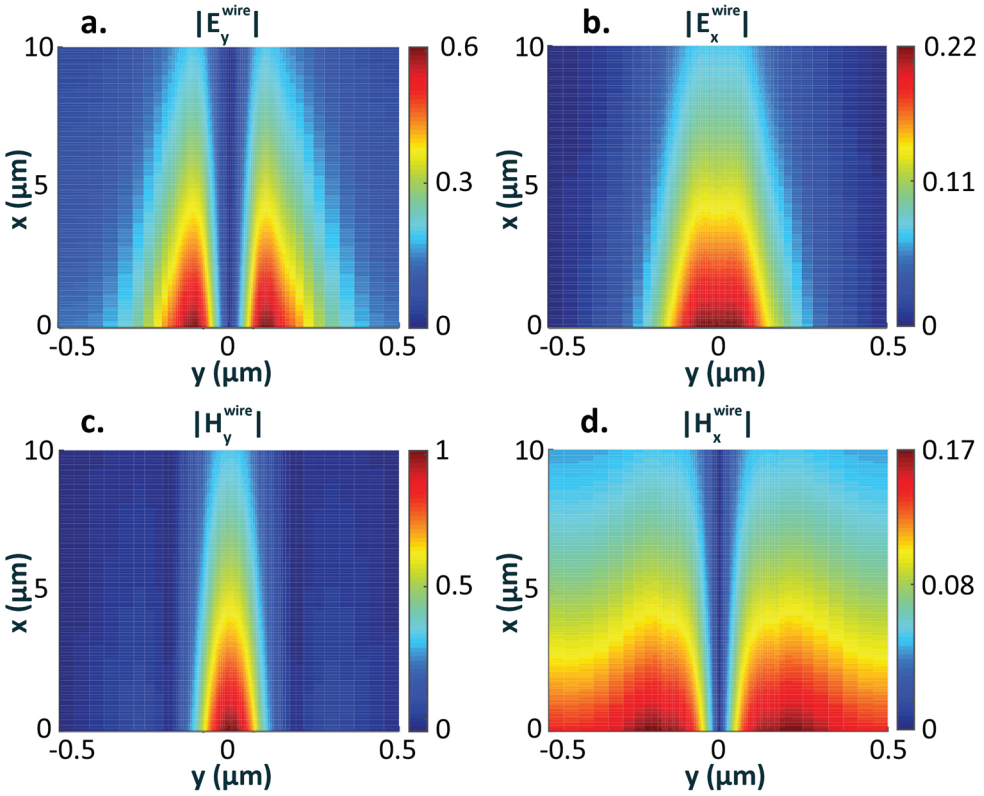

Figure 3.2: Simulated electric and magnetic field amplitudes for the four in-plane components at a height of z=20nm in the plane xy for a gold nanowire with a width of $w = 130$ nm. The field amplitudes are normalized to the maximum amplitude of $|H_y^{wire}|$ component.

Next we compare our measured signals L_1 and L_2 to the fields obtained by numerical modeling of an SPP wave, propagating in a gold nanowire with a width of 130 nm. For the simulation we use the material parameters of gold and glass from a standard source [125] at the wavelength of interest. We simulate the propagation of SPPs using the finite-difference time-domain (FDTD) method. Figure 3.2 shows maps of the calculated electric and magnetic field components in the xy plane, 20 nm above the surface. From the amplitude and the phase (the latter, not presented in Fig. 3.2) information we conclude that the fields E_y^{wire} and H_x^{wire} are antisymmetric with respect to the xz-plane through the center of the wire, similar to the signal L_1 measured by detector D1 (Fig. 3.2d). The fields E_x^{wire} and H_y^{wire}, however, are symmetric, similar to the signal L_2 measured by detector D2 (Fig. 3.1e). Magnetic fields

in Fig. 3.2 (c and d) are multiplied by the vacuum impedance $Z_0 = \sqrt{\mu_0/\epsilon_0}$, where μ_0 and ϵ_0 are vacuum permeability and permittivity, respectively. Multiplication brings the fields to the same units of Volt per meter for comparison. In the calculations we find that the largest field component is the y-polarized magnetic field (H_y^{wire}), indicating that magnetic fields are not negligible. We also note that the distributions of the electric and magnetic fields share the same features, such as symmetry, but are not exactly the same. For example, E_y^{wire} is more confined to the nanowire edges than H_x^{wire}. Additionally, E_y^{wire} has two maxima, whereas H_y^{wire} has only one maximum at the center of the wire. These observations together with the fact that a-NSOM has been previously shown to measure magnetic fields [117,121], suggests that all in-plane electro-magnetic field components could be important to the image formation.

The question we have to answer next is how these fields combine inside the probe to produce the signals L_1 and L_2. We immediately see that this is not a trivial question taking into account the size of the nanowire (130 nm), the complex structure of the nanowire's mode, and the size of the probe's aperture (200 nm). Naively, we might expect the probe to act as an integrating filter with a Gaussian-like response. Due to the aperture being larger than the nanowire itself, such a filter applied to the intrinsic fields of the nanowire would lead to a blurring effect, such that the measured signals would have a larger spread in space than the intrinsic nanowire fields. Fortunately, there is no need for speculation as we can use a rigorous approach for the signal reconstruction based on the optical reciprocity theorem [126].

3.4 Optical reciprocity theorem

It is known that the optical reciprocity theorem can be used to explain near-field data collected during a measurement [126, 127]. This theorem postulates that the detected signal from a source will be the same if the source and the detector are exchanged [128]. Recently, the reciprocity theorem has been successfully applied for the reconstruction of electro-magnetic fields above a $W1$-type PhCW [117]. In this chapter we will follow the same approach to explain the measurement of evanescent fields associated with the plasmonic nanowire mode.

The reciprocity theorem relates the fields measured by the probe to the fields that would be transmitted through the probe if a dipole source were placed at the location of the detector. Mathematically, when we neglect any back-action from the probe, the expected signals at detectors D1 and D2 can be expressed as

$$\begin{aligned} L_1(\mathbf{r}) &\propto \int_S \left[\mathbf{E}^{\mathbf{wire}}(\mathbf{r}) \times \mathbf{H}^{\mathbf{rec,y}}(\mathbf{r}) - \mathbf{E}^{\mathbf{rec,y}}(\mathbf{r}) \times \mathbf{H}^{\mathbf{wire}}(\mathbf{r})\right] \cdot d\mathbf{S}, \\ L_2(\mathbf{r}) &\propto \int_S \left[\mathbf{E}^{\mathbf{wire}}(\mathbf{r}) \times \mathbf{H}^{\mathbf{rec,x}}(\mathbf{r}) - \mathbf{E}^{\mathbf{rec,x}}(\mathbf{r}) \times \mathbf{H}^{\mathbf{wire}}(\mathbf{r})\right] \cdot d\mathbf{S}, \end{aligned} \tag{3.1}$$

where $\mathbf{dS}$ represents the normal vector of the surface S in the xy-plane above the nanowire. Here $\mathbf{r}$ is the position of the probe tip above the nanowire. From Eq. 3.1 and the definition of $d\mathbf{S} = \mathbf{z}dS$ we conclude that the only non-zero terms under

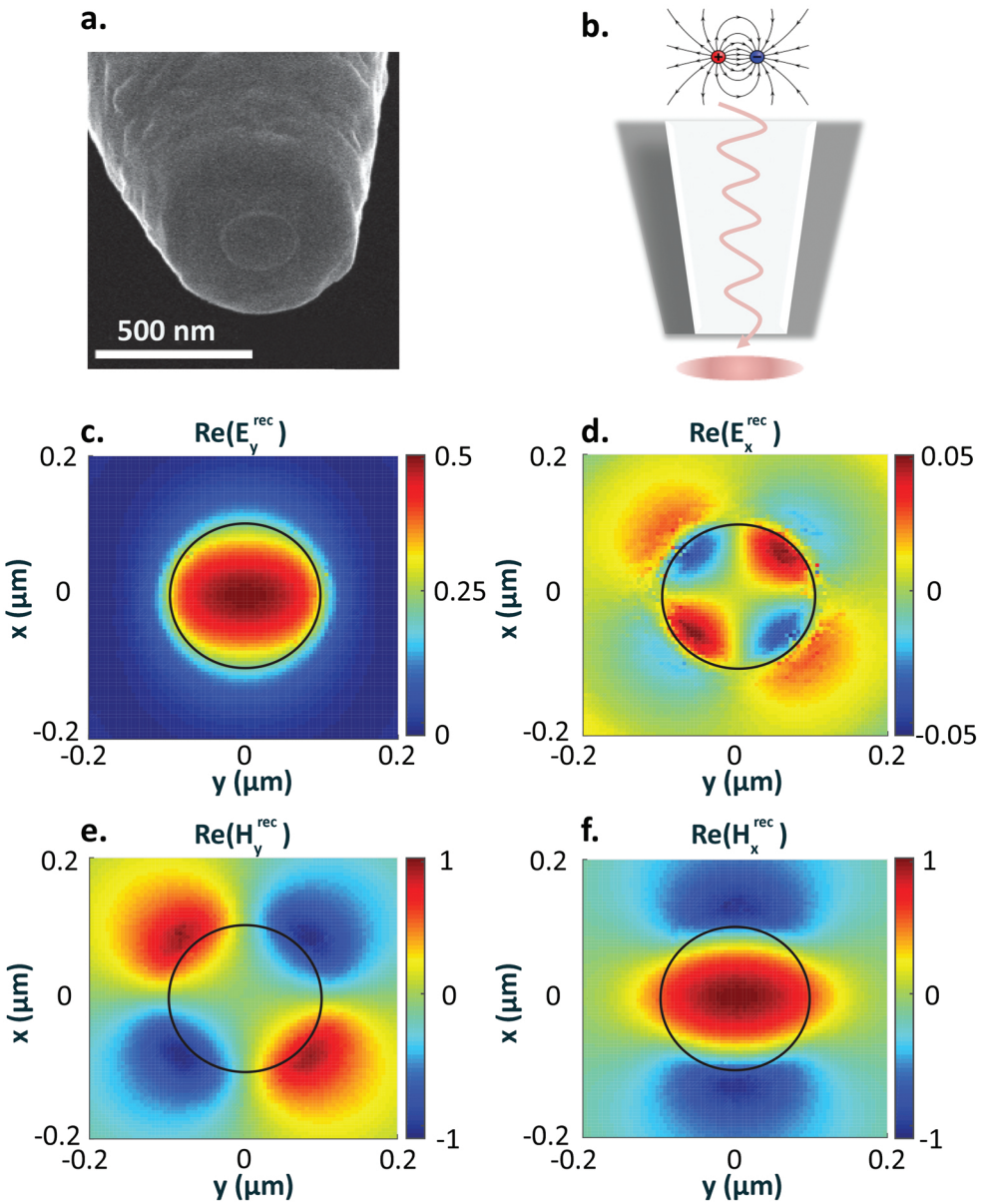

Figure 3.3: (a) SEM image of the aperture probe, (b) Illustration to the calculation of reciprocal fields: a dipole source placed at the detector position emits light that is imaged below the aperture, (c-f) Reciprocal fields in the plane xy calculated below the aperture probe, arising from the y-oriented dipole source. The magnetic fields are multiplied by the vacuum impedance $Z_0 = \sqrt{\mu_0/\epsilon_0}$ and all field amplitudes are normalized to the maximum amplitude of the $Re(H_y^{rec})$ component. The black circle indicates a cross-section of the aperture.

the integral are those constructed by the reciprocal and wire fields in the plane xy, since the vector product of the out-of-plane fields with $d\mathbf{S}$ is zero. $\mathbf{E^{wire}}$ and $\mathbf{H^{wire}}$ indicate the calculated fields of the nanowire mode above the gold nanowire due to the propagating plasmonic mode. $\mathbf{E^{rec}}$ and $\mathbf{H^{rec}}$ are, the so-called, reciprocal fields, which are calculated just below the probe and which result from an x- or y-polarized dipole source placed at the detector position [128]. We note that $\mathbf{E^{rec}}$ and $\mathbf{H^{rec}}$ are virtual fields as they are not present in the actual measurement. They, however, are useful for calculations and have a meaning of the probe's complex response function. The concept of the reciprocal fields is illustrated in Fig. 3.3, where a shows a SEM image of the actual microscope tip and (b) illustrates the model which we use to calculate reciprocal fields. Eq. 3.1 suggests that the reciprocal magnetic fields reflect the sensitivity of the probe to the electric field components of the wire as

$$\eta_E^i(\mathbf{r}) \propto \int_S (\mathbf{E^{wire}}(\mathbf{r}) \times \mathbf{H^{rec,j}}(\mathbf{r})) \cdot d\mathbf{S}. \tag{3.2}$$

Similarly, the reciprocal electric fields reflect the probe's sensitivity to the wire's magnetic fields

$$\eta_H^i(\mathbf{r}) \propto \int_S (\mathbf{E^{rec,j}}(\mathbf{r}) \times \mathbf{H^{wire}}(\mathbf{r})) \cdot d\mathbf{S}. \tag{3.3}$$

where $i = 1, 2$ denotes the detector number and $j = y, x$ shows the respective orientation of the dipole source. For $i = 1$ the dipole is oriented along y ($j = y$), whereas it is oriented along $j = x$ for $i = 2$.

To calculate the reciprocal fields $\mathbf{E^{rec}}$ and $\mathbf{H^{rec}}$ we use the finite element method and approximate the near-field probe by a glass hole (diameter $d = 200$ nm) in a thin, 150 nm aluminum layer. This approximation is justified, since the thickness of the aluminum layer on the probe is large enough to have no significant electro-magnetic fields outside the metal coating when the source and the detector are exchanged. It has also been shown that the fields produced by such a hole closely resemble the transmitted fields of a real aperture probe [129]. As strongly suggested by recent work [130, 131], the sensitivity of an aperture probe can be controlled through the thickness of the metal coating. This situation is particularly important for probes with thin metal claddings. In this work, however, the metal cladding is relatively thick and we focus on the extent to which the detected field components can be separated so that a local description of the field coupling to the probe is valid.

Figure 3.3c-f shows the calculated reciprocal fields $\mathbf{E^{rec}_{y,x}}$ and $\mathbf{H^{rec}_{y,x}}$ below the tip of the probe, arising from a y-oriented dipole source. The magnitudes of these fields are normalized to the maximum of $\mathbf{H^{rec}_{y}}$ to simplify the comparison. We observe that the distribution of $\mathbf{E^{rec}_{y}}$ resembles a slightly squeezed Gaussian beam, whereas the other three components have a more complex structure. It would therefore be erroneous to expect the probe to behave as a simple integrating filter. We also note that the reciprocal magnetic components $\mathbf{H^{rec}_{y,x}}$ are stronger than the electric counterparts. This is an important observation and we expect it to play a role in the probe's sensitivity to the electric and magnetic fields. After obtaining the reciprocal fields

we can now convolve them with the wire fields using the recipe given by Eq. 3.1. By doing so we are able to calculate the signals L_1 and L_2, measured by detectors D1 and D2, at every position of the probe in the xy plane above the nanowire.

The result of this numerical procedure is presented in Fig. 3.4, where the calculated signals using the reciprocity theorem are shown in (a-c), and the measured signals are given in (b-d) for the comparison. We notice that the calculated signals (Fig. 3.4a-c) exhibit a very good agreement with the measurement (Fig. 3.4b-d). A slight asymmetry is observed in the measured data, which can be attributed to a small degree of polarization mixing, i.e. non-perfect separation of orthogonal polarizations in the experiment. This is, however, hard to avoid since the polarization of light in an optical fiber is susceptible to drifts due to temperature and stresses [132].

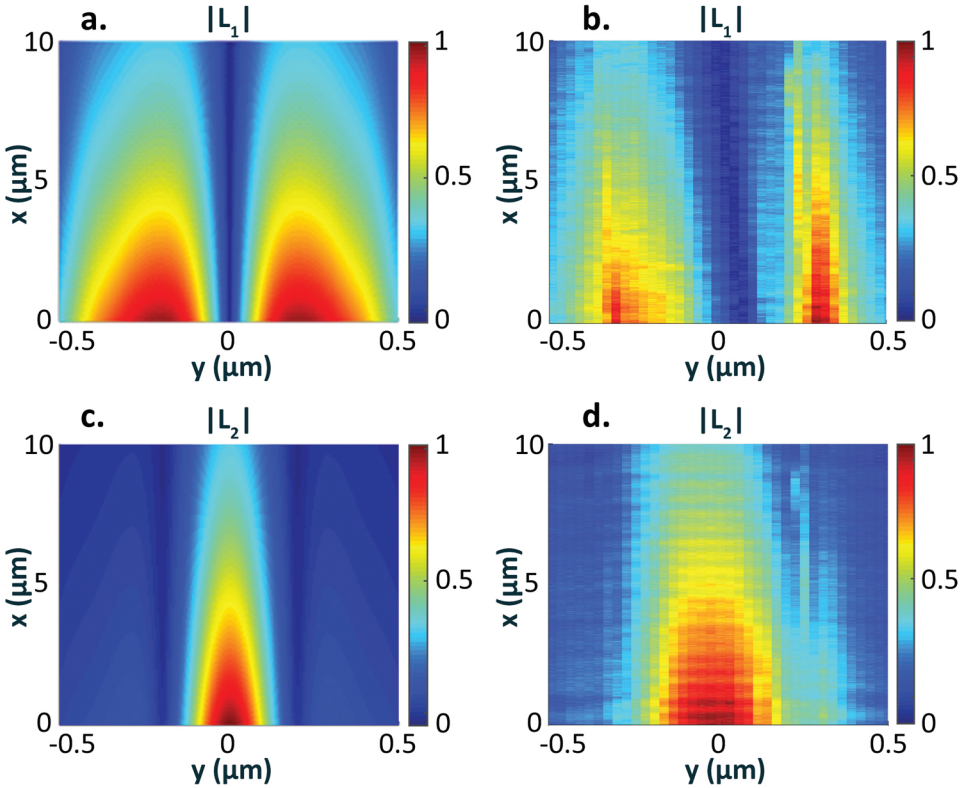

Figure 3.4: Reconstructed (a-c) and measured (b-d) signals at detectors D1 and D2. The amplitudes of all signals are normalized to their maxima.

One of the important conclusions that can be drawn after analyzing Fig. 3.4a and b: the field map detected by D1 (as well as its calculated version) looks markedly different from the individual field components E_y^{wire} and H_x^{wire}. Apart from the width

of the lobes, the most striking difference is the distance between the lobes. In fact, the separation between the lobes (measured as the distance between the field maxima) in Fig. 3.4c is close to 600 nm, which is almost 3 times the separation between the lobes of the field E_y^{wire} in Fig. 3.2. In fact, it can be shown that the signal L_1 in these measurements cannot be constructed as a linear superposition of the respective electric and magnetic field components, $L_1 = \alpha_1 E_y^{wire} + \beta_1 H_x^{wire}$, where α_1 and β_1 are complex constants. This finding is contrary to the experimental observations while mapping the electric and magnetic fields above a photonic crystal waveguide [117]. Apparently, the structure of the fields around a nanophotonic structure combined with the complexity of the near-field coupling to the probe, see e.g. Eq. 3.1, makes that the simple separation in a superposition of individual **E** and **H** components can only be performed for certain conditions.

3.5 Probe sensitivity to electric and magnetic fields near plasmonic nanowire

Another piece of information that we are able to retrieve using the reciprocity theorem is the sensitivity of the probe to the electric and magnetic field components of the nanowire's near field. From Eq. 3.2 and Eq. 3.3 it follows that the probe sensitivity depends not only on the reciprocal fields of the probe itself, but also on the fields the probe is measuring. This means that, in principle, the probe's sensitivity can differ depending on which structure it measures: a plasmonic nanowire, a hole or a photonic crystal. This is an important property of the near-field imaging that originates from the complexity of the collection process as is evident from Eq. 3.1. Using Eq. 3.2 and eq. 3.3 we finally calculate the sensitivity ratio to the magnetic and electric fields, averaged across the calculation area, to be $\langle \eta_H^1 \rangle / \langle \eta_E^1 \rangle = 1.058$ for the detector D1 and $\langle \eta_H^2 \rangle / \langle \eta_E^2 \rangle = 1.32$ for the detector D2. We find that the ratio of sensitivities varies for each detector, but overall is slightly larger than 1, meaning that the probe is slightly more sensitive to the magnetic near field than to the electric one. From Eq. 3.2 and 3.3 it becomes clear that a higher sensitivity of the detector to the magnetic field is obtained when the integrated electric field of the probe ($\mathbf{E}^{\mathbf{rec}}$) is higher than the probe's integrated magnetic field ($\mathbf{H}^{\mathbf{rec}}$).

3.6 Discussion

Our analysis of the near field, associated with the propagating mode in a plasmonic nanowire, has shown that the contribution of the magnetic field to the measured signals cannot be neglected, because it is equal to or in some instances even larger than the contribution of the electric field [116,121]. We have also determined that the probe sensitivity to the magnetic field is approximately equal to the probe sensitivity to the electric field. A similar situation was reported for the near-field imaging of PhCWs, in which the probe sensitivity ratio $\langle \eta_H \rangle / \langle \eta_E \rangle \approx 1$ was found for most of the

probe sizes and independent of the height of the probe above the crystal [117].

It might seem, however, a puzzling outcome that the ratio of sensitivities in our system differs for the two detectors ($\langle \eta_H^1 \rangle / \langle \eta_E^1 \rangle = 1.058$ and $\langle \eta_H^2 \rangle / \langle \eta_E^2 \rangle = 1.32$), albeit modestly. At first glance, it seems nonphysical as the probe used in the measurements was cylindrically symmetric. Moreover, in the simulations the probe was assumed to be symmetric, which was reflected in the calculation of the reciprocal fields (the reciprocal fields calculated for a y-polarized dipole source are a projection-swap version of the fields calculated for x-polarized dipole source). Thus, the different value of the sensitivity ratio for the two detectors would seem impossible, if the sensitivity of the probe were to depend on the probe's properties only. The sensitivity of the probe, however, is also determined by the properties of the fields it is measuring. This circumstance allows for a perfectly symmetric probe in a perfectly symmetric detection scheme to have different sensitivity ratios in the two orthogonal field directions.

As we discussed earlier, due to the complex nature of the image formation process, the link between the local intrinsic field of the nanowire and the signal measured at this same location is nontrivial. Therefore, it is not possible to represent the signals L_1 and L_2 as a linear superposition of the nanowire electric and magnetic fields, and consequently separate **E** and **H** fields in the measurement. This is in contrast to the near-field measurement of PhCWs [117, 120] and of a plasmonic aperture [116] reported previously. In the situation with photonic crystals it was actually possible to fit the measurement at nine different heights above the crystal by forming linear superpositions of the electric and magnetic fields using only 2 fitting parameters, the probe sensitivities. In those experiments, the period of the photonic crystal was 420 nm and the hole diameter was 240 nm [117], somewhat larger than the nanowire dimensions and comparable to the probe's aperture.

Another point of difference in the present work is the structure of the wire's mode with two of the field projections (E_y^{wire} and H_x^{wire}) being antisymmetric. We expect that the field separation problem can be solved if a smaller probe is used. In principle, probes with aperture diameters of approximately a 100 nm can be fabricated. Such probes, however, prove to be impractical since they typically have a very poor transmission and coupling efficiency. Another solution could be to use a scattering probe [133], with a diameter on the order of tens of nanometers [134], instead of a collecting aperture probe. Care must be taken, however, to ensure that the interaction of the scattering probe with the sample is minimal and can be described by the first order perturbation theory [135].

In summary, we have performed near-field imaging of plasmonic nanowires using a homebuilt polarization- and phase-sensitive near-field microscope operating in a collection mode. The analysis of the measured signals has shown that the collected light is the combination of electric and magnetic fields, and the magnetic field contribution is significant. We have developed a model of the image formation in our microscope, based on the optical reciprocity theorem. This theorem allows us to include the response of the aperture probe into consideration and calculate the signals measured by the detectors. We find a very good agreement between our measurement and the

modeling results. Overall, our findings indicate the importance of a careful analysis of the near-field measurement data and consideration of both electric and magnetic contributions of the near field. The identification of the strong magnetic contribution to the near-field signals measured in the vicinity of plasmonic nanostructures paves the way towards studies of magnetic effects at optical frequencies [136–138].

Chapter 4

Optical singularities in plasmonic fields near single subwavelength holes

We identify phase and polarization singularities in near-field measurements and theoretical modeling of the electric near-field distributions that result from the scattering of surface plasmon polaritons from single subwavelength holes in optically thick gold films. We discuss properties of the singularities, such as their topological charge or the field amplitudes at their locations. We show that it is possible to tune the in-plane field amplitude at the positions of the polarization singularities by three orders of magnitude simply by varying the size of the hole or the incident plasmon beam width.

This chapter is based on A. de Hoogh, N. Rotenberg and L. Kuipers, *Optical singularities in plasmonic fields near single subwavelength holes*, J. Opt. **16**, 114004 (2014).

4.1 Introduction

The creation of structured light fields that can carry angular momentum is a topic of intense research. In the far field, beams can carry either spin or orbital-angular momentum, as is the case for, for example, vortex or circularly polarized beams [30, 36, 139–142]. Such beams are important to applications in fields such as nanomanipulation [143, 144], biosensing [145], or quantum optics [146]. Recently, there has been a push to create angular momentum carrying light fields at the nanoscale [147], which would allow on-chip applications in the aforementioned fields.

At the nanoscale, properties of a light field, such as the amount of angular momentum that they carry, can be local quantities. That is, unlike in the far-field where the entire beam can carry angular momentum, in the near field distinct regions can have angular momentum while the entire distribution is neutral [37], [148]. In the near field, regions with local angular momentum are often associated with optical singularities, either phase or polarization singularities in the cases of orbital- or spin-angular momentum, respectively. And, since near fields are strongly controlled by geometry, it is possible to design and fabricate structures, such as photonic crystal waveguides [37] or slits [28], whose nanoscopic light fields contain optical singularities.

In this chapter we introduce a new system where optical singularities can be found, namely a subwavelength hole on a metallic film as it scatters surface plasmon polaritons (SPPs). Unlike previous plasmonic systems whose fields are known to contain singularities [28], in our case we expect that the optical singularities will be found in the plane of the film. Our calculations do, in fact, reveal a plethora of both phase and polarization singularities in this plane, and we discuss their properties. We control the position of the singularities relative to the hole by tuning the size of either the incident SPP beam or the hole. Lastly, we show preliminary polarization- and phase-resolved near-field measurements of the scattering of SPPs from a subwavelength hole on a gold film, in which we indeed observe polarization singularities.

4.2 Plasmonic scattering and phase singularities

The scattering of light from plasmonic nanostructures, such as subwavelength holes, results in complex electric field distributions [51, 52]. As these field distributions in the neighborhood of the hole are highly structured we can be hopeful that they might contain optical singularities [15, 67]. The complexity of the field distribution arises from the fact that these distributions are composed of two different, interfering surface waves: the incident SPP beam propagating along the metal interface, $\mathbf{E}^{in}$, and the scattered SPP, $\mathbf{E}^{s}$. For our situation of an SPP beam scattering from a hole in a gold film, the incident beam profile is a Gaussian, given by Eq. 1.21 [51]. The scattered SPP wave can be written as Eq. 1.23 [52], as described in section 1.4.3.

As sketched in Fig. 4.1, the total field in the region surrounding the hole, at any position $r = (x, y)$ in a plane at height z, is the superposition of the incident and scattered field. That is, $\mathbf{E}^{T} = \mathbf{E}^{in} + \mathbf{E}^{s}$, where the scattered field is, in this model,

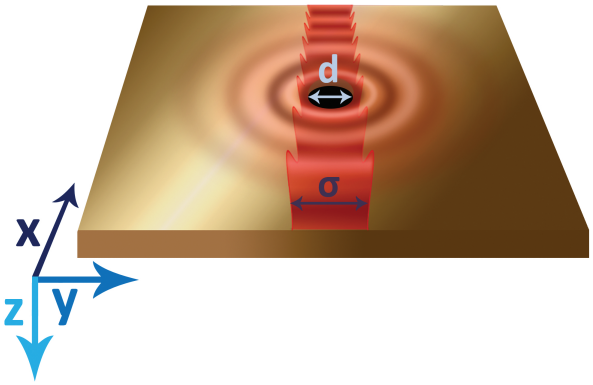

Figure 4.1: Schematic of our nanoplasmonic structure, including the coordinate system. An optically thick gold film supports a Gaussian SPP beam (σ FWHM), that scatters from a single subwavelength hole of diameter d.

radiated by the dipoles that are induced in the hole by the incident field. Here, $r_0 = (x_0, y_0)$ is the position of the hole, and r' represents the displacement from r_0. Due to the symmetry of our nanophotonic system, these dipoles are $p_z = \alpha_E \mathbf{E}_z^{in}(r_0)$ and $m_y = \alpha_H \mathbf{H}_y^{in}(r_0)$, where the polarizability $\alpha_{E(H)}$ that determines the response of the hole to the incident electric (magnetic) field has been calculated [52] and measured [51].

Figure 4.2 presents an example of the calculated amplitude, $A(r)$, and phase, $\theta(r)$, of the vector components of $\mathbf{E}^{in}$ and $\mathbf{E}^{s}$ over an area of $40 \times 40\ \mu m^2$, at a height of 10 nm above the surface of the gold film. This calculation was performed for light with $\lambda = 1550\ nm$, where $\varepsilon = 155.1 + 11.3i$ [50]. In Fig. 4.2, $\mathbf{E}^{in}$ is a Gaussian SPP beam with a FWHM $\sigma = 5\ \mu m$, which propagates in the positive x direction and is centered around y = 0. As expected for an SPP beam at this frequency on gold, the strongest electric field component is polarized out-of-plane, and hence E_z^{in} (Fig. 4.2e) is roughly ten times larger than the longitudinal in-plane component E_x^{in} in (Fig. 4.2a). Because $\mathbf{E}^{in}$ has a Gaussian shape, and is not a plane wave, we also find a non-zero distribution to the transverse electric field component E_y^{in} (Fig. 4.2c), which will increase in magnitude for beams with smaller widths. The scattered field, shown in Fig. 4.2b, d, and f, is centered about the position of the hole at $r_0 = (0, 0)$. In these maps, the hole is taken to have a diameter of 800 nm, and the corresponding polarizabilities are $\alpha_E = 0.0448 + 0.0083i$ and $\alpha_H = 0.1301 + 0.1670i$ [52]. We observe a subtle asymmetry in the amplitude of the scattered field, with respect to the x axis, which arises due to the interference of the radiation emitted by the electric and magnetic dipoles [51]. This directionality of the scattered field can, in principle, be controlled either through the polarizability of the hole (e.g. by changing the hole geometry), or the phases of the incident field (e.g. by changing r_0 relative to the incident field, or using a different $\mathbf{E}^{in}$). In Fig. 4.2, we observe that the scattering is

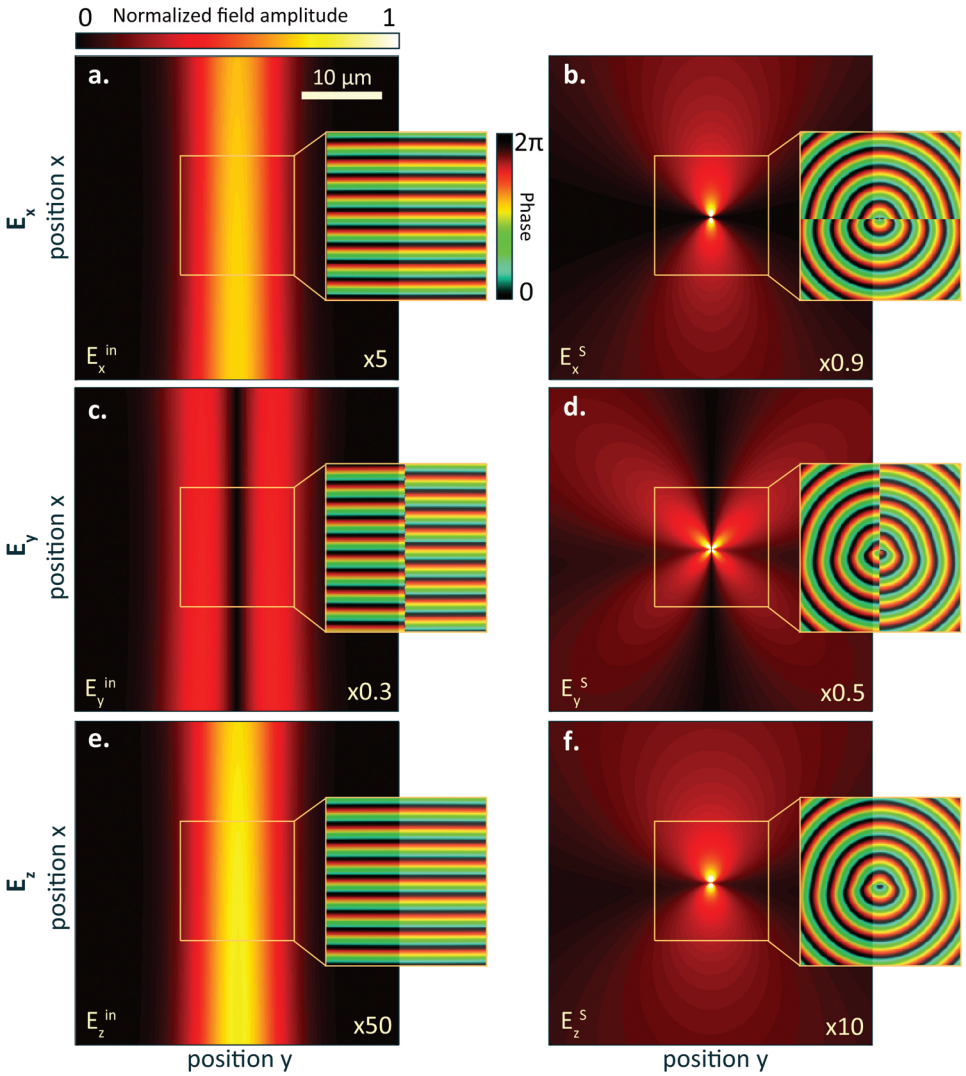

Figure 4.2: (a), (c), (e) Incident and (b), (d), (f) scattered electric field amplitude maps for a $\sigma = 5$ μm SPP beam scattering from an 800 nm hole. The beam propagates in the upwards direction, and the hole is located in the center of each map. The insets show the phase of each respective field component in a 15 x 15 μm^2 area that is centered on the hole. The relative amplitudes of the different components are given in the bottom right corner of each panel.

strongest in the forward direction.

In addition to $A(r)$, we also present $\theta(r)$ for both the incident and scattered field, in the insets to Fig. 4.2. The phase of the incident field components (Fig. 4.2a, c, and e) increases monotonically in x, as expected for a beam traveling in that direction. In contrast, the phase of the scattered field components (Fig. 4.2b, d, and f) grows with the displacement from the hole position r', as expected for a circular wave radiating away from the hole. We now look for phase singularities in the fields shown in Fig. 4.2. Phase singularities are points where $\theta(r)$ is undefined, and are generally found by looking for positions where different lines of constant phase intersect. Their intersection can only occur at points where the amplitude of the associated field is identically zero. The field maps shown in Fig. 4.2 contain no phase singularities, although some components (E_y^{in}, E_x^s, and E_y^s) do contain lines of undefined phase, known as wave disclinations, about which the phase flips. In our system, these disclinations are found on axes of symmetry, for example along $y = 0$ for E_y^{in} (Fig. 4.2c) or $x = 0$ for E_x^s (Fig. 4.2b).

While we find no phase singularities in the individual electric field components, such singularities are known to occur in systems where (two) different waves interfere [67]. In Fig. 4.3, we show both $A(r)$ and $\theta(r)$ for the three components of $\mathbf{E}^T$, made by adding the fields shown in Fig. 4.2. In the amplitude maps of $\mathbf{E}^T$ (Fig. 4.3a, d, and g) we observe parabolic fringes which arise from the interference of the incident SPP wave and the wave scattered by the hole. In fact, it is within these fringes that we can find positions where the incident and scattered waves have equal amplitudes and opposite phases, and hence the total field amplitude is zero. Indeed, we find many intersection points of lines of different constant phase in the phase maps of $\mathbf{E}^T$ (Fig. 4.3b, e, and h), which we mark with symbols. We also mark these positions of undefined θ in the associated amplitude maps. We ensure that these points lie on positions of zero amplitude by plotting

$$f(r) \quad = \quad \log\left|A^{in}(r) - A^s(r)\right| + \log\left|\mathrm{mod}\left[\theta^{in}(r) - \theta^s(r), 2\pi\right] - \pi\right|, \qquad (4.1)$$

in Fig. 4.3c, f and i, and looking for points where $f(r) = 0$. When $f(r) = 0$, the amplitudes of the incident and scattered waves are equal (first term in (Eq. 4.1)) and their phases are opposite (second term). That is, these points are indeed the phase singularities in the vector components of $\mathbf{E}^T$. It is interesting to note that the distributions of these singularities can greatly differ between components. In particular, the singularities in E_y^T are located much closer to the hole than those of E_x^T and E_z^T. This difference is perhaps not unexpected, as the amplitude of E_y^{in} is smaller than that of the other two components, and hence the positions where the incident and scattered fields are equal occur at smaller r's. Phase singularities are known to carry a topological charge, s, which denotes the number of times the phase of the electric field changes by 2π when traversing a loop around the singularity in the counter-clockwise direction. The singularities that we observe all carry a topological charge $s = \pm 1$, where s is the same for all intensities within each quadrant of our maps, as we show in Fig. 4.2a, c, and e. For example, for E_y^T (Fig. 4.3d and e), $s = +1$ in the upper left and lower right quadrants, and $s = -1$ in the lower left and upper

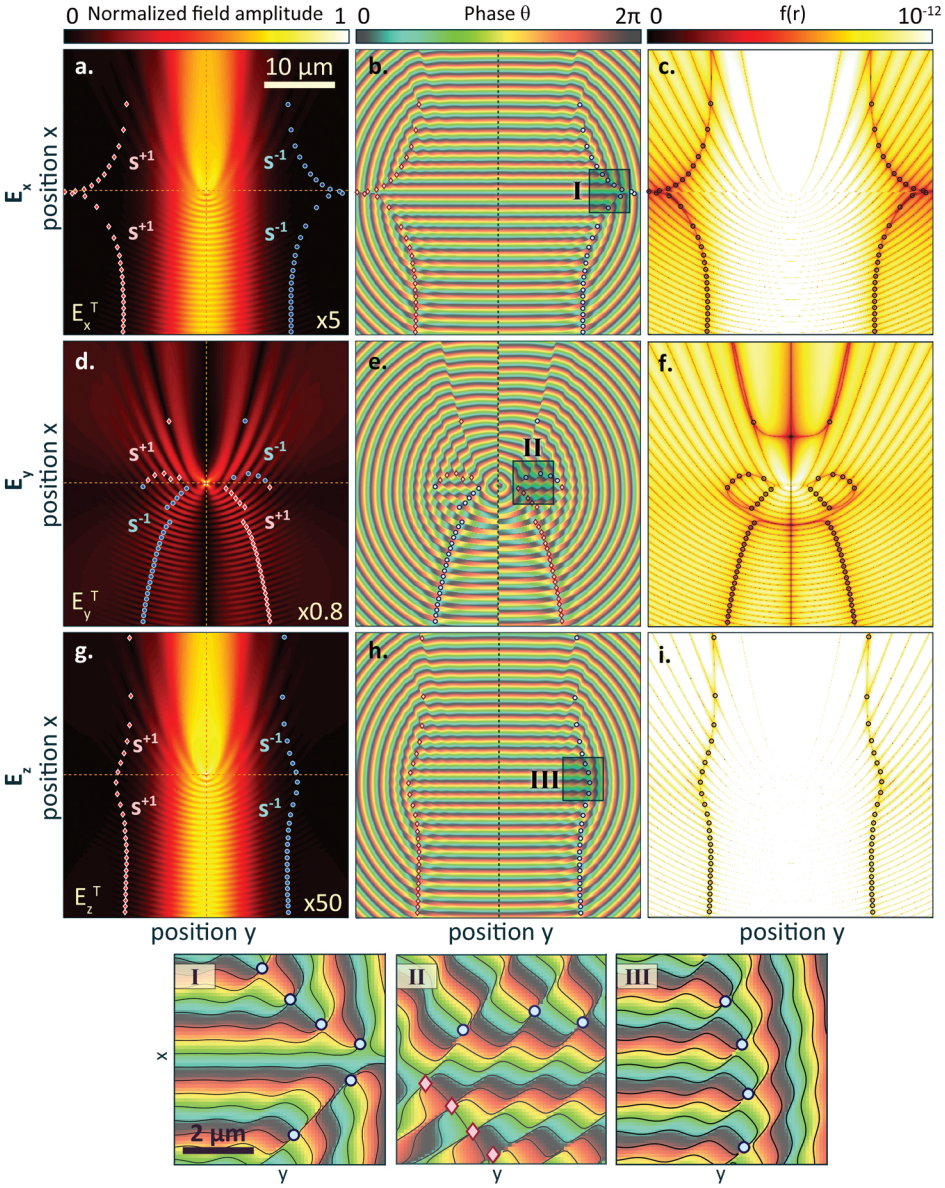

Figure 4.3: Electric field distributions that result when a 5 μm SPP beam scatters from a 800 nm wide hole. (a), (d), (g) The amplitude and (b), (e), (h) phase maps of $\mathbf{E}^T$ for the plasmonic scattering event, with the $s = 1\,(-1)$ phase singularities marked in solid red (blue) symbols. The relative amplitude of the different field components is shown in the bottom right of (a), (d), and (g). (c), (f), (i) maps of $f(r)(Eq.\ 4.1)$ associated with (a), (d), (g) and (b), (e), (h), with the locations of the phase singularities marked with solid symbols. The singularities are found where $f(r) = 0$, ensuring that they do occur when the amplitude of the associated field component (a), (d), (g) is also 0.

right quadrant. That is, for every singularity with a positive topological charge there is one with a negative charge, such that the total topological charge of the plasmonic field is zero for every field component.

4.3 Polarization singularities

In addition to phase singularities, another class of singularities exists that can occur in the light fields near a single hole: the polarization singularity. Within a plane, the electric field vector of the light, at any point, traces out an ellipse in time, as shown in Fig. 4.4a. Here, the polarization can be described by two variables. The first is the ratio between the short and long axis, u/v, which is a measure of the ellipticity, as given by Eq. 1.8. The second parameter that describes the polarization of light is the orientation angle of the ellipse α, which is given by Eq. 1.9 and ranges from $-1/2\pi$ to $+1/2\pi$.

Polarization singularities are found at positions where either the handedness or the orientation of the polarization ellipse is undefined. Here, we look for C-points and L-lines (*section 1.2*), in the plane of our sample (the xy plane), for which either the ellipse orientation α or the handedness of the polarization is undetermined. We present the amplitude of the in-plane electric field $A^T_{xy}(r) = \sqrt{\left[E^T_x(r)\right]^2 + \left[E^T_y(r)\right]^2}$ in Fig. 4.4b, $\varepsilon(r)$ in Fig. 4.4c, and $\alpha(r)$ in Fig. 4.4d, using the field components shown in Fig. 4.3. We find a large area in the maps where the polarization is (nearly) linearly polarized ($\varepsilon \approx 0$) in the direction of propagation ($\alpha = 0$), which originates from the Gaussian plasmon beam ($\mathbf{E}^{in}$). On both sides next to this region, we find highly structured patterns, where the ellipticity and ellipse orientation strongly vary in position. We can identify the singularities where the handedness of the light is undefined from the $\varepsilon(r)$ map, since these occur where the light is exactly linear ($\varepsilon = 0$). As these singularities, within a plane, occur in lines they are known as L-lines, and we mark them in Fig. 4.4c and d with blue lines. Note that L-lines always separate regions where the light has opposite handedness.

The second type of polarization singularity, where the orientation of the polarization ellipse is undefined, occurs within a plane at points. At such C-points light is circularly polarized. In analogy to phase singularities, we find C-points by locating intersections of contour lines of constant α (known as isogyres, and are shown by black curves in our figures) in Fig. 4.4d. Additionally, we ensure that $\varepsilon = \pm(1)$ at these locations. We show these C-points in Fig. 4.4 in symbols, where the color and shape correspond to the topological charge of the singularities (Eq. 1.12). In our figures, a topological charge of $+1/2$ is shown in red diamonds, and a charge of $-1/2$ in blue circles. In analogy to phase singularities, we determine the topological charge of the C-points from Fig. 4.4c by tracing out the number of times the orientation of the polarization ellipse rotates by 2π as a loop around the C-point is traversed in a counter-clockwise direction. From Fig. 4.4 it is clear that in our plasmonic system we observe two regions that contain singularities, which roughly form stripes along the direction of propagation on either side of the hole. Further, within each stripe,

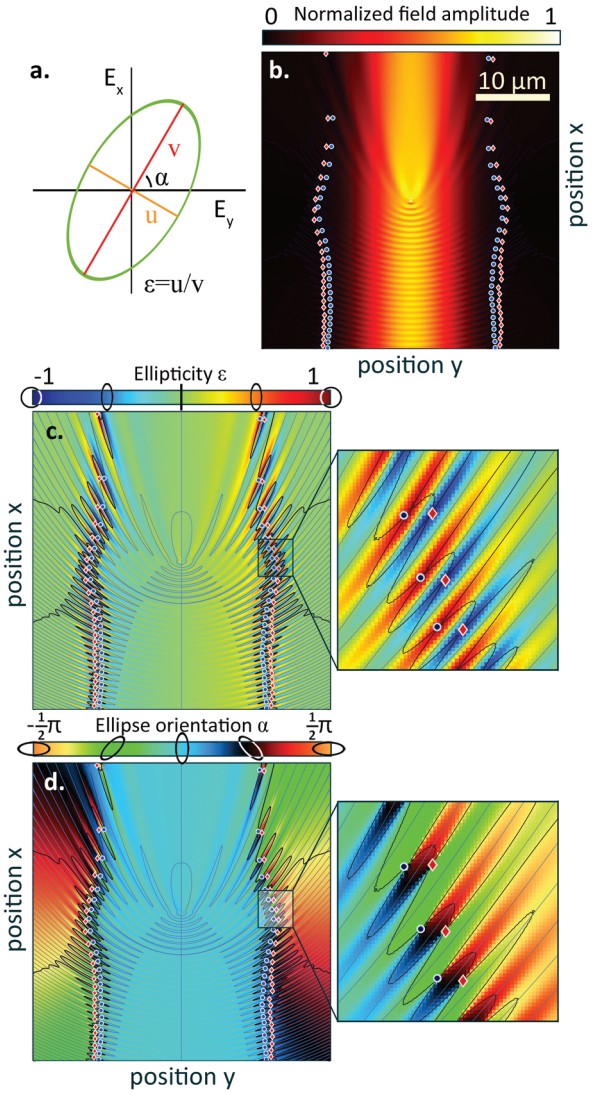

Figure 4.4: Polarization singularities in the plasmonic scattering event (a). Schematic of the polarization ellipse traced out by the electric field vector in the plane of the gold film (b). Amplitude map of the in-plane electric field of the scattering event. Polarization singularities with a topological charge of $1/2(-1/2)$ are marked in solid red diamonds (blue circles) (c). Ellipticity and (d) orientation maps of the electric field distribution for the scattering event. In (c), (d) L-lines ($\epsilon = 0$) are shown in light blue curves and isogyres (constant α) in black curves. The polarization singularities are again marked in solid symbols.

we find that the singularities come in pairs, where the inner singularity is negatively charged and the outer singularity is positively charged. As expected, an L-line runs in between each one of these singularity pairs (see Fig. 4.4c and d). Furthermore, the total topological charge of the system is zero.

When a 5 μm SPP beam scatters from an 800 nm wide hole, our calculations show that the C-points are all located well away from $y = 0$ (> 10 μm) where the intensity is highest. Consequently, the field amplitude at a C-point is typically $\approx (2-25)$ times weaker than the incident field amplitude, at the hole. There are two parameters in our model that can be varied, on which the position of the C-points is expected to depend: the diameter of the hole, d, and the FWHM of the Gaussian beam σ, as shown in Fig. 4.1. By changing the size of the Gaussian SPP beam we change the length over which the amplitude of $\mathbf{E}^{in}$ decreases away from its maximum at $y = 0$. Likewise, if we change the hole size, we change the efficiency with which it scatters light [52], and hence effectively change the magnitude of $\mathbf{E}^{s}$ relative to $\mathbf{E}^{in}$. That is, changing either, or both, of these parameters is expected to vary the positions where the interference of $\mathbf{E}^{s}$ and $\mathbf{E}^{in}$ creates C-points, and consequently the field amplitude at these singularities.

In Fig. 4.5 we show examples of $\mathbf{E}^{T}$ for several different hole and beam size combinations, in which we investigate whether the locations of the C-points change. In Fig. 4.5a, where we again show $\mathbf{E}^{T}$ for a 5 μm FWHM SPP beam scattering from an 800 nm hole, we highlight five singularities that we will follow. As can be observed in Fig. 4.5 when we increase d, while holding σ constant, the singularities all shift towards $y = 0$. This movement occurs because the larger hole scatters light more efficiently [52], and hence the region where the amplitude of $\mathbf{E}^{s}$ is comparable to that of $\mathbf{E}^{in}$ shifts closer to the hole. We observe a similar behavior, with the singularities shifting in towards $y = 0$, when we decrease σ while keeping d constant (Fig. 4.5c).

We vary σ and d in a systematic way to investigate the evolution of the field amplitude A at the positions of the C-points. Figures 4.5d and e depict the amplitude of the polarization singularities as a function of d and σ respectively. As shown in Fig. 4.5d, when the hole diameter is increased from 300 nm to 1200 nm, the relative electric field amplitude at the positions of the C-points increases, changing by almost three orders of magnitude for this range of hole sizes. We then fix $d = 1100$ nm, near where the electric field amplitude at the C-points is the strongest, and vary the beam diameter from 1 μm to 8 μm FWHM. We present the results in Fig. 4.5e, where we observe that increasing the beam diameter has almost no effect on the relative amplitude of the in-plane electric fields at the C-point position, even though the C-points are pushed away from the hole (compare Fig. 4.5c to Fig. 4.5a). Interestingly, we also observe that changing the beam diameter decreases the amplitude of the out-of-plane electric field component, A_z^T, relative to the in-plane amplitude, A_{xy}^T, at the position of the C-points (thick solid lines in Fig. 4.5e), in this case by almost two orders of magnitude over the range of beam sizes that we study. This suggests that it is possible to tune both the absolute amount of in-plane electric field amplitude that is present at the C-point, as well as the ratio of in-plane to out-of-plane amplitude. Since changing the hole size has a larger effect on the amplitude at the singularity

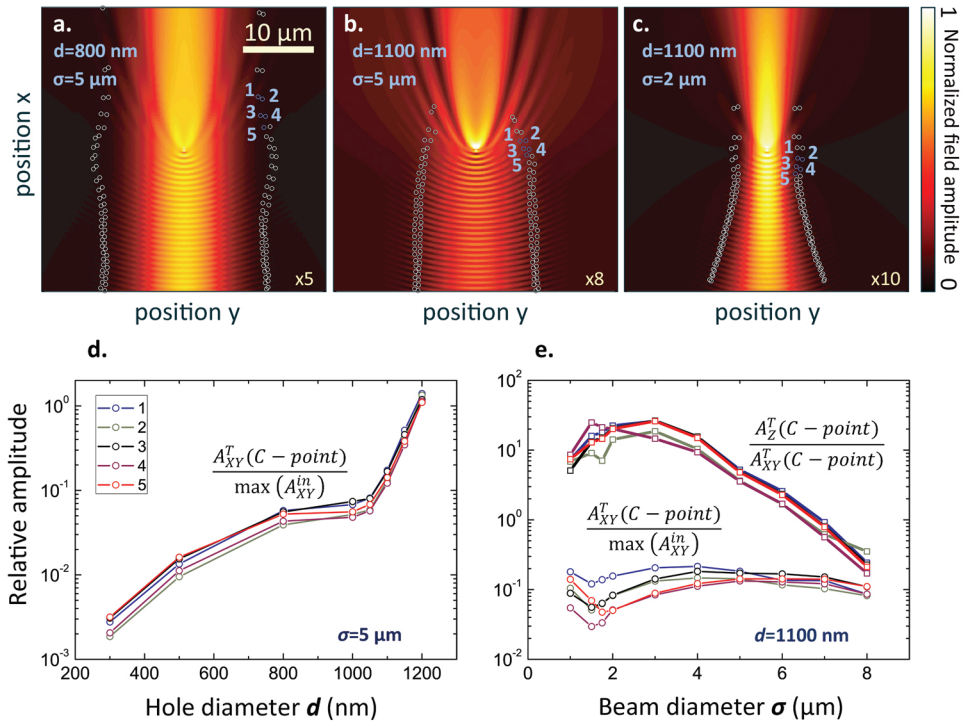

Figure 4.5: In-plane electric field amplitude maps for (a) a 5 μm SPP beam scattering from an 800 nm hole, (b) a 5 μm SPP beam scattering from an 1100 nm hole, and (c) 2 μm SPP beam scattering from an 800 nm hole. The locations of C-points in these maps are shown with white open circles, with five C-points shown in blue open circles and numbered, to help the reader observe how their positions depend on d and σ. The field amplitudes at the positions of the five C-points marked in (a), (b), and (c), normalized to the maximum of the incident in-plane field amplitude, as a function of (d) hole diameter and (e) beam diameter. The thick lines in (d) also show the ratio of the in-plane to out-of-plane electric field amplitudes at the location of the C-points.

location than changing the beam diameter, it is likely that the interplay between the two parameters will allow for the design of systems with large in-plane electric field amplitudes at the C-point locations with concurrent small out-of-plane amplitudes. Such a situation might be desirable, since it is in the in-plane electric field amplitude that we look for the C-points.

4.4 Near-field measurements

Having demonstrated the existence and control of C-points with theoretical simulations of plasmonic scattering events, we now hunt for their existence in experimental near-field data. We look for these singularities in data taken from [51], where SPPs were launched towards a single subwavelength hole of 875 nm perforated in a 200 nm thick gold film on a glass substrate. The plasmonic scattering event was imaged with a home-built near-field scanning optical microscope, using a heterodyne detection scheme which allows us to measure both the amplitude and phase of the in-plane field components [66]. The field maps are measured at a height of 20 nm above the sample.

In Fig. 4.6 we show a $A_{xy}(r)$, b $\varepsilon(r)$, and c $\alpha(r)$, which we extracted from the near-field measurements. The measured in-plane field amplitude (Fig. 4.6a) is qualitatively very similar to the calculated in-plane field amplitude (Fig. 4.4a). In both the experiments and simulations we observe a strong Gaussian beam overlaid with parabolic interference fringes. There are, however, some differences between the measured and simulated field maps, which preclude a good quantitative agreement. Most importantly, in the measurements the hole is not located at the center of the beam but, as can be seen in Fig. 4.6a, can be found a little to the left. This minor, relative movement of the hole with respect to the beam, results in both a change to the relative phases of the electric and magnetic dipoles that describe the plasmonic scattering event, and a significant shift to the interference fringes. It is therefore reasonable to expect that the positions where $\mathbf{E}^s$ and $\mathbf{E}^{in}$ combine to create C-points might also change. Second, the measurements contain some unwanted signals, and noise, which are not included in the simulations. Most obviously, in the measurements we see non-parabolic interference fringes, for example diagonal fringes to the right of the beam or horizontal fringes along the incident Gaussian SPPs. We attribute these fringes mainly to reflections that occur outside of the scan area, leading to additional surface waves. Yet, despite these discrepancies between our measurements and the calculations, we do see that important features in the calculated fields were reproduced in the measurements.

We search for the polarization singularities in the map of $\alpha(r)$ where we find multiple C-points where isogyres intersect. As was the case in the calculations, the C-points observed in our measurements are distributed in columns along the propagation direction, both to the left and right of the incident beam. Unlike the theory, however, we observe many more rows of singularities, which we attribute to the presence of additional (surface) waves. Such additional waves can arise from extra reflections, as noted above, or due to imperfections during the excitation of the original SPP beam.

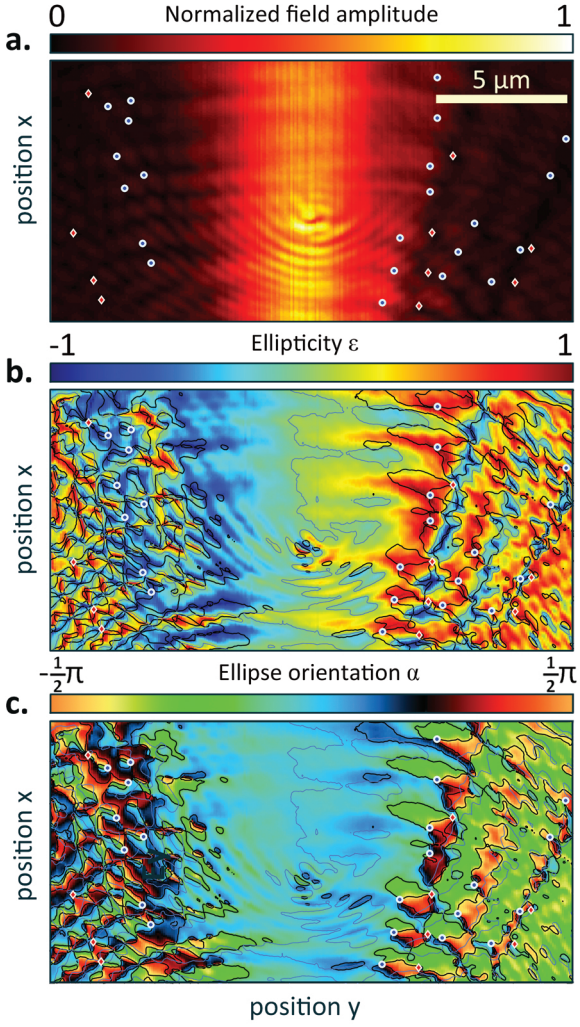

Figure 4.6: Near-field scanning optical microscopy measurements of the scattering of SPPs from an 875 *nm* hole. Maps of (a) the in-plane electric field amplitude, (b) ellipticity, and (c) ellipse orientation related to this scattering event. In all maps we mark C-points with symbols, using blue circles (red diamonds) for those with a topological charge of $-1/2$ ($1/2$). In (b) and (c), L-lines are shown in thin light blue curves and isogyres in thick black curves.

In fact, the topological charges of all C-points, other than those in the innermost row, seem randomly distributed between $s = \pm 1/2$. This random distribution of topological charge hints that these spurious singularities do, indeed, arise from noise and imperfections in the experiment. In contrast, all C-points in the innermost row, where the field amplitude is highest as is the signal-to-noise ratio, carry a topological charge of $s = -1/2$, in excellent agreement with the theory.

4.5 Conclusions

In conclusion, we find phase and polarization singularities in the electric field distributions that arise from the scattering of SPPs from single subwavelength holes in a gold film. These singularities are predicted by our theory and are also observed in near-field scanning optical microscopy measurements, although additional measurements are required for a quantitative comparison to be possible. We find that both the phase and polarization singularities are only found when both the incident and scattered waves are present and can interfere. Moreover, we show how by controlling the relative strengths of the incident and scattered waves, we can tune the position of the singularities, and even increase the field amplitude at the position of the C-points by three orders of magnitude. Because this control over the C-points is achievable by changing easily accessible parameters of the system, such as the hole size or incident beam diameter, we expect that our results will have importance to future on-chip applications requiring structured light fields.

Chapter 5

Creating and Controlling Polarization Singularities in Plasmonic Fields

In this chapter, we present the results of our search for the simplest plasmonic system that contains, and can be used to control, the smallest optical feature: an optical singularity. Specifically, we study the field around subwavelength holes in a metal film, obtained from numerical simulations, and search for polarization singularities. These can be C-points, at which the polarization is circular, or L-lines where the polarization is linear. We find that, depending on the polarization of the incident light, linear arrangements of two or three holes are sufficient to create a wealth of these singularities. Moreover, we find for the two-hole system that C-points are created in multiples of eight. This can be explained using symmetry arguments and conservation laws. We are able to determine where these singularities are created, their charge, and the topology of the field surrounding them. These results demonstrate the promise of this plasmonic platform as a tool for studying and controlling fundamental properties of light fields, and may be important to applications where control over these properties is required at the nanoscale.

This chapter is based on A. de Hoogh, L. Kuipers, T.D. Visser and N. Rotenberg, *Creating and Controlling Polarization Singularities in Plasmonic Fields*, Photonics **2**, 553 (2015).

5.1 Introduction

Structured light fields, which have long been studied at everyday length scales [14, 17,149–151], are increasingly being identified and studied at the nanoscale. That this transition occurs should not be too surprising, as we can control optical properties at the nanoscale, such as the speed [21, 152–154] and direction [155–157] in which light propagates, simply by engineering the structural geometry. What is surprising is how long it has taken for this transition to occur. After all, studies of fine structure in light fields, such as optical singularities, first appeared almost 70 years ago [30, 37, 158].

Perhaps investigations into the fine structure of nanoscale light fields were delayed because, initially, researchers were more interested in the macroscopic optical properties of nanopatterned materials, rather than their microscopic field structure. Studies of photonic crystal waveguides, where the geometry of a periodic array of holes in a thin semi-conductor layer determine the properties of the optical modes, are a perfect example of this phenomenon. Such waveguides were extensively studied for the way in which they guide light, generating considerable excitement for their ability to both highly confine light and to slow it down [21,152]. Yet, this very same nanopatterning, which controls the flow of light, also imprints fine structure onto their nanoscale light fields. It is only recently that researchers have begun looking into the structured light fields of photonic crystal waveguides [37,159], and, through an understanding of this structure, explaining the origins of the macroscopic behavior of the waveguide [160].

One exciting type of structure in light fields, which we will focus on in this work, is the optical singularity, and more specifically the polarization singularity [14, 151]. As extensively discussed in section 1.2, polarization singularities are amongst the smallest optical entities: infinitesimally small points in space where an aspect of the polarization of light (such as its handedness or orientation) is undefined, and whose surrounding light fields carry a topological charge. The recent studies of nanoscale optical singularities have been into the near fields of either highly structured dielectrics, such as photonic crystal waveguides [37, 144, 161], or the more simple plasmonic systems such as slits or holes in metal films [28, 162]. The latter, in part due to the underlying simplicity of the plasmonic systems, have illuminated key aspects of nanoscale singular optics and, in general, of light-matter interactions on the nanoscale. For example, these studies predict the nanoscale spatial evolution of optical singularities in complex light fields [28], and even offer a glimpse as to how they can be controlled and manipulated through nanoscale geometry [162]. These studies suggest that simple plasmonic systems can be used as a platform to study properties of optical singularities, at the nanoscale.

In this chapter, we set out to find the simplest plasmonic system where optical singularities can be created and controlled in a robust fashion. We use rigorous electromagnetic theory to numerically model the scattering of surface waves from multiple subwavelength holes in metal films. We find that scattering from 2 holes, which act as dipole sources of surface plasmon polaritons that predominantly radiate towards each other, is sufficient to create light field distributions that contain polarization singularities. If we rotate the polarization of the incident light such that

the scattering of the holes is predominantly in the direction orthogonal to the line containing the holes, then we find that 3 holes are required to generate polarization singularities. In other words, we show how using this simple plasmonic platform we can create and annihilate singularities simply by changing the hole spacing or the polarization of the excitation beam.

5.2 Polarization singularities in plasmonic fields

As thoroughly discussed in section 1.2, polarization singularities are, by definition, points where a property of the polarization of a light field is undefined. At the nanoscale, these singularities can often be found in highly structured fields that arise, for example, from the interference of the different Bloch harmonics that form the eigenmodes of a photonic crystal waveguide [37, 161], or the interference of incident and scattered surface plasmon polaritons (SPPs) from a nanoscatterer such as a subwavelength hole [162].

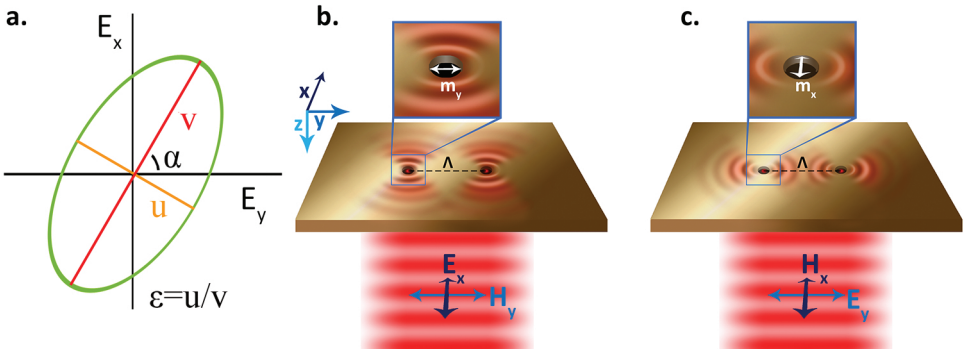

Figure 5.1: Plasmonic platform for the study of optical singularities. (a) The polarization ellipse. (b) Sketch of a plasmonic system that we envision to be used to study optical singularities on the nanoscale. Multiple holes, each separated by Λ are arranged along a line on an optically thick metallic film. Illumination from the bottom side, in this case at normal incidence with $\mathbf{H}$ oriented along y and $\mathbf{E}$ along x, excites dipoles in the holes (in this case, predominately m_y), which radiate SPPs on the top surface of the film. We look for singularities in the electric field distributions that result from the superposition of all the SPP waves. (c) Same system as in (b), but with the incident illumination rotated by 90 degrees, resulting in an initial response of the holes that is dominated by m_x. In this case, the holes will predominately launch SPPs in the $\hat{y}$ direction.

At any point in space, the polarization of a monochromatic light field on a plane (in this chapter we consider the plane of the sample, the xy-plane) of two field components (E_x and E_y) can be described by an ellipse (described in detail in section 1.2), as shown in Fig. 5.1a. This ellipse can be parameterized by the ellipticity ε (Eq. 1.8) and the orientation angle α (Eq. 1.9). The ellipticity, ε, measures the ratio between the short and long axes of the polarization ellipse, ranging from -1 to 1. When $\varepsilon = \pm 1$ the

electric field is circularly polarized, with the sign denoting the handedness, while $\varepsilon = 0$ corresponds to linear polarization. In the latter case, the handedness of the light field is undefined, giving rise to L-lines.

Likewise, the orientation of the long axis of the polarization ellipse, α, is measured from the y-axis towards the x-axis, and it ranges from $-\pi/2$ to $\pi/2$. If at a point in space, the orientation of the polarization ellipse α is undefined, we find a *C-point*. This type of singularity necessarily occurs at positions where the polarization is circular ($\varepsilon = \pm 1$). A C-point occurs when at that location the amplitude of the two components E_x and E_y are equal, meanwhile their phases are $1/2\pi$ out of phase. The light fields in the vicinity of C-points carry a topological charge (Eq. 1.12). The topological charge, which is here defined as the integer number of rotations that the director of the polarization ellipse undergoes as one traverses a closed path around the feature in a counter-clockwise manner. In this chapter, we will search for C-points with a topological charge of $\pm 1/2$, which come in three generic forms: the star, the monstar, and the lemon [142].

As noted above, C-points have been recently observed in a simple plasmonic system, consisting of a single subwavelength hole in a metallic film (chapter 4 [162]). In order to obtain structured light fields using a single hole, the excitation scheme is chosen such that there are still two sources of SPP waves. The complex electric field distribution that arises due to the interference of an incident SPP beam, and a wave of SPPs scattered from the hole, contains many C-points. The disadvantage of the excitation scheme, however, is that properties of the C-points, such as their positions, are sensitive to the properties of the incident beam. Slight changes in the size of the incident beam can, for example, cause the C-point positions to drastically change, making them hard to study.

Here, we propose to use the plasmonic system sketched out in Fig. 5.1b and c to largely decouple the properties of the electric field distribution, and hence of the C-points, from the incident light. As shown in this figure, our system consists of an optically thick gold film that is perforated by multiple subwavelength holes. We envision shining a weakly focused laser beam on the bottom of the sample to, a. ensure that only light radiated by the holes can be found on the top surface and, b. ensure that small changes to the incident beam parameters do not affect the resultant field distribution. We then search for C-points in the complex field distribution that results from the superposition of the different scattered SPPs. An advantage of our plasmonic system is that the nanoscale optical response of such a subwavelength hole is now well understood (section 1.4.3), and can be modeled as arising from in-plane magnetic dipoles (m_x, m_y) and an out-of-plane electric dipole (p_z), excited at the hole location [51, 52]. If these dipoles are known, then the electric field of the SPPs radiated by the hole can be written as Eq. 1.23.

In this chapter, we will consider a hole with radius $d = 400$ nm, for which the electric and magnetic polarizibility of the hole are $\alpha_E^{zz}/d^3 = -0.049 + i0.008$ and $\alpha_H^{\kappa\kappa}/d^3 = 0.130 + i0.167$ (where κ indicates the local in-plane orientation of the magnetic field) at $\lambda = 1550$ nm [52]. At this free-space wavelength, the SPP wavelength is $\lambda_{spp} = 1543$ nm. We note that the relative phase of these two polarizabilities is

largely independent of hole size, and hence we expect that small changes in hole size (and possibly shape) will mostly lead to a change in the amplitude of the induced dipoles, and hence the scattered field, and not to the shape of the scattered field.

The fields that are incident on the holes, $\mathbf{E}^{\text{in}}$ and $\mathbf{H}^{\text{in}}$, which excite the dipoles, can be due either to the initial free-space beam that is incident on the holes, or the scattered field from one hole that arrives at its neighbor. For the initial excitation we consider two cases, corresponding to orthogonal polarizations of the initial, free-space excitation beam. If this beam is polarized such that its magnetic field is oriented along the y axis (i.e. $\mathbf{H}^{\text{in}} = H_y\hat{y}$ and $\mathbf{E}^{\text{in}} = E_x\hat{x}$), as is shown in Fig. 5.1b, then the initial response of the hole will be dominated by the m_y dipole. If we place the holes on a horizontal line at $x = 0$ then the initial radiation of SPPs will predominately be in the $\hat{x}$ direction, and the holes will, in effect, not 'see each other'. Conversely, for initial excitation using $\mathbf{H}^{\text{in}} = H_x\hat{x}$ and $\mathbf{E}^{\text{in}} = E_y\hat{y}$, the response will be dominated by m_x, and the holes will predominantly radiate along the axis connecting both holes, as is shown in Fig. 5.1c. In this case, the interaction of the holes cannot be neglected, and in this work is accounted for by allowing the scattered field from any hole to act as an additional source term for its neighbors (see *Appendix D* for more details on the theoretical model and the interaction of the holes).

5.3 Results and Discussion

5.3.1 Two holes

We begin by considering the case shown in Fig. 5.1c, with two holes separated by $\Lambda = 3.2\ \mu m$ and the incident polarization chosen such that $\mathbf{H}^{\text{in}} = H_x\hat{x}$ and the holes interact with each other. The in-plane light field distribution of the SPPs, 20 nm above the gold surface, is presented in Fig. 5.2a where, in addition to the electric field amplitude, we also depict the ellipticity and orientation distributions. We observe in the field amplitude map that the scattering of SPPs is directional, with most of the light flowing in the $\pm\hat{y}$ direction, as expected for holes primarily characterized by m_x dipoles. Furthermore, in this amplitude map, we observe side lobes, whose angular position is determined by the interference of the SPPs radiated by the two holes. We note that, as shown in Eq. 1.23, the plasmonic field simply decays exponentially with z, and hence underline that only the amplitude, but not ε or α, of the field distributions shown in these maps depends on height. Near the hole, however, other fields, such as cylindrical waves [163] can be present, affecting the field distributions.

We hunt for C-points, in the plasmonic field radiated by the holes, by looking at the α map (Fig. 5.2a last pane). In this map, we follow isogyres - lines of constant α, shown with black curves - to their intersections, where α is necessarily undefined, and a C-point is found. For the scattering event shown in Fig. 5.2a we find 16 C-points that are roughly arranged in an ellipse, with the holes at the tip of the long axis. It is interesting that even such a simple system, with only 2 holes, can contain such a large number of singularities, and it is particularly useful that some C-points can be almost

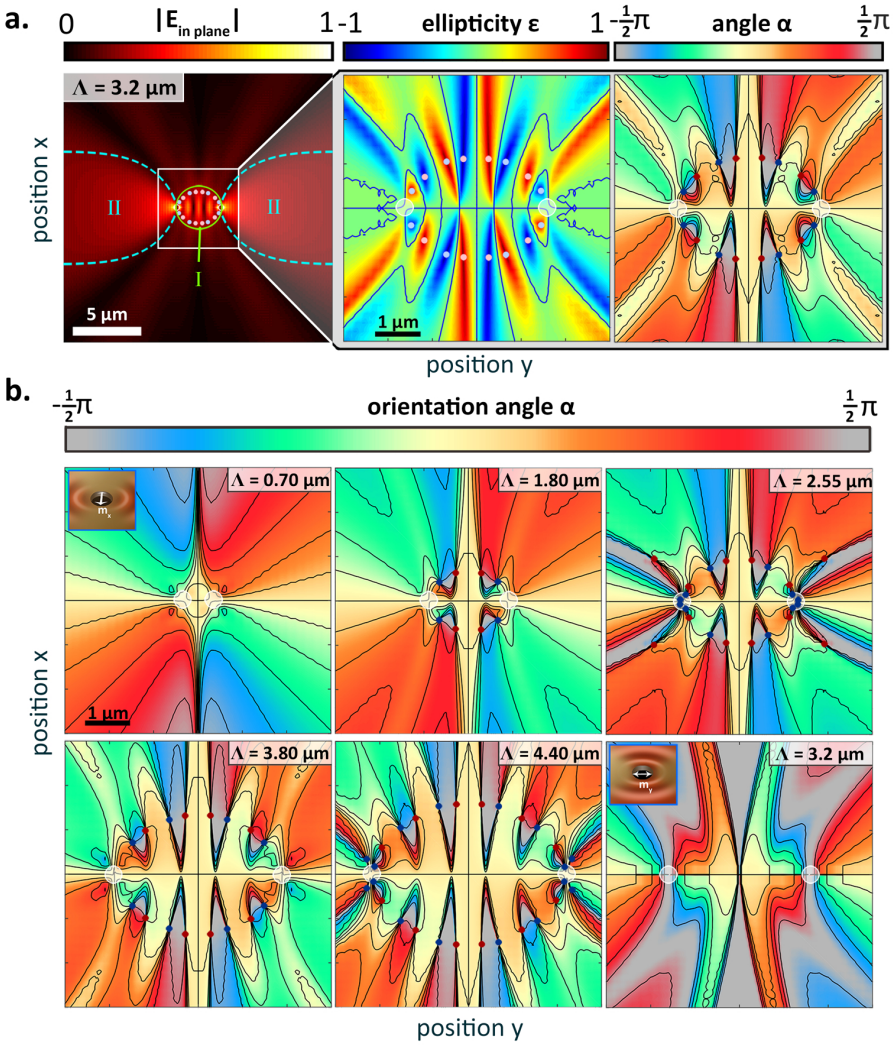

Figure 5.2: Light field maps for different plasmonic systems. (a) The in-plane electric field amplitude map, along with zoomed in maps of the ellipticity and orientation of the polarization ellipse, for two holes separated by 3.2 μm, with initial excitation H_x^{in}. In the field amplitude map, we draw two curves, (I) an ellipse and (II) two parabolas, along which we find polarization singularities. In this figure, we see C-points along I only, and we color code them according to their topological charge, with blue being $+1/2$ and red $-1/2$. We also present ε and α maps in a smaller region of the central area around the holes. For ε we mark the L-lines with solid curves, while for α we likewise show the isogyres. (b) α maps, with C-points marked in solid symbols as in (a), for different Λ, ranging from 0.70 μm, where we see no C-points, to 4.40 μm, where we see 28 C-points (24 on I and 4 on II) in our field of view. The last frame shows the case of $\Lambda = 3.2$ μm for H_y^{in} excitation.

2 μm away from the holes. Such relatively large separations are desirable since, near the hole aforementioned cylindrical waves might affect the field distributions.

We find the singularities in pairs, where each pair contains one singularity with a topological charge (Eq. 1.12) of $+1/2$ and one of $-1/2$, which we mark with blue and red symbols, respectively. Hence, the total topological charge of the light field is zero.

Having established that, with just 2 subwavelength holes, we can create electric field distributions that contain multiple C-points, we set out to test the tunability of our system. We begin by varying the separations of the holes, Λ, from 0.6 to 5.0 μm, and calculating the resulting electric field distributions. In Fig. 5.2b we show a selection of the resultant α maps, in order of increasing Λ. From these images, it is immediately clear that simply changing Λ can greatly affect the resultant light fields, and in particular we note that the complexity of the α maps increases with larger hole separations.

Moreover, we observe a dramatic change to the number of C-points that can be found in each map (Fig. 5.2b). For example, for $\Lambda = 0.6$ μm we do not find any C-points, while for $\Lambda = 1.8$ μm we find 8 C-points, and for $\Lambda = 3.6$ μm we find 16 C-points, and so on. This trend is summarized in Fig. 5.3, where it is clear that we find plateaus of Λ where the number of C-points present in the electric field distribution is a constant multiple of eight. Moreover, in all these cases, the C-points are found on

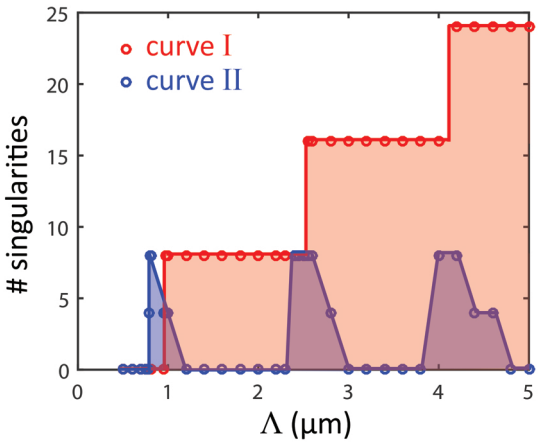

Figure 5.3: Number of C-points in our field of view, for the plasmonic system introduced in Fig. 5.2, as a function of Λ, showing clear plateaus of multiples of 8. Both the C-points found along curve I are shown (in red), as are those along curves II (in blue).

the ellipse described above, and which we sketch out in Fig. 5.2a and mark by curve I. The discrete step size (8 singularities) with which C-points appear can be understood as follows: our plasmonic system has two axes of symmetry ($x = 0$ and $y = 0$), which lead to a four-fold symmetry of the scattered SPP fields (as is evident from the

consideration of a single hole, in Eq. 1.23). Hence, we expect that if the singularities are created away from the symmetry axes, as is the case here, they will appear at 4 locations simultaneously. Moreover, at each position of creation, 2 singularities with opposite charge must be created, otherwise either the symmetry of our system or the conservation of charge will be violated. Hence, during a creation event, the symmetry of our system and conservation of charge dictate that a total of 8 new C-points appear. Interestingly, the width of each plateau is $\sim \lambda_{sp}$, perhaps because, for multiple holes, this would be the threshold for diffraction orders to appear.

In the α maps presented in Fig. 5.2b and in Fig. 5.3 we observe that something interesting occurs near transitions when the number of C-points increases. The transition is, in fact, not straight from n to $n+8$ C-points. Rather, at first when a transition occurs, several extra C-points appear, which then disappear when the new, $n+8$ plateau is reached. For example, when $\Lambda = 2.55\ \mu m$ (Fig. 5.2b, last image in the top row), we observe 20 C-points, and not the 16 of the plateau (e.g. $\Lambda = 3.8\ \mu m$, Fig. 5.2b, first image bottom row). Interestingly, these 'extra' C-points are always found outside of the main C-point ellipse, on curve II as marked in Fig. 5.2a, and first appear far away, at large y values. These extra C-points then move closer and closer to the holes, until after the creation event when, continuing on curve II, they again move out of our field of view. Interestingly, unlike the C-points found in curve I, the 'extra' C-points on curves II seem to violate the symmetry and conservation of charge argument. We envision that the missing C-points might lie outside of the field of view. The creation of C-points will be discussed in more detail, in section 5.3.3.

Finally, we recall that it is also possible to change the excitation beam, such that $\mathbf{H}^{\text{in}} = H_y\hat{y}$, corresponding to the last pane of Fig. 5.2b. In this case, the incident beam will predominantly excite the m_y dipole in the holes, and they will not interact. As expected for this incident polarization, SPPs are radiated by the holes predominantly in the $\pm\hat{x}$ directions. More importantly, in the α maps, an example of which is shown in the last image in the bottom row of Fig. 5.2b for $\Lambda = 3.2\ \mu m$, we find no C-points. This is true for the entire range of Λ's that we investigate (up to $\Lambda = 0.6$ to $5.0\ \mu m$). That is, 2 plasmonic holes that, initially, scatter SPPs perpendicularly to the line on which they lie are not sufficient to create electric field distributions that support C-points. Moreover, using a two hole plasmonic system it is therefore possible to create and annihilate C-points simply by rotating the polarization of the excitation beam.

5.3.2 Three holes

It is, of course, also possible to increase the number of holes in the gold film. We can preserve the symmetry of our system, even as we add holes, by placing the additional holes on the $x = 0$ line, along with the original 2 holes. The additional holes act as extra sources of SPPs, both initially or from secondary scattering events in the case of hole-hole interactions, resulting in more complex field distributions. We show examples of such fields (including the amplitude, ε and α), for the case of 3 holes separated by $\Lambda = 3.2\ \mu m$, for initial excitation using H_x^{in} in Fig. 5.4a and H_y^{in} in

Fig. 5.4b.

In these, we observe that the directionality of the scattering is still determined by the excitation - with SPPs being radiated primarily in the $\pm\hat{y}$ direction for H_x^{in} excitation, and vice versa - but that many more side lobes arise in comparison to the field profiles created by the two plasmonic holes (Fig. 5.2a).

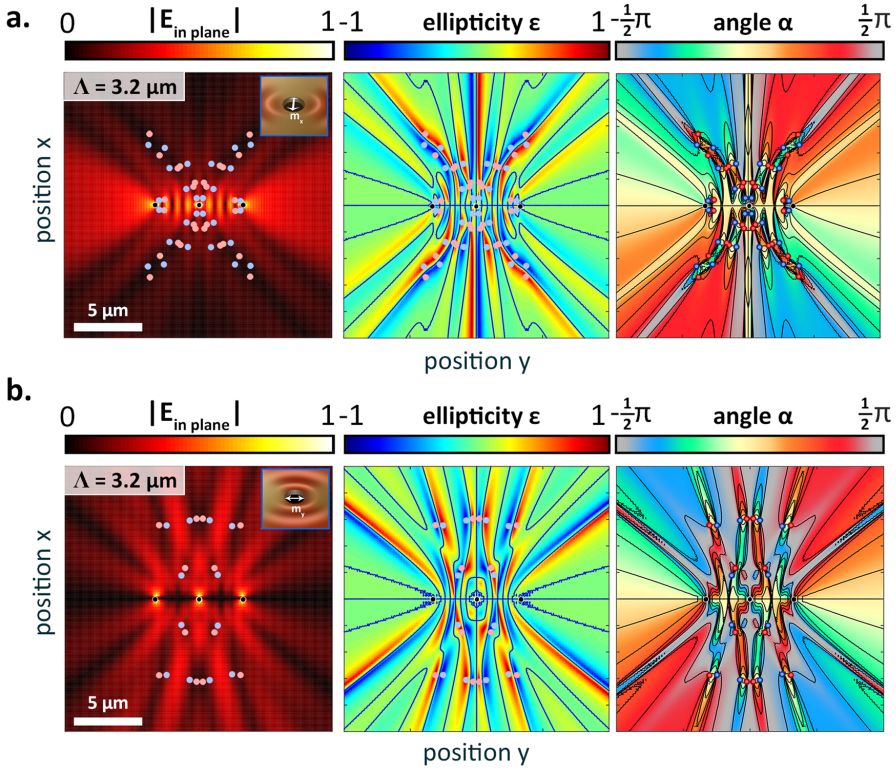

Figure 5.4: Light fields around 3 holes. Field amplitude, ε and α maps for 3 holes with 3.2 μm separations when the incident response of the holes is dominated by (a) m_x and (b) m_y dipoles. Both sets of maps clearly contain many C-points.

Given the increased complexity of the electric field distribution for the 3 hole systems, we could expect to find additional C-points therein, relative to the case when only 2 holes were present. In fact, investigating the field maps for both the 2 and 3 hole systems reveals that this is the case: for example, for the two hole system with $\Lambda = 3.2\ \mu m$ (Fig. 5.2a) we observed 16 C-points, while for the same Λ, when $\mathbf{H}^{\text{in}} = H_x\hat{x}$ (Fig. 5.4a), we now observe 56 C-points. Moreover, we see that when 3 holes are present, we find C-points at greater distances from the holes, particularly in the $\hat{x}$ direction. In essence, the SPPs scattered from the two outer holes can interfere

with the field from the middle hole, at relatively large distances directly above (or below, $|x| > 0$) it, to create circularly polarized light.

Interestingly and in contrast to the case when only 2 holes were present, with 3 holes we observe C-points even for $\mathbf{H}^{\text{in}} = H_y\hat{y}$ excitation, where the holes do not radiate towards each other. In Fig. 5.4b, for example, we find 24 C-points, which is comparable to the number of C-points found for only 2 holes under $\mathbf{H}^{\text{in}} = H_x\hat{x}$ excitation at this separation. It is clear that, regardless of the excitation field orientation, light fields containing polarization singularities can be created with relatively few such sources.

5.3.3 Creation and annihilation of C-points

The simple way in which our plasmonic system can be used to create light fields that contain polarization singularities, and more specifically, how nanoscale geometry controls these features, allows it to be used as a platform to study properties of these C-points. As a demonstration, we focus on the creation of C-points and study the evolution of the light fields as new singularities appear due to changes in geometry. Specifically, we consider the situation first shown in Figs. 5.2b and 5.3 where, near $\Lambda = 2.5\ \mu m$, new C-points appear.

When $\Lambda = 2.7\ \mu m$ (field amplitude and polarization maps in Fig. 5.5a), the transition from 8 to 16 C-points on curve I has been completed. At $\Lambda = 2.7\ \mu m$, we observe that the 16 C-points are arranged nicely along an elliptical curve, and are found in pairs of opposite charge where, in each pair, one C-point is found where $\varepsilon = 1$ and the other where $\varepsilon = -1$. As we learned, from Fig. 5.2, the new C-points appear near the holes, and so we now focus on a small area near the leftmost hole, as marked by the red rectangle in the α map (frame 3) of Fig. 5.5a, and study the evolution of the light fields, as the C-point pair shown in this volume appear (Fig. 5.5b). Due to the fastly changing polarizations as a function of position, extra close-ups are provided on the important areas.

At hole separations before the appearance of the new C-point pair, for example at $\Lambda = 2.52\ \mu m$ as shown in the first pane of Fig. 5.5b, we observe no points where α is undefined, in our region of interest. At $\Lambda = 2.53\ \mu m$ (second frame, Fig. 5.5b), however, something interesting occurs. This small change of separation, from 2.52 to $2.53\ \mu m$, is not enough to cause C-points to appear (at least, not within the resolution of our calculations), but it is enough to cause a point to appear in the α map, where the orientation is somewhat jumbled. As we see from the subsequent frames, it is from this point that the light fields that contain the C-points evolve.

In fact, a further small increase in separation, to $\Lambda = 2.55\ \mu m$ (third frame, Fig. 5.5b) is sufficient to make C-points clearly visible in the polarization maps. We mark these with blue and red circles, and note that they carry a topological charge of $+1/2$ and $-1/2$, respectively, ensuring that the total topological charge of the light field is conserved in this creation process. Interestingly, both C-points are formed in regions where $\varepsilon = -1$; that is, although the C-points carry opposite charge, the light fields in their vicinities have only one handedness. This situation remains even

for $\Lambda = 2.60\ \mu m$ (fourth frame, Fig. 5.5b), although as Λ increases, so too does the separation between the new C-points.

By $\Lambda = 2.70\ \mu m$ (last frame, Fig. 5.5b), the C-points are well separated and, interestingly, can now be found in regions of opposite handedness. The flip in handedness of the field in the area of the bottom C-point is interesting because, for this to occur it seems as though the C-point must cross an L-line; this view is supported by Fig. 5.5b, where up to separations of $2.60\ \mu m$ there is no L-line between the C-points, while it is clearly there when $\Lambda = 2.70\ \mu m$. Such a crossing of a C-point and an L-line is, in fact, not possible, since on the L-line the polarization of the light is linear, and hence has a well defined orientation α. Consequently, a C-point cannot be found on an L-line.

A closer look at the evolution of the C-points after their creation, in high resolution simulations allows us to determine how the handedness of the bottom C-point in Fig. 5.5b flips. Initially, in the region shown in the figure we observe two C-points on fields characterized by $\varepsilon = -1$. Outside our field of view, below the y axis, the situation is reversed, and two C-point on fields where $\varepsilon = 1$ were created. The handedness of the field underlying each singularity is, in fact, unchanged as the singularity moves due to a tuning of Λ. Rather, as Λ is increased the two C-points closest to the y axis the one above, in our field of view, and the one below, switch partner singularities. Once this switch occurs, at roughly $\Lambda = 2.64\ \mu m$, each singularity pair contains fields of both handedness, which are separated by an L-line. We emphasize that, during this rearrangement, no C-points are created or annihilated and the way that the C-points switch their partner singularity can be found in the next section.

Further, for the $\Lambda = 2.70\ \mu m$ frame in Fig. 5.5b, we trace the lines of constant α in the vicinity of the C-points to identify the type of singularity. We see that the top singularity is a *star* type C-point, identified by the 3-fold symmetric straight lines that radiate away from the singularity, while the bottom point is *monstar* C-point, where again 3 straight lines radiate away from the singularity, though without the 3-fold symmetry of the star. Interestingly, when further increasing Λ to, for example, $3.0\ \mu m$, we observe that the bottom C-point has transformed from a monstar to a *lemon* type C-point, further discussed in the next section. The evolution of the singularities, from the creation of a star-monstar pair to the subsequent transformation of the monstar to a lemon, confirms earlier predictions of this event [144].

5.3.4 Evolution of the C-point after creation

There are several interesting facets to the evolution of the C-points after their creation. Two of these facets are that one of the C-points appears to cross an L-line, and that this singularity also changes its class, from the monstar to the lemon type C-point. Although both of these events occur for the same C-point (the bottom one in Fig. 5b, which has a charge $+1/2$), they occur for different hole separations and hence we will discuss them separately.

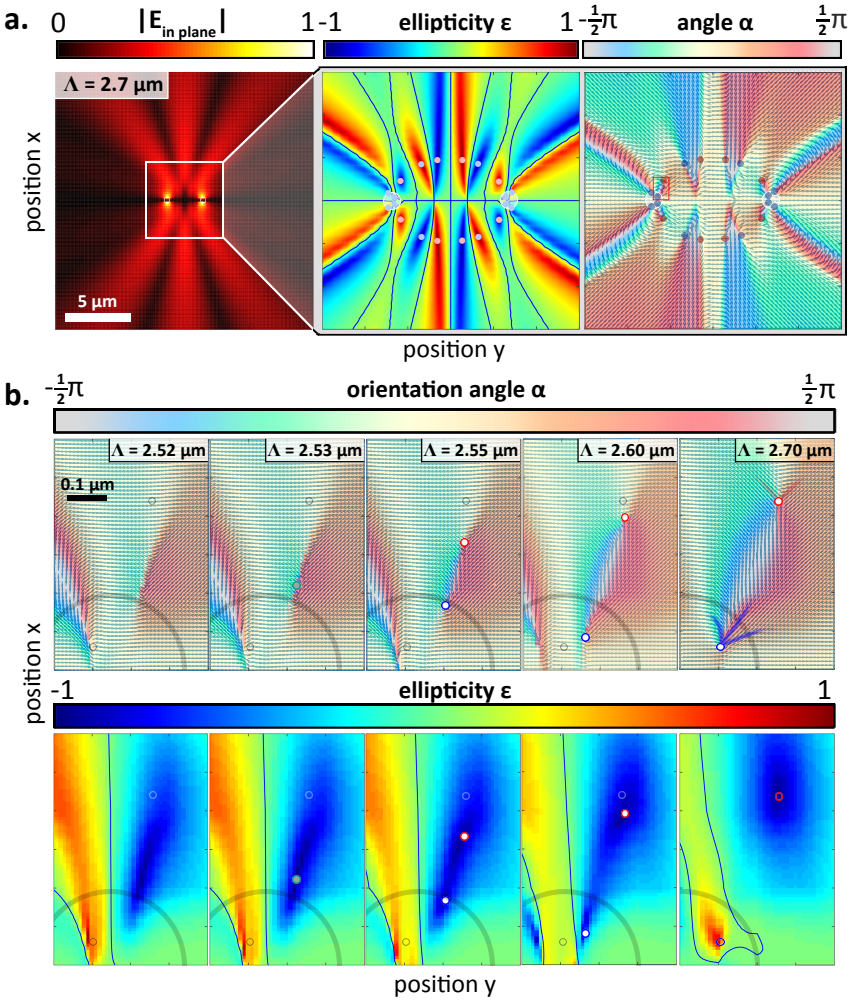

Figure 5.5: Evolution of the electric field leading to the creation of C-point pairs. (a) The in-plane electric field amplitude map, along with zoomed in maps of the ellipticity and orientation of the polarization ellipse, for two holes separated by 2.7 μm, with initial excitation H_x^{in}. In the ε and α maps we mark the locations of the C-points. For α, we also overlay the color map with vectors aligned along the direction of the long axis, indicated by arrows to also include relative phase information. Additionally, the region that contains the 2 C-points whose creation we investigate, is marked in the α map. (b) The spatial evolution of ε and α for $\Lambda = 2.52$ to 2.70 μm, in the region marked in (a). In all panes we show the outlines of the holes, which scans through the field of view with the change to Λ. In all panes, we also show the final positions of the 2 C-points (for $\Lambda = 2.7$ μm). For $\Lambda = 2.53$ μm, we mark the location where changes in the α map herald the formation of the C-points, which we subsequently also mark for larger separations. Finally, for $\Lambda = 2.70$, we also trace out the lines of constant α leading to the singularity, observing that the top C-point is *star* singularity, while the bottom C-point is of the *monstar* variety.

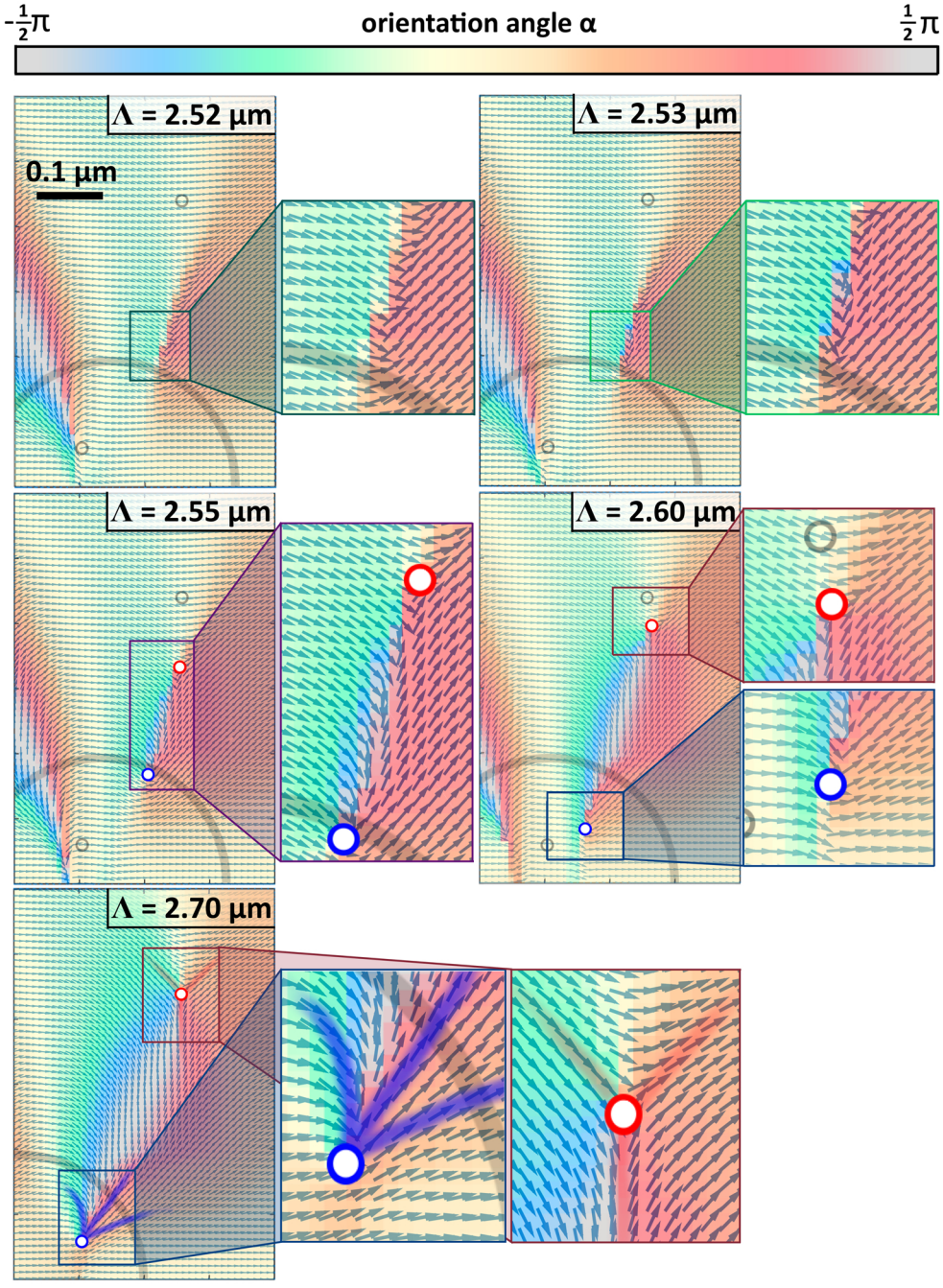
$-\frac{1}{2}\pi$
orientation angle α
$\frac{1}{2}\pi$
Λ = 2.52 µm
0.1 µm
Λ = 2.53 µm
Λ = 2.55 µm
Λ = 2.60 µm
Λ = 2.70 µm

Handedness

Firstly, although in Fig. 5.5 the C-point appears to cross an L-line for a Λ value somewhere between 2.60 and 2.70 μm, this is misleading. In fact, at every point in space and for every geometry that we consider the polarization of the light is well defined. That is, on an L-line singularity the polarization is linear and hence a C-point cannot exist on such a line. As discussed in the previous section, there is no crossing of the L-line, and what happens is that after the creation event, as Λ increase, the C-point pairs rearrange themselves so that each pair contains singularities with both handedness.

Initially, as shown in Fig. 5.5 at each point where a pair of C-points is created both have the same handedness. In the zoomed in region that we considered in Fig. 5.5, both C-points were located in fields with $\varepsilon = -1$ (see, for example, $\Lambda = 2.60$ μm in Fig. 5.5). This situation, where each singularity pair has fields of only one handedness is shown again in Fig. 5.6, in the large ε and α maps at $\Lambda = 2.63$ μm. As can be seen in this figure, the singularity pairs separated by the y axis are on fields with opposite handedness. This arrangement is clear in the zoomed in region, which spans contains both positive and negative x values, and in which we see, at $\Lambda = 2.63$ μm, one singularity on $\varepsilon = -1$ fields (for $x > 0$) and one on $\varepsilon = 1$ fields (for $x < 0$). As expected, these singularities are separated by an L-line.

A slight change of Λ causes the position of the C-points to shift. At a hole separation of 2.64 μm, the two C-points in our region of interest can both be found at the same x position, and are very close to each other in y. In fact, as can be observed in the middle frame of Fig. 5.6, they are only separated by a few pixels. A further minor increase of Λ to 2.65 μm, further shifts the position of the C-points. In fact, by this hole separation, these two C-points complete their crossing and now the singularity characterized by $\varepsilon = -1$ is found on the bottom half of the figure, while the one with $\varepsilon = 1$ is found in the top half. Peculiar is that during the C-point pair rearrangement, the four-fold symmetry of the system seems to be violated. So far we have not found a clear explanation for this. Interestingly, a change of hole separation of only 20 nm has caused an exchange of 2 C-points and a formation of new pairs, such that the new pairs contain fields of both handedness. Further increases in Λ up to $\Lambda \approx 4.2$ result in the new pairs moving away from the holes, as is shown in Fig. 5.2, but do not result in more exchanges of singularities between the C-point pairs.

C-point type

Secondly, as mentioned previously, increasing Λ causes one of the C-points to change its type, morphing from a monstar to a lemon type singularity. This C-point is, in fact, the same one that we studied when considering the handedness change of the underlying fields, in the previous section. Here, we continue to examine the fields in the vicinity of this singularity, starting from the case when $\Lambda = 2.7$ μm. As we showed in the last frame of Fig. 5.5b, and again here in the first frame of Fig. 5.7, the bottom C-point is identifiable at this hole separation as a monstar type singularity by

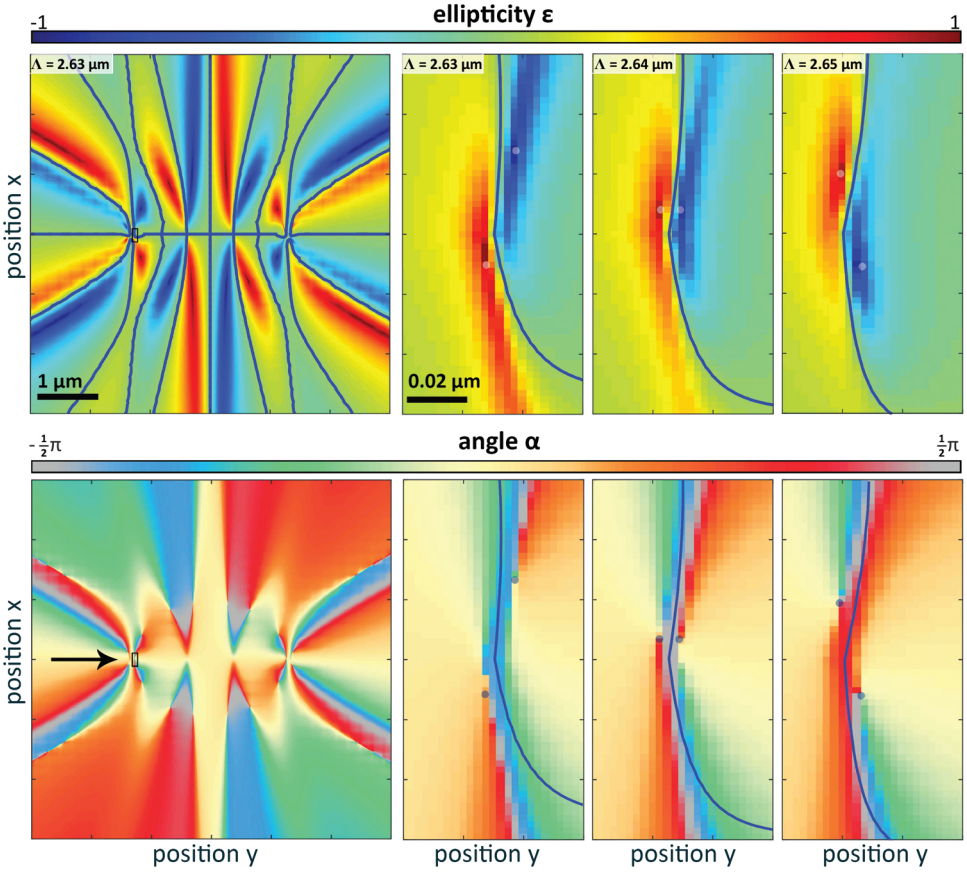

Figure 5.6: Calculated ε and α maps showing the rearrangement of the C-points leading to the final pairings of Fig. 5.5 . At a hole separation of $\Lambda = 2.63\ \mu m$, which is shown in the first frame, the newly created singularity pairs have only one handedness per pair. The zoomed in region, which is marked by a black rectangle (which in turn is indicated by the arrow) in the large image, contains one C-point from the top pair (on $\varepsilon = -1$ fields) and one from the bottom pair (on $\varepsilon = 1$ fields), separated by an L-line (blue curve). At $\Lambda = 2.64\ \mu m$ the C-points have moved so that they are located at the same x position, and are only slightly separated in y (by an L-line). At $\Lambda = 2.65\ \mu m$, the C-points have passed each other, and the C-point with $\varepsilon = 1$ fields is found $x > 0$, while the other, with $\varepsilon = 1$ is located at $x < 0$. Note the extremely small pixel size required to resolve this event.

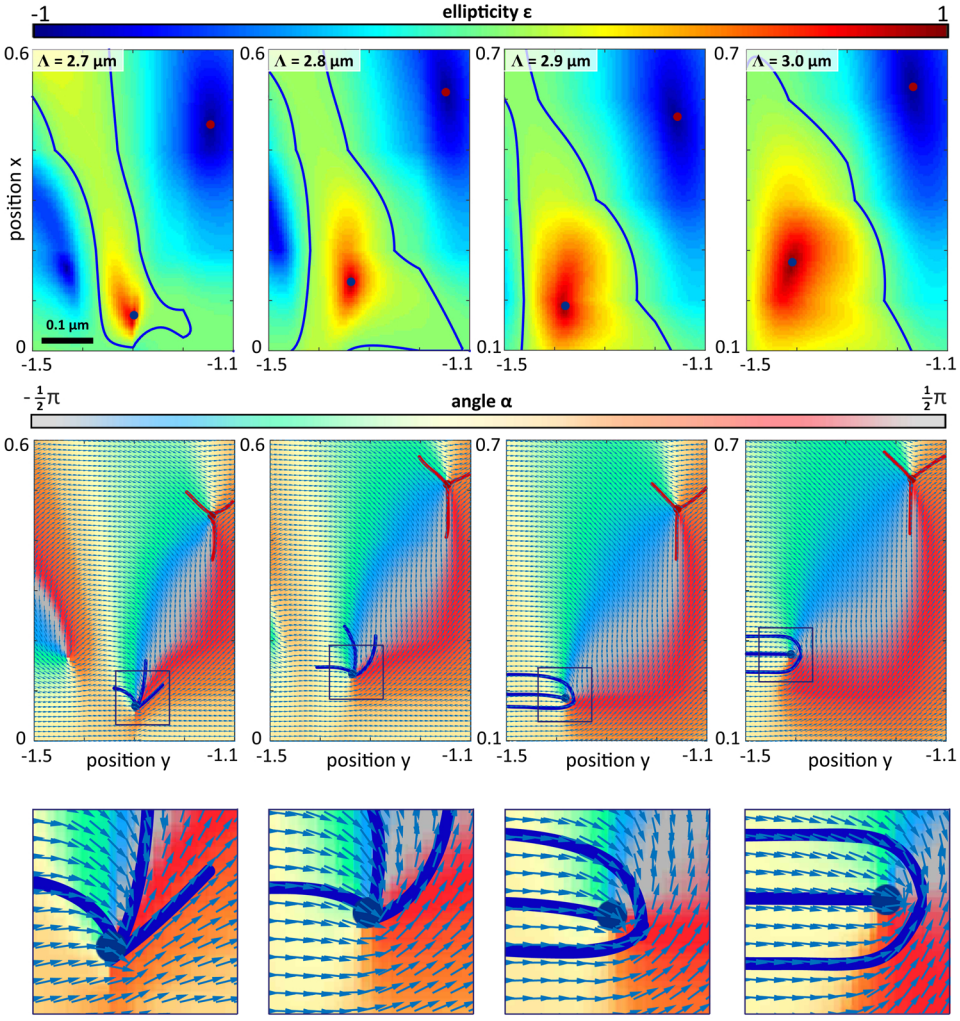

Figure 5.7: Calculated ε and α maps showing the metamorphosis of the bottom C-point from a monstar type singularity to a lemon type singularity. The C-points are marked in all maps by red (charge of $-1/2$) or blue (charge of $+1/2$) symbols. In the ε maps we also mark the L-lines with the solid blue curve. In the α maps we use the small arrows to show the orientation of the long axis of the polarization ellipse and the relative phase, at every point in space. Lines of constant ellipse orientation in the vicinity of the C-points, which we mark with solid curves, allow us to identify the type of singularity. The top (red) C-point is a star type singularity in all frames, while the bottom C-point morphs from a monstar singularity ($\Lambda = 2.7$ and 2.8 μm) to a lemon singularity ($\Lambda = 2.9$ and 3.0 μm). The field of view is the same as that of Fig. 5.5b.

the 3 straight lines that radiate away from it, all in the positive x direction (upwards in the figure).

In contrast, the uppermost C-point (red singularity) is a star type singularity, which is also characterized by 3 straight lines of polarization orientation that, in this case, show a three-fold symmetry. This upper most singularity remains a star singularity when Λ is changed.

In contrast to the upper singularity, whose type is constant, in Fig. 5.7 we see the C-point changes as Λ is increased. We can follow this change by considering the orientation of the polarization of the light near this C-point, which we trace with a solid curve to aid the reader. From these traces we can see that the C-point is initially, at $\Lambda = 2.7\ \mu m$ a monstar singularity, which is characterized by 3 straight lines of constant α that, in this case, are all found above (in the positive x direction) the singularity. Increasing Λ to $2.8\ \mu m$ causes these lines to rotate somewhat, but the singularity remains a monstar singularity.

Further increasing Λ to $2.9\ \mu m$ causes a rather more dramatic change to the local field distributions. Specifically, the left and right most lines of constant α no longer meet at the C-point, but now connect to each other behind (in the positive y direction) the singularity. Furthermore, the line of constant α that, for smaller values of Λ used to point in the positive x direction (upwards), has rotated by 90 degrees in a counter-clockwise direction, and now runs along the negative y direction (to the left). The overall pattern of these fields near the singularity shows that it is no longer a monstar type C-point, but is now a lemon. Further increasing Λ slightly changes the details of the field near the singularity but (for example for $\Lambda = 3.0\ \mu m$) it remains a lemon type singularity.

5.4 Conclusions and outlook

In this chapter, we present a new plasmonic platform that can be used to study polarization singularities in nanoscale light fields: an arrangement of multiple sub-wavelength holes on optically thick metal films. We show that depending on the polarization of the excitation beam, 2 or 3 holes are sufficient to create light fields with C-points. Moreover, we demonstrate that these light fields are intimately linked to the exact geometry of the system, and that small changes in the hole separations are enough to create or annihilate many C-points. In fact, in the case of a system of 2 plasmonic holes, we observe large plateaus of integer multiples of 8 C-points in the light fields as a function of the inter-hole separations, with sharp transitions where additional C-points occur only for a limited range of separation before disappearing again. Finally, we show that using this system we are able to study the evolution of the light field during one of these creation transitions. We focus on the transition from 16 to 24 C-points, for 2 holes, which occurs for hole separations of about $2.5\ \mu m$, where we can pinpoint the location where the creation occurs, as well as the type of C-points created, and the underlying helicities of the local light fields.

In conclusion, our results open up a new system where fundamental properties

of light fields can be studied at length scales compatible with near-field microscopy techniques [37, 65, 161, 164]. Moreover, many recent nanophotonic applications, from biosensing using chiral fields [165] to on-chip control of dipole emission [22, 166] for quantum optics, rely on highly structured local light fields near nanoscopic structures. In these applications, the fine structure of near fields is used to control the interaction of the nanophotonic structure with a nearby objects, be it a molecule or emitter. Our system, therefore, offers another approach to creating, and studying, such light fields, and may therefore be of interest as a route towards new technologies.

Appendix A

Fabrication of plasmonic nanowires and numerical calculations of their modes

As mentioned in section 1.4.4, plasmonic nanowires are interesting candidates for guidance of light at the nanoscale. Here, we provide the details of the fabrication of plasmonic nanowires and the numerical simulations to analyze their modes. The radial-like nature of the fields of this mode, makes it challenging to directly couple a Gaussian laser beam to the plasmonic mode supported by the nanowire, due to the low modal overlap. It has been demonstrated, that it is possible to efficiently couple free-space radiation to a 5 μm wide rectangular Au waveguide, first using a grating to excite glass-Au interface SPPs. By gradually narrowing down the width of the waveguide along a taper, the mode was subsequently adiabatically transformed to nanowire SPPs [90] [53].

Electron beam lithography

Gold nanowires were fabricated on a glass surface using electron-beam lithography. Next, Au is evaporated onto the sample through resistive heating, resulting in improved uniformity and smoothness of the layer. The detailed process of e-beam lithography is illustrated in fig. A.1a and consists of the following steps.

1. Substrate pre-cleaning

Plain UV-grade quartz glass substrates of 1x1 inch with a thickness of 1 mm are cleaned following a standard base piranha procedure. Samples are first sonicated in demineralized H_2O (dH_2O) in a Teflon basket. A beaker is filled with 5 parts water and 1 part NH_4OH and heated up to 75 degrees Celsius under constant magnetic

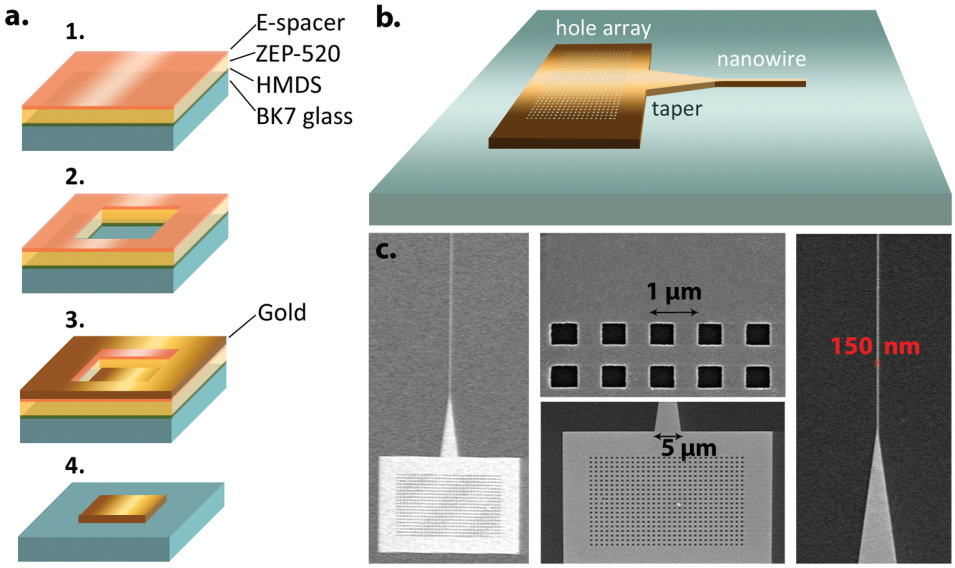

Figure A.1: Fabrication of a plasmonic nanowire. (a) The fabrication procedure using electron-beam lithography. After sample cleaning, a 1 mm thick BK7 glass substate is spincoated with a monolayer HMDS, a 180 nm thick layer ZEP-520 eventually covered with a thin e-spacer layer [1]. A 20 kV electron beam illuminates patterns into the three layers and the sample is developed [2] An argon etch is applied under vacuum conditions before gold is evaporated onto the sample with a uniform layer thickness of approximately 50 nm [3] During the lift-off process the resist with gold on top of it is washed away, only gold that was evaporated on the glass resists [4] (b) Schematic representation of the gold structure, consisting of a hole array with a periodicity optimized to couple $\lambda = 1500\ nm$ free-space light at the Au glass interface to the SPPs, a taper then gradually confines the SPPs from a 5 μm wide waveguide to the desired nanowire width of 10's to 100's of nm wide. (c) Scanning-electron microscopy images of a plasmonic nanowire with w=150 nm.

stirring. Addition of 1 part H_2O_2 and reheating to 75 degrees Celsius activates the base piranha and samples are cleaned for 15 minutes followed by two rinsing steps in a beaker with dH_2O and isopropanol respectively. The glass substrates are then dried with N_2.

2. E-beam lithography and development

For the lithography process the positive tone e-beam resist ZEP-520 is chosen for its high resolution and etch resistance (after exposure and development the illuminated areas are washed away while the unexposed resists remains). A monolayer of HMDS is first spun onto the piranha cleaned glass substrate for improvement of resist wetting and adhesion by the formation of a hydrophobic surface. The resist is diluted with anisole in a ratio of 5:2 and subsequently spun on top of the monolayer for 45 s at 2000 rpm. A uniform 170 nm thick polymer layer is obtained as measured with

profilometry. A layer of e-spacer is then spun to cover the ZEP-520 layer. E-spacer is a conductive polymer, allowing us to perform e-beam lithography without charging the sample. An area dose is used for the entire nanowire structure, with a dose of $50-60$ $\mu C/m^2$ and $60-72$ $\mu C/m^2$ for the hole array and the taper respectively. An optimal dose for the nanowire was established of between $50-600$ $\mu C/m^2$, dependent on the nanowire width. After exposure the sample is developed: first, the sample is rinsed for 60 seconds in a beaker filled with dH_20. After this the sample is dipped into another beaker containing dH_20 and blowed dry thoroughly with an N_2 gun. To ensure a completely dehydrated surface a new pair of tweezers is used to rinse the sample in N-amyl acetate for 1-2 minutes, followed by a 15 s rinse in an Methyl isobutyl ketone : Isopropylalcohol (MIBK:IPA) solution in ratio 9:1. Finally the sample is rinsed in IPA for another 15 seconds.

3. Gold evaporation

The sample is mounted in a vacuum chamber with a pressure of $6.5 \cdot 10^{-6}$ mbar. Prior to the gold evaporation, the sample is subjected to a 5 min Argon etch for a better adhesivity. Gold is then thermally evaporated over the complete sample with a deposition rate of 0.6 $\text{Å}s^{-1}$. With a profilometer the obtained thickness is determined to be 50 $nm \pm 5$ nm after the lift-off process.

4. Lift-off process

During a lift-off process the resist and gold left-overs are removed in Methylpyrrolidone (NMP) at 65 degrees C for approximately 4 hours, followed by a rinsing step in acetone and IPA respectively at room temperature. The sample is then dried with the N_2 gun. The resulting nanowires are characterized with a scanning electron microscope (SEM).

Figure A.1b shows the entire structure consisting of a nanowire, a waveguide taper and a hole array. We fabricated double structures, where each 50 μm long wire connects 2 tapers and hole arrays on each side. This fabrication scheme simplified the lift-off procedure. SEM images of a typical fabricated nanowire is presented in fig. A.1c.

Simulations of gold nanowires

For the numerical modeling of plasmonic nanowires in this thesis, we have used a two dimensional mode analysis using a finite element method implemented in COMSOL multiphysics. A box with sizes of 20×20 μm is chosen, divided into a glass and air region, all surrounded by perfectly matched layers (PML) as illustrated in fig. A.2. A cross-section of the rectangular gold nanowire is placed on the glass surface, in the middle of the box. The refractive index of air and glass were taken 1.0 and 1.5 respectively, the properties of gold were taken from literature [50]. A complicated mesh design is established to reach convergence over the effective mode index. At the edges of the nanowire, in fig. A.2 indicated with red lines, a maximum element size is taken of 0.1 nm, growing up to a maximum element size of 10 nm within the core of the nanowire (area 9 in fig. A.2). The surrounding air and glass regions (area 6 and 7 in fig. A.2) contain elements no larger than 2000 nm. Typically, to

reach convergence, the rule of thumb for the maximum element size is one fifth of the free-space wavelength. In this thesis, the largest free-space wavelength used in these simulations is 1550 nm. Due to a very fine mesh design at the edges of the nanowire, and a gradual increase of the element size away from the nanowire, the model converges despite a maximum element size larger than the rule of thumb. This design gives a high resolution in the area of interest, where the fields are highest. The electric and magnetic fields are normalized by the total energy in the system.

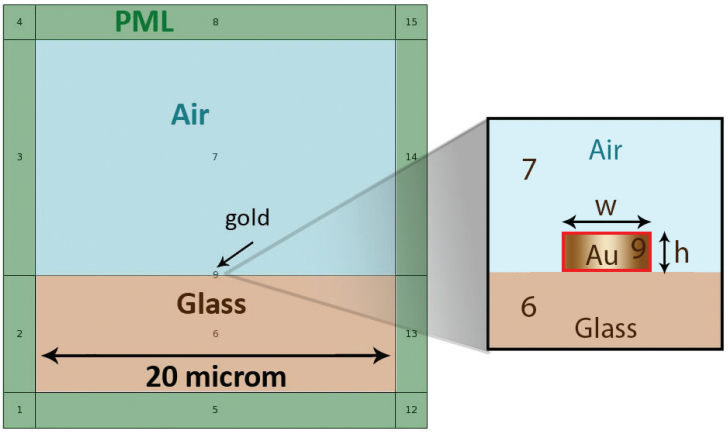

Figure A.2: Geometry of the simulation box (left) and the nanowire (close-up right). The width of the nanowire w is varied, whereas the height h is kept constant at 50 nm. The numbers indicate different simulation areas in the box. Each area is defined with material properties air, glass or Au, where the latter is taken from literature [50].

Appendix B

Scattering of SPPs guided on plasmonic nanowires

In *Chapter 2* we mentioned that the fundamental SPPs cannot be used as a reference to the harmonic intensities. In this appendix we provide the results which explain why the quantitative analysis of the scattered IR SPPs is not feasible and we discuss potential alternative strategies to use a reference to the harmonic intensities. Figure B.1a shows a IR camera image of a typical structure, taken by the diffuse illumination of the sample with a 1500 nm LED. The outlines of the hole array, taper and nanowire are marked by red lines to guide the eye. Next, a 170 nm wide NW is excited by illumination of a hole array with p-polarized light ($\lambda_\omega = 1550\ nm$) which excites SPPs in the nanowire. In Fig. B.1b IR images are presented in which the hole array is illuminated with a low (left) and high (right) incident laser power. The illumination spot on the hole array is bright (spot size FWHM $\approx 3\ \mu m$), even for a low incident power and no light is observed scattering from the nanowire. The tail from the incident Gaussian beam is sufficient to mask the scattering from the NW.

SPPs(ω) are expected to scatter from surface roughness without a clear preferential polarization. Hence, cross-polarized detection allows us to image the scattering of the fundamental SPPs from the NWs by effectively suppressing the background due to the illumination spot by at least two orders of magnitude. In Fig. B.1c an image is shown of the entire structure when the incident illumination I_{in} is p-polarized light, and the scattered signal I_{out} is detected with a perpendicular polarization. The insets show a close-up of the IR signal of the first $\approx 20\ \mu m$ of the NW for p-polarized and s-polarized illumination. In both cases the detected light I_{out} is cross-polarized to the illumination I_{in}, as indicated by the red arrows. With cross polarization we demonstrate that when we excite SPPs by illumination with p-polarized light (top panel) we observe a small fraction of light scattering from the nanowire. Contrary,

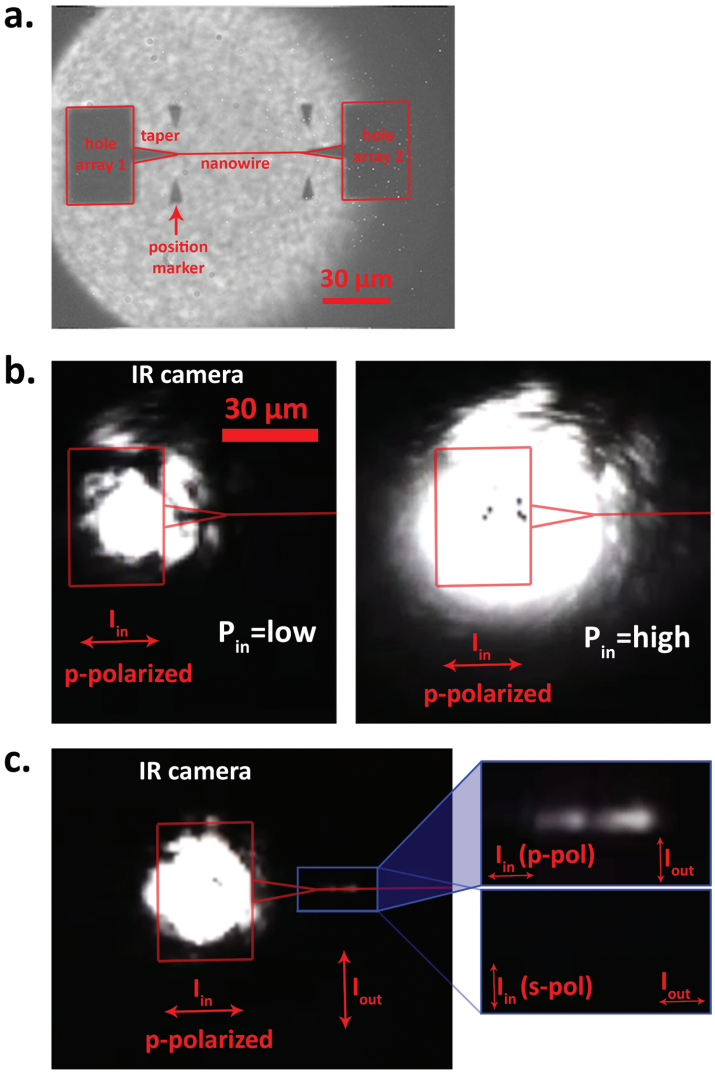

Figure B.1: Imaging fundamental SPPs scattering from a 170 nm wide NW. (a) Camera image of the hole array, taper and NW with red outlines of these elements to guide the eye. (b) IR signal from the hole array and NW using p-polarized light with a low (left) and high (right) laser power. (c) Cross-polarized IR signal from the hole array and NW using p-polarized and s-polarized incident illumination. We detect light I_{out} with a polarization that is perpendicular to the incident light. Thus we filter out most of the illumination spot I_{in}. In the insets we show close ups of the wire, where only p-polarized light results in a measurable IR signal from the NW.

with s-polarized light no nanowire SPPs are excited and consequently no light is observed to scatter from the nanowire.

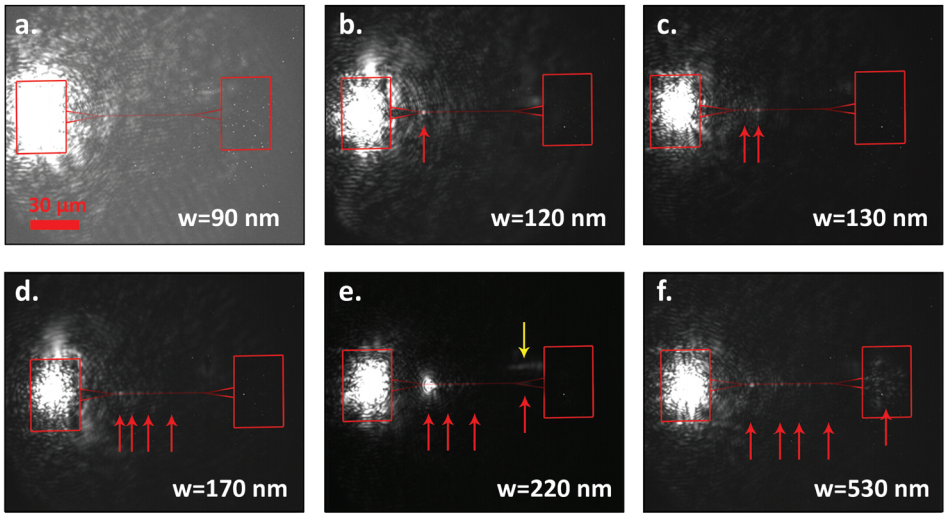

Figure B.2: IR light scattering from various nanowires including the excitation hole array, where the widths of the NW range from w=90 nm - 530 nm. Red outlines as shown in Fig B.1a are used to mark the position of the NW and launching structures. For NWs wider than 120 nm, light is observed scattering from the NW (indicated by red arrows). Wider wires show scattered IR signal over a longer range, ultimately allowing a small fraction to scatter out through the second hole array.

We image the scattering of fundamental SPPs from all NWs from which harmonic decay lengths were derived in chapter 2. In each case, the left hole array is illuminated with p-polarized light. A typical result for each NW width is shown in Fig. B.2, from which several observations can be made. First, wider NWs support SPPs with longer propagation lengths, in accordance with simulations and near-field measurements (presented in Fig. 2.3). This can be seen by bright features, indicated for each NW by red arrows that reach further on the NW for wider wires. The first clear observation of IR light from the end of the taper can be seen for $w = 120\ nm$, where a single clear hotspot is observed (red arrow in Fig. B.2b). For wider wires, the signal extends further along the NW, eventually reaching the far taper. For instance, for a $w = 220\ nm$ wide NW we observe a faint IR signal on the edge of the right taper, suggesting that a fraction of the SPPs propagates over the entire 50 μm long NW and then scatter from the edges of the taper. In the extreme case of $w = 530\ nm$, a small part of the SPPs are even adiabatically converted back along the entire right taper, to be scattered out by the second (right) hole array. Altogether, these images demonstrate that scattered fundamental SPPs can be detected by an

IR camera and that their propagation lengths depend on the NW width, as expected from simulations.

Second, we observe that the illumination spot dominates our IR images, even when we use cross-polarized detection. We observe diffraction circles that originate from the location of the focal spot on the hole array. These circles also cross the NW. Furthermore, stray light can be observed in several images that can even reach the far taper. This is most clearly visible for $w = 220\ nm$, indicated by a yellow arrow. We were not able to find the origin of this stray light. Hence, while we can use these images to observe the expected trend between propagation lengths of the fundamental SPPs and NW width, the presence of incident and stray light prevents us from using them for a more quantitative comparison with the harmonic maps presented in *Chapter 2*.

Several other strategies could potentially be used as a reference to the harmonic intensities. For instance, a logical step would be to perform linear measurements at the wavelengths of the second and third harmonics (i.e. the hole array will be illuminated with 775 nm and 517 nm respectively). The comparison of the intensity along the wire of the linear and nonlinear measurement, at the same wavelength, could provide useful information about the efficiency of harmonic generation. Due to short propagation lengths of SPPs at the visible wavelengths even in the adiabatic taper, the linear SPPs at 2ω and 3ω would already be so attenuated after propagation to the end of the taper, that no detectable signal would propagate along the nanowire.

Another strategy could be to use the third-harmonic signal as a reference for the second-harmonic signal. The propagation length of SPPs at 3ω are only $\approx$ 30 nm, (dependent on the nanowire width) and hence the third harmonic could, in principle, act as a local probe for the fundamental intensity when the cubic intensity relation is taken into account. However, at the safe powers, where we do not damage the nanowires irreversibly, the third-harmonic signal is very low, and process I for its generation typically overshadows process II and III, resulting in a finite number of very bright 3ω spots. As a result, no exponential decay can be fitted to the signal and hence, the 3ω signal cannot be used as a reliable local probe for the fundamental intensity.

Other methods from which we could get more information about the fundamental behavior on the nanowire exist, which exploit leaky modes. However, with the exception of a small range in nanowire width and for the fundamental frequency only, all involved modes are not leaky: so without scattering at imperfections they cannot radiate to the far field. Nevertheless, increasing the NA of the collection, e.g., through the use of an oil-immersion objective, would probably increase the collection efficiency. Such an increase would facilitate future experiments. Near-field experiments are, in principle, also feasible at the harmonic frequency, but they suffer greatly from low collection efficiencies.

Appendix C

Statistical analysis of the second-harmonic decay length

In *Chapter 2* we have determined decay lengths of the second-harmonic intensity from the camera images. The decay lengths from nominally identical nanowires were then averaged. The detailed statistical analysis is described in this appendix.

To extract the decay lengths of the SH signal for each NW, we process our images as follows. First, to obtain the SH signal for one position along the NW, we integrate the signal in the 2D images over 6 pixels across the nanowire width. Figure C.1 shows the spatial distributions of the SH signal for four different NWs with nominally the same dimensions (which is the same dataset as presented in fig. 2.3b in *Chapter 2*) on a linear scale (top) and a semi-log y scale (bottom). As discussed in the results of *Chapter 2* the distributions evaluated on a linear scale exhibit sharp and clear peaks. These peaks originate from generated harmonics at local hotspots. Conversely, evaluated on a semi-log scale (bottom frame of Fig. C.1) these peaks do not appear as dominant. However, as we discuss in *Chapter 2*, exponential decay associated with processes II and III (see Fig. 2.3b of *Chapter 2*) is more readily recognizable than on a linear scale.

For each structure we measured the SH yield using three or more different powers. This was done both to collect sufficient data, and to ensure that the structures were not physically damaged by the laser. For the statistical analysis, all curves from the measured powers for a certain structure are plotted in one graph. For example, in Fig. C.2 all measured power curves are plotted for the NW represented by the blue curve in Fig. C.1. Subsequently, a fit area is selected, marked by the vertical dashed gray lines, hereby limiting our analysis to regions where process II and III

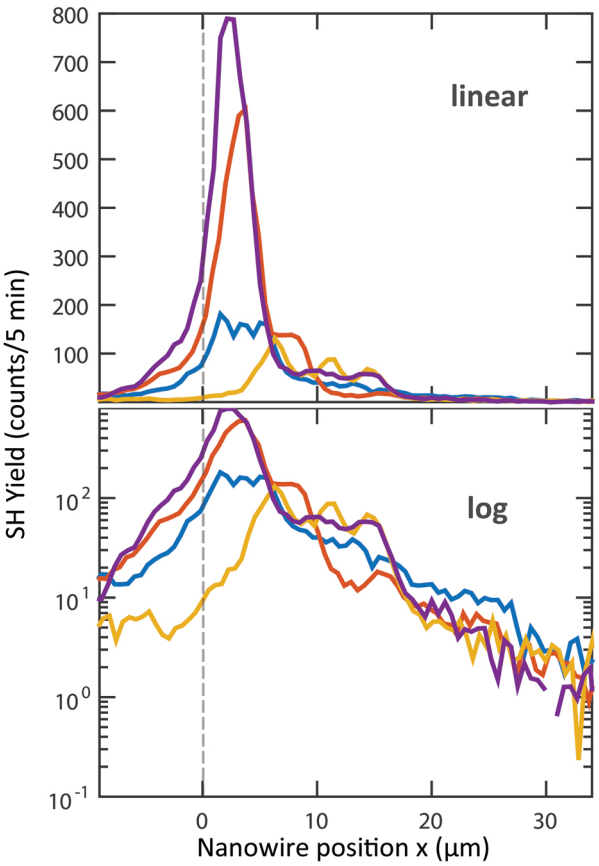

Figure C.1: Measured SH Yield for four 90 nm wide NWs. The NW begins at $x = 0\ \mu m$ The SH yield is shown on a linear scale (top graph) and a log y scale (bottom). The peaks in SH yield resulting from local plasmonic hotspots on imperfections become less visible on the log scale.

dominate. In this fit area, a single linear slope is fitted to the log of all power curves by minimizing the sum of squared residuals (SSR) for all curves simultaneously. As the SH yield scales with the square of the incident power, the offset of the curves is set free in this fitting process. This procedure results in a decay length and standard deviation of the fit for each NW. This standard deviation σ is determined by plotting the SSR as a function of the fit parameter (i.e. slope) and finding where the SSR intersects with the minimum of SSR, $min(SRR)$, following

$$\sigma = \frac{min(SSR)}{(n-m)}(n-m+1), \tag{C.1}$$

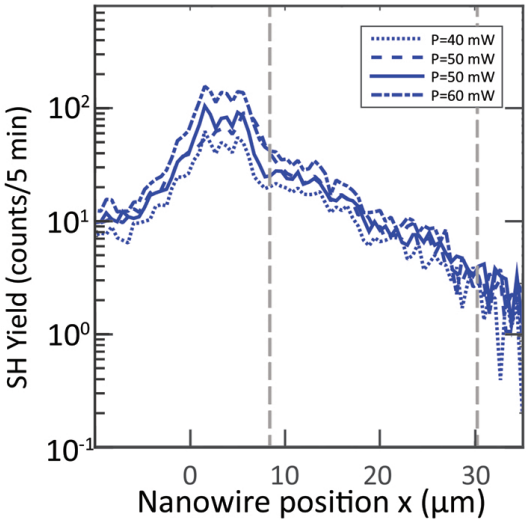

Figure C.2: SH yield of a 90 nm wide NW, using different powers on one single NW structure (blue curve in Fig. C.1). Four curves are shown of measurements using powers of 40, 50 and 60 mW of which 50 mW was measured twice to demonstrate the reliability and reproducibility of the SH distribution on this NW. Dashed lines indicate the boundaries of the region where the exponential decay is most prominent and where a linear fit is performed on the log of the SH yield.

with n the number of data points, and m the number of fit parameters.[1]

We repeat this procedure for N different wires with the same dimensions, which gives us N decay lengths $\ell_p(2\omega, j)$ and standard deviations $\sigma(j)$, where $j = 1, ..., N$. We then average these numbers for each NW dimension to obtain an average $\ell_{p,2\omega}$ and $error(2\omega)$, weighted by the inverse squared standard deviation of the individual fits for N wires $\sigma(j)^{-2}$ following

$$\ell_{p,2\omega} = \frac{\sum_{j=1}^{N} \ell_{p,2\omega}(j)/\sigma(j)^2}{\sum_{j=1}^{N} \frac{1}{\sigma(j)^2}}, and \tag{C.2}$$

$$error(2\omega) = \sqrt{\frac{\sum_{j=1}^{N} (\ell_{p,2\omega}(j) - \ell_{p,2\omega}^2)/\sigma(j)^2}{\sum_{j=1}^{N} \frac{1}{\sigma(j)^2}}}. \tag{C.3}$$

[1] $http://www.hjcb.nl/meten/GoedMeten.pdf$

Appendix D

Interaction of plasmonic holes

In *Chapter 5* we have studied the EM fields near multiple subwavelength holes in an optically thick gold film. The fields arise from illumination normal to the sample through the bottom, using two polarizations. Here, we investigate for both polarizations whether the SPPs generated at one hole can act as an additional source term for the neighboring hole. As in *Chapter 5*, here we consider the two cases, where the holes either (i) radiate SPPs primarily along the axis connecting both holes or (ii) where the SPPs are mainly radiated in a direction perpendicular to that axis. If the two holes are located on the $x = 0$ line (see Fig. 5.1 of *Chapter 5*) then case (i) corresponds to an initial excitation of the m_x dipole in the hole, while case (ii) corresponds to an excitation of the m_y dipole. If we take the initial excitation field to have an amplitude of 1 (that is, $Z_0 H_i = 1$, for $i = x, y$ and free-space impedance Z_0), then the field amplitudes at a second hole (normalized to the excitation field at the first hole) as a function of the displacement from the first hole, for both dipoles, are presented in Fig. D.1, for both dipoles.

In this work, we set a threshold of 0.1 in the amplitude on the interaction of the holes when this value is exceeded. That is, we consider two holes to interact if the amplitude of the scattered field from hole 1 that reaches hole 2 is equal to or larger than 0.1 times the amplitude of the excitation field at hole 2. From Fig. D.1 it is evident that in the case of an m_y dipole (part b) two holes would not interact unless they were to be placed much less than a micron from each other. Conversely, for the 0.1 interaction threshold, a hole whose response is dominated by an m_x dipole would interact with a second hole, even if they were placed many microns apart (Fig. D.1a).

In our calculations we allow the holes to interact by calculating the scattered field distribution from one hole and finding the different field components that arrive at

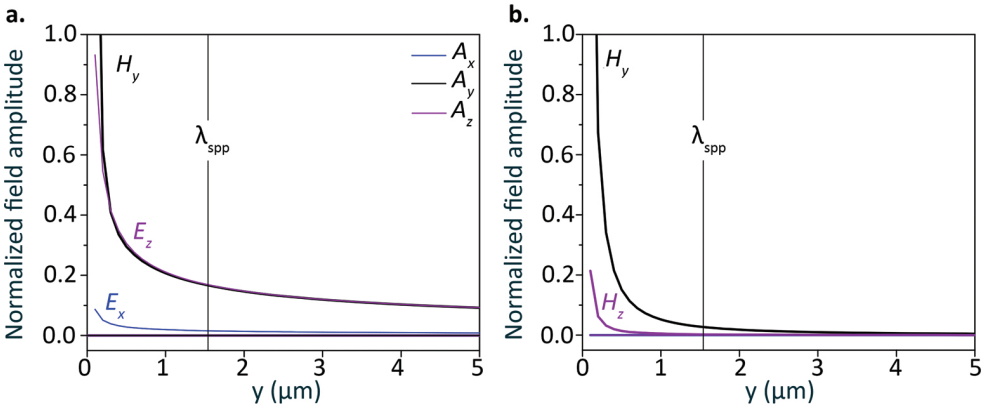

Figure D.1: Amplitude of the electromagnetic fields as a function of position from a hole (along the y-axis, as shown in fig. 5.1 of chapter 5) whose response is due to (a) an m_x dipole, and (b) an m_y dipole. Details on the numerical method can be found in section1.4.3 and chapter 5. All fields are normalized to the incident excitation field at the position of the hole, which has amplitude $Z_0 H = 1$. All nonzero field components are labeled, and the surface plasmon polariton wavelength is shown by the vertical black line.

the location of a second hole, as was done in Fig. D.1. If the amplitude of a field component at the secondary hole location is greater than our threshold (0.1 of the initial field amplitude at the secondary hole), then we let that component act as a secondary source (which creates new dipoles in the secondary hole, according to Eq. 1.22). This process is then iterated for these new dipoles and all other holes, until no more field components pass our threshold. We follow this procedure for all dipoles that characterize the hole, not just m_x or m_y as was done in Fig. D.1).

Neglecting the interaction of holes has the potential to greatly effect the scattered-field distributions. An example of the potential error caused by ignoring the hole-hole interaction is depicted in Fig. D.2. Although at first glance the distribution of the electric amplitude looks similar regardless of whether or not the holes are allowed to interact (top row), a closer look reveals large differences (bottom row). In fact, in certain locations deviations of upwards of 75% are caused by neglecting the hole interactions. Interestingly, we can find C-points in the field distributions regardless of whether or not the holes interact, showing that the presence of the singularities is mostly determined by the original sources (dipoles) induced in the holes, and not by any secondary scattering effects. Of course, details such as the exact location of the C-points are changed when the interaction is turned off or on.

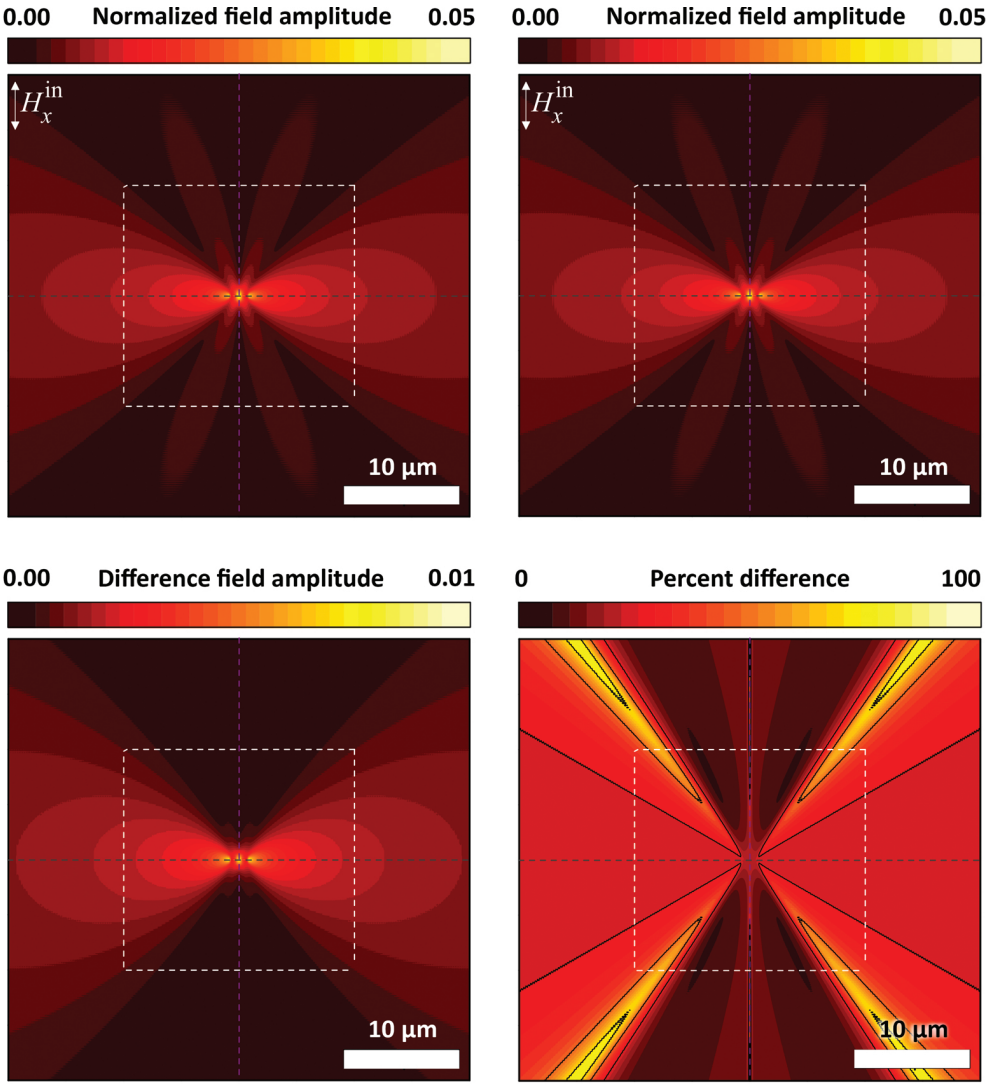

Figure D.2: Calculated scattered field amplitude of two 400 nm (radius) holes separated by 1.3 μm whose optical response is due to the m_x dipoles excited by the illumination beam. Both the cases when the holes are allowed to interact (top left) and when the interaction is turned off (top right) are shown. In the bottom row, the difference between these two case is shown, both in the same units as the top row (bottom left) and as a percent change (bottom right). In the final plot, contours are shown every 25%.

References

[1] G. Sines and Y. A. Sakellarakis, *Lenses in antiquity*, American Journal of Archaeology , 191 (1987).

[2] J. M. Enoch, *Ancient lenses in art and sculpture and the objects viewed through them, dating back 4500 years*, in *Photonics West'98 Electronic Imaging*, pages 424–430, International Society for Optics and Photonics, 1998.

[3] Archimedes, *Burning ray (translation from lost greek manuscript)*, Tareq Rajab Museum, Kuwait, 902 AD.

[4] Pliny the Elder, *The natural history XXXVI*, London, H. G. Bohn, 1855.

[5] W. T. Hill III and C. H. Lee, *Light-matter interaction*, John Wiley & Sons, 2008.

[6] C. Wilson, *The invisible world: early modern philosophy and the invention of the microscope*, volume 228, Cambridge Univ Press, 1995.

[7] H. C. King, *The history of the telescope*, Courier Corporation, 1955.

[8] D. B. Keck, *Optical fiber spans 30 years*, Lightwave **17**, 78 (2000).

[9] P. Würfel, *Physics of Solar Cells*, 2005.

[10] V. V. Tuchin and V. Tuchin, *Tissue optics: light scattering methods and instruments for medical diagnosis*, volume 13, SPIE press Bellingham, 2007.

[11] D. A. Steigerwald, J. C. Bhat, D. Collins, R. M. Fletcher, M. O. Holcomb, M. J. Ludowise, P. S. Martin, and S. L. Rudaz, *Illumination with solid state lighting technology*, Selected Topics in Quantum Electronics, IEEE Journal of **8**, 310 (2002).

[12] M. Born and E. Wolf, *Principles of optics: electromagnetic theory of propagation, interference and diffraction of light*, CUP Archive, 2000.

[13] L. Novotny and B. Hecht, *Principles of nano-optics*, Cambridge university press, 2012.

[14] M. R. Dennis, K. O'Holleran, and M. J. Padgett, *Chapter 5 Singular Optics: Optical Vortices and Polarization Singularities*, Progress in Optics **53**, 293 (2009).

[15] J. F. Nye, *Natural focusing and fine structure of light: caustics and wave dislocations*, CRC Press, 1999.

[16] G. A. Siviloglou, J. Broky, A. Dogariu, and D. N. Christodoulides, *Observation of accelerating Airy beams*, Physical Review Letters **99**, 213901 (2007).

[17] W. T. M. Irvine and D. Bouwmeester, *Linked and knotted beams of light*, Nature Physics **4**, 716 (2008).

[18] M. R. Dennis, R. P. King, B. Jack, K. O'Holleran, and M. J. Padgett, *Isolated optical vortex knots*, Nature Physics **6**, 118 (2010).

[19] S. Kühn, U. Håkanson, L. Rogobete, and V. Sandoghdar, *Enhancement of single-molecule fluorescence using a gold nanoparticle as an optical nanoantenna*, Physical review letters **97**, 17402 (2006).

[20] S. Lal, S. E. Clare, and N. J. Halas, *Nanoshell-enabled photothermal cancer therapy: impending clinical impact*, Accounts of chemical research **41**, 1842 (2008).

[21] T. Baba, *Slow light in photonic crystals*, Nature Photonics **2**, 465 (2008).

[22] B. le Feber, N. Rotenberg, and L. Kuipers, *Nanophotonic control of circular dipole emission*, Nature Communications **6**, 6695 (2015).

[23] R. J. Coles, D. M. Price, J. E. Dixon, B. Royall, E. Clarke, P. Kok, M. S. Skolnick, A. M. Fox, and M. N. Makhonin, *Chirality of nanophotonic waveguide with embedded quantum emitter for unidirectional spin transfer*, Nat Commun **7** (2016).

[24] M. Kauranen and A. V. Zayats, *Nonlinear plasmonics*, Nature Photonics **6**, 737 (2012).

[25] S. A. Maier and H. A. Atwater, *Plasmonics: Localization and guiding of electromagnetic energy in metal/dielectric structures*, Journal of Applied Physics **98**, 11101 (2005).

[26] Y. Gorodetski, A. Niv, V. Kleiner, and E. Hasman, *Observation of the spin-based plasmonic effect in nanoscale structures*, Physical review letters **101**, 43903 (2008).

[27] X. Pang, G. Gbur, and T. D. Visser, *Cycle of phase, coherence and polarization singularities in Young's three-pinhole experiment*, Optics Express **23**, 34093 (2015).

[28] H. F. Schouten, T. D. Visser, G. Gbur, D. Lenstra, and H. Blok, *Connection between phase singularities and the radiation pattern of a slit in a metal plate.*, Physical review letters **93**, 173901 (2004).

[29] M. R. Dennis, *Topological singularities in wave fields*, 2001.

[30] J. F. Nye and M. V. Berry, *Dislocations in Wave Trains*, Proceedings of the Royal Society A: Mathematical, Physical and Engineering Sciences **336**, 165 (1974).

[31] J. W. Goodman, *Speckle phenomena in optics: theory and applications*, Roberts and Company Publishers, 2007.

[32] W. Wang, M. R. Dennis, R. Ishijima, T. Yokozeki, A. Matsuda, S. G. Hanson, and M. Takeda, *PoincarÚ sphere representation for the anisotropy of phase singularities and its applications to optical vortex metrology for fluid mechanical analysis*, Optics express **15**, 11008 (2007).

[33] B. Hecht, B. Sick, U. P. Wild, V. Deckert, R. Zenobi, O. J. F. Martin, and D. W. Pohl, *Scanning near-field optical microscopy with aperture probes: Fundamentals and applications*, The Journal of Chemical Physics **112**, 7761 (2013).

[34] W. Whewell, *Researches on the tides. Sixth series. On the results of an extensive system of tide observations made on the coasts of Europe and America in June 1835*, Philosophical Transactions of the Royal Society of London **126**, 289 (1836).

[35] N. P. M. Huck, W. F. Jager, B. de Lange, and B. L. Feringa, *Dynamic control and amplification of molecular chirality by circular polarized light*, Science **273**, 1686 (1996).

[36] M. V. Berry and M. R. Dennis, *Polarization singularities in isotropic random vector waves*, Proceedings of the Royal Society A: Mathematical, Physical and Engineering Sciences **457**, 141 (2001).

[37] M. Burresi, R. J. P. Engelen, A. Opheij, D. Van Oosten, D. Mori, T. Baba, and L. Kuipers, *Observation of polarization singularities at the nanoscale*, Physical Review Letters **102** (2009).

[38] E. Collett, *Field guide to polarization*, volume 15, SPIE press Bellingham, WA, 2005.

[39] P. Lodahl, A. F. Van Driel, I. S. Nikolaev, A. Irman, K. Overgaag, D. Vanmaekelbergh, and W. L. Vos, *Controlling the dynamics of spontaneous emission from quantum dots by photonic crystals*, Nature **430**, 654 (2004).

[40] R. W. Boyd, *Nonlinear Optics*, volume 5, 2003.

[41] P. A. Franken, A. E. Hill, C. W. el Peters, and G. Weinreich, *Generation of optical harmonics*, Physical Review Letters **7**, 118 (1961).

[42] T. H. Maiman, *Stimulated optical radiation in ruby*, (1960).

[43] H. H. Arnaut and G. A. Barbosa, *Orbital and intrinsic angular momentum of single photons and entangled pairs of photons generated by parametric down-conversion*, Physical review letters **85**, 286 (2000).

[44] R. W. Wood, *XLII. On a remarkable case of uneven distribution of light in a diffraction grating spectrum*, The London, Edinburgh, and Dublin Philosophical Magazine and Journal of Science **4**, 396 (1902).

[45] D. Pines, *Collective energy losses in solids*, Reviews of Modern Physics **28**, 184 (1956).

[46] W. Steinmann, *Experimental verification of radiation of plasma oscillations in thin silver films*, Physical Review Letters **5**, 470 (1960).

[47] R. H. Ritchie, *Plasma losses by fast electrons in thin films*, Physical Review **106**, 874 (1957).

[48] C. J. Powell and J. B. Swan, *Origin of the characteristic electron energy losses in aluminum*, Physical Review **115**, 869 (1959).

[49] T. W. Ebbesen, H. J. Lezec, H. F. Ghaemi, T. Thio, and P. A. Wolff, *Extraordinary optical transmission through sub-wavelength hole arrays*, Nature **391**, 667 (1998).

[50] P. B. Johnson and R. W. Christy, *Optical constants of the noble metals*, Physical Review B **6**, 4370 (1972).

[51] N. Rotenberg, T. L. Krijger, B. le Feber, M. Spasenović, F. J. G. de Abajo, and L. Kuipers, *Magnetic and electric response of single subwavelength holes*, Physical Review B **88**, 241408 (2013).

[52] N. Rotenberg, M. Spasenović, T. L. Krijger, B. Le Feber, F. J. García De Abajo, and L. Kuipers, *Plasmon scattering from single subwavelength holes*, Physical Review Letters **108** (2012).

[53] E. Verhagen, M. Spasenović, A. Polman, and L. Kuipers, *Nanowire plasmon excitation by adiabatic mode transformation*, Physical Review Letters **102** (2009).

[54] M. Stockman, *Nanofocusing of Optical Energy in Tapered Plasmonic Waveguides*, 2004.

[55] A. Sommerfeld, *Ueber die Fortpflanzung elektrodynamischer Wellen längs eines Drahtes*, Annalen der Physik **303**, 233 (1899).

[56] K. Wang and D. M. Mittleman, *Metal wires for terahertz wave guiding*, Nature **432**, 376 (2004).

[57] D. J. Dikken, M. Spasenović, E. Verhagen, D. van Oosten, and L. K. Kuipers, *Characterization of bending losses for curved plasmonic nanowire waveguides*, Optics express **18**, 16112 (2010).

[58] E. Synge, *XXXVIII. A suggested method for extending microscopic resolution into the ultra-microscopic region*, The London, Edinburgh, and Dublin Philosophical Magazine and Journal of Science **6**, 356 (1928).

[59] D. Pohl, *Optical scanning near-field microscope*, 1984.

[60] D. W. Pohl, W. Denk, and M. Lanz, *Optical stethoscopy: Image recording with resolution λ/20*, Applied physics letters **44**, 651 (1984).

[61] E. Betzig, J. K. Trautman, T. D. Harris, J. S. Weiner, and R. L. Kostelak, *Breaking the diffraction barrier: optical microscopy on a nanometric scale*, Science **251**, 1468 (1991).

[62] J. A. Veerman, A. M. Otter, L. Kuipers, and N. F. Van Hulst, *High definition aperture probes for near-field optical microscopy fabricated by focused ion beam milling*, Applied Physics Letters **72**, 3115 (1998).

[63] K. Karrai and R. D. Grober, *Piezoelectric tipâsample distance control for near field optical microscopes*, Applied physics letters **66**, 1842 (1995).

[64] B. Le Feber, N. Rotenberg, D. M. Beggs, and L. Kuipers, *Simultaneous measurement of nanoscale electric and magnetic optical fields*, Nature Photonics **8**, 43 (2014).

[65] N. Rotenberg and L. Kuipers, *Mapping nanoscale light fields*, Nature Photonics **8**, 919 (2014).

[66] M. Sandtke, R. J. P. Engelen, H. Schoenmaker, I. Attema, H. Dekker, I. Cerjak, J. P. Korterik, F. B. Segerink, and L. Kuipers, *Novel instrument for surface plasmon polariton tracking in space and time*, Review of Scientific Instruments **79** (2008).

[67] M. Balistreri, J. Korterik, L. Kuipers, and van Hulst NF, *Local observations of phase singularities in optical fields in waveguide structures*, Physical review letters **85**, 294 (2000).

[68] A. Nesci, R. Dändliker, and H. P. Herzig, *Quantitative amplitude and phase measurement by use of a heterodyne scanning near-field optical microscope*, Optics letters **26**, 208 (2001).

[69] M. Ayache, M. P. Nezhad, S. Zamek, M. Abashin, and Y. Fainman, *Near-field measurement of amplitude and phase in silicon waveguides with liquid cladding*, Optics letters **36**, 1869 (2011).

[70] R. L. Byer, *Nonlinear optics and solid-state lasers: 2000*, IEEE Journal on Selected Topics in Quantum Electronics **6**, 911 (2000).

[71] Y. Barad, H. Eisenberg, M. Horowitz, and Y. Silberberg, *Nonlinear scanning laser microscopy by third harmonic generation*, Applied Physics Letters **70**, 922 (1997).

[72] D. Cotter, R. J. Manning, K. J. Blow, A. D. Ellis, A. E. Kelly, D. Nesset, I. D. Phillips, A. J. Poustie, and D. C. Rogers, *Nonlinear Optics for High-Speed Digital Information Processing*, Science **286**, 1523 (1999).

[73] B. Corcoran, C. Monat, C. Grillet, D. J. Moss, B. J. Eggleton, T. P. White, L. O'Faolain, and T. F. Krauss, *Green light emission in silicon through slow-light enhanced third-harmonic generation in photonic-crystal waveguides*, 2009.

[74] M. A. Foster, A. C. Turner, M. Lipson, and A. L. Gaeta, *Nonlinear optics in photonic nanowires.*, Optics express **16**, 1300 (2008).

[75] C. Monat, M. de Sterke, and B. J. Eggleton, *Slow light enhanced nonlinear optics in periodic structures*, 2010.

[76] D. E. Chang, V. Vuletić, and M. D. Lukin, *Quantum nonlinear opticsÂ âÂ photon by photon*, Nature Photonics , 685 (2014).

[77] M. Wulf, A. D. Hoogh, N. Rotenberg, and L. Kuipers, *Ultrafast Plasmonics on Gold Nanowires: Confinement, Dispersion, and Pulse Propagation*, ACS Photonics **1**, 1173 (2014).

[78] L. Novotny and N. van Hulst, *Antennas for light*, 2011.

[79] M. Danckwerts and L. Novotny, *Optical frequency mixing at coupled gold nanoparticles*, Physical Review Letters **98** (2007).

[80] T. Hanke, J. Cesar, V. Knittel, A. Trügler, U. Hohenester, A. Leitenstorfer, and R. Bratschitsch, *Tailoring spatiotemporal light confinement in single plasmonic nanoantennas*, Nano Letters **12**, 992 (2012).

[81] V. K. Valev, J. J. Baumberg, B. De Clercq, N. Braz, X. Zheng, E. J. Osley, S. Vandendriessche, M. Hojeij, C. Blejean, J. Mertens, C. G. Biris, V. Volskiy, M. Ameloot, Y. Ekinci, G. A. E. Vandenbosch, P. A. Warburton, V. V.

Moshchalkov, N. C. Panoiu, and T. Verbiest, *Nonlinear superchiral metasurfaces: Tuning chirality and disentangling non-reciprocity at the nanoscale*, Advanced Materials **26**, 4074 (2014).

[82] A. Salomon, M. Zielinski, R. Kolkowski, J. Zyss, and Y. Prior, *Size and shape resonances in second harmonic generation from silver nanocavities*, Journal of Physical Chemistry C **117**, 22377 (2013).

[83] Y. Zhang, F. Wen, Y.-R. Zhen, P. Nordlander, and N. J. Halas, *Coherent Fano resonances in a plasmonic nanocluster enhance optical four-wave mixing.*, Proceedings of the National Academy of Sciences of the United States of America **110**, 9215 (2013).

[84] J. van Nieuwstadt, M. Sandtke, R. Harmsen, F. Segerink, J. Prangsma, S. Enoch, and L. Kuipers, *Strong Modification of the Nonlinear Optical Response of Metallic Subwavelength Hole Arrays*, Physical Review Letters **97**, 1 (2006).

[85] H. J. Simon, D. E. Mitchell, and J. G. Watson, *Optical second-harmonic generation with surface plasmons in silver films*, Physical Review Letters **33**, 1531 (1974).

[86] S. Palomba and L. Novotny, *Nonlinear excitation of surface plasmon polaritons by four-wave mixing*, Physical Review Letters **101** (2008).

[87] C. C. Neacsu, G. a. Reider, and M. B. Raschke, *Second-harmonic generation from nanoscopic metal tips: Symmetry selection rules for single asymmetric nanostructures*, Physical Review B - Condensed Matter and Materials Physics **71**, 1 (2005).

[88] S. Schmidt, B. Piglosiewicz, D. Sadiq, J. Shirdel, J. S. Lee, P. Vasa, N. Park, D. S. Kim, and C. Lienau, *Adiabatic nanofocusing on ultrasmooth single-crystalline gold tapers creates a 10-nm-sized light source with few-cycle time resolution*, ACS Nano **6**, 6040 (2012).

[89] K. F. MacDonald, Z. L. Samson, M. I. Stockman, and N. I. Zheludev, *Ultrafast active plasmonics: transmission and control of femtosecond plasmon signals*, **3**, 4 (2008).

[90] E. Verhagen, A. Polman, and L. K. Kuipers, *Nanofocusing in laterally tapered plasmonic waveguides.*, Optics express **16**, 45 (2008).

[91] J. E. Sipe, V. C. Y. So, M. Fukui, and G. I. Stegeman, *Analysis of second-harmonic generation at metal surfaces*, Physical Review B **21**, 4389 (1980).

[92] F. X. Wang, F. J. Rodríguez, W. M. Albers, R. Ahorinta, J. E. Sipe, and M. Kauranen, *Surface and bulk contributions to the second-order nonlinear optical response of a gold film*, 2009.

[93] B. Canfield, S. Kujala, K. Jefimovs, J. Turunen, and M. Kauranen, *Linear and nonlinear optical responses influenced by broken symmetry in an array of gold nanoparticles.*, Optics express **12**, 5418 (2004).

[94] A. Mooradian, *Photoluminescence of metals*, Physical Review Letters **22**, 185 (1969).

[95] S. Linden, J. Kuhl, and H. Giessen, *Controlling the interaction between light and gold nanoparticles: Selective suppression of extinction*, Physical Review Letters **86**, 4688 (2001).

[96] M. I. Stockman, M. F. Kling, U. Kleineberg, and F. Krausz, *Attosecond nanoplasmonic-field microscope*, Nature Photonics **1**, 539 (2007).

[97] B. Hecht, B. Sick, U. P. Wild, V. Deckert, O. Zenobi, R. Martin, and D. W. Pohl, *Scanning near-field optical microscopy with aperture probes: fundamentals and applications.*, The Journal of Chemical Physics **112**, 7761 (2000).

[98] L. Duo, P. Biagioni, and M. Finazzi, *Recent developments in linear and nonlinear near-field microscopy on single plasmonic nanoparticles.*, Physica Status Solidi B **247**, 2040 (2010).

[99] M. A. Paesler and P. J. Moyer, *Near-Field Optics: Theory, Instrumentation and Applications.*, Willey (1996).

[100] M. Schnell, A. GarcÃa-Etxarri, A. J. Huber, K. Crozier, J. Aizpurua, and R. Hillenbrand, *Controlling the near-field oscillations of loaded plasmonic nanoantennas.*, Nat. Photon. **3**, 287 (2009).

[101] E. Yoxall, M. Schnell, A. Y. Nikitin, O. Txoperena, A. Woessner, M. B. Lundeberg, F. Casanova, L. E. Hueso, F. H. L. Koppens, and R. Hillenbrand, *Direct observation of ultraslow hyperbolic polariton propagation with negative phase velocity.*, Nat. Photon. , advanced online publication (2015).

[102] M. Frimmer, Y. Chen, and A. F. Koenderink, *Scanning emitter lifetime imaging microscopy for spontaneous emission control.*, Phys. Rev. Lett. **107**, 123602 (2011).

[103] N. Rotenberg and L. Kuipers, *Mapping nanoscale light fields.*, Nature Photonics **8**, 919 (2014).

[104] E. Betzig and R. J. Cichester, *Single molecules observed by near-field scanning optical microscopy.*, Science **262**, 1422 (1993).

[105] A. F. Koenderink, A. Alu, and A. Polman, *Nanophotonics: Shrinking light-based technology.*, Science **348**, 516 (2015).

[106] B. Hecht, H. Bielefeldt, Y. Inouye, D. W. Pohl, and L. Novotny, *Facts and artifacts in near-field optical microscopy.*, J. Appl. Phys. **81**, 2492 (1997).

[107] W. L. Barnes, A. Dereux, and W. Ebbesen, *Surface plasmon subwavelength optics.*, Nature **424**, 824 (2003).

[108] J. C. Weeber, J. R. Krenn, A. Dereux, B. Lamprecht, Y. Lacroute, and J. P. Goudonnet, *Near-field observation of surface plasmon polariton propagation on thin metal stripes.*, Phys. Rev. B **64**, 045411 (2001).

[109] D. K. Gramotnev and S. I. Bozhevolny, *Plasmonics beyond the diffraction limit.*, Nature Photon. **4**, 83 (2010).

[110] B. Steinberger, A. Hohenau, H. Ditlbacher, A. L. Stepanov, A. Drezet, F. R. Aussenegg, A. Leitner, and K. J. R., *Dielectric stripes on gold as surface plasmon waveguides.*, Appl. Phys. Lett. **88**, 094104 (2006).

[111] E. Verhagen, M. Spasenovic, A. Polman, and L. Kuipers, *Nanowire plasmon excitation by adiabatic mode transformation.*, Physics Review Letters **102**, 203904 (2009).

[112] J. Prikulis, H. Xu, L. Gunnarsson, and M. Kall, *Phase-sensitive near-field imaging of metal nanoparticles.*, J. Appl. Phys. **92**, 6211 (2002).

[113] A. de Hoogh, N. Rotenberg, and L. Kuipers, *Optical singularities in plasmonic fields near single subwavelength holes.*, Journal of Optics **16**, 114004 (2014).

[114] A. de Hoogh, L. Kuipers, T. D. Visser, and N. Rotenberg, *Creating and controlling polarization singularities in plasmonic fields.*, Photonics **2**, 553 (2015).

[115] A. Nesci and O. J. F. Martin, *Optical nano-imaging of metallic nanostructures.*, Proceedings of the SPIE **5928**, 59280U1 (2005).

[116] A. E. Klein, N. Janunts, M. Steinert, A. TÃ$\frac{1}{4}$nnermann, and T. Pertsch, *Polarization-resolved near-field mapping of plasmonic aperture emission by a dual-SNOM system.*, Proceedings of the SPIE **14**, 5010â5015 (2014).

[117] B. le Feber, N. Rotenberg, D. M. Beggs, and L. Kuipers, *Simultaneous measurements of nanoscale electric and magnetic optical fields.*, Nature Photon. **8**, 43 (2013).

[118] H. W. Kihm, J. Kim, S. Koo, J. Ahn, K. Ahn, K. Lee, and D.-S. Park, N.and Kim, *Optical magnetic field mapping using a subwavelength aperture.*, Optics Express **21**, 5625 (2013).

[119] D. Permyakov, I. Sinev, D. Markovich, P. Ginzburg, A. Samusev, P. Belov, V. Valuckas, A. I. Kuznetsov, B. S. Luk'yanchuk, A. E. Miroshnichenko, D. N. Neshev, and K. Y. S., *Probing magnetic and electric optical responses of silicon nanoparticles.*, Appl. Phys. Lett. **106**, 171110 (2015).

[120] N. Rotenberg, B. le Feber, T. D. Visser, and L. Kuipers, *Tracking nanoscale electric and magnetic singularities through three-dimensional space.*, Optica **2**, 540 (2015).

[121] R. M. Bakker, P. D., Y. F. Yu, D. Markovich, R. Paniagua-Dominguez, L. Gonzaga, A. Samusev, Y. Kivshar, B. Luk'yanchuk, and A. I. Kuznetsov, *Magnetic and electric hotspots with silicon nanodimers.*, Nano Lett. **15**, 2137 (2015).

[122] K. G. Lee, H. W. Kihm, J. E. Kihm, W. J. Choi, H. Kim, C. Ropers, D. J. Park, Y. C. Yoon, S. B. Choi, D. H. Woo, J. Kim, B. Lee, Q. H. Park, C. Lienau, and D. S. Kim, *Vector field microscopic imaging of light*, Nature Photonics **1**, 53 (2007).

[123] E. Devaux, A. Dereux, E. Bourillot, J. C. Weeber, Y. Lacroute, and J. P. Goudonnet, *Local detection of the optical magnetic field in the near zone of dielectric samples*, Physical Review B - Condensed Matter and Materials Physics **62**, 10504 (2000).

[124] M. Wulf, A. de Hoogh, N. Rotenberg, and L. Kuipers, *Ultrafast plasmonics on gold nanowires: confinement, dispersion, and pulse propagation.*, ACS Photonics **1**, 1173 (2014).

[125] CRC Handbook of Chemistry and Physics. , http://www.hbcpnetbase.com/.

[126] J. J. Greffet and R. Carminati, *Image formation in near-field optics.*, Pro. Surf. Sci. **56**, 133 (1997).

[127] M. Esslinger and R. Vogelgesang, *Reciprocity theory of apertureless scanning near-field optical microscopy with point-dipole probes.*, ACS Nano **6**, 8173 (2012).

[128] J. A. Porto, R. Carminati, and J. J. Greffet, *Theory of electromagnetic field imaging and spectroscopy in scanning near-field optical microscopy.*, J. Appl. Phys. **88**, 4845 (2000).

[129] J. Veerman, M. F. Garcia-Parajo, L. Kuipers, and N. F. van Hulst, *Single molecule mapping of the optical field distribution of probes for near-field microscopy.*, J. Microsc. **194**, 477 (1999).

[130] D. K. Singh, J. S. Ahn, S. Koo, T. Kang, J. Kim, S. Lee, N. Park, and D.-S. Kim, *Selective electric and magnetic sensitivity of aperture probes*, Optics Express **23**, 20820 (2015).

[131] H. W. Kihm, S. M. Koo, Q. H. Kim, K. Bao, J. E. Kihm, W. S. Bak, S. H. Eah, C. Lienau, H. Kim, P. Nordlander, N. J. Halas, N. K. Park, and D.-S. Kim, *Bethe-hole polarization analyser for the magnetic vector of light.*, Nature communications **2**, 451 (2011).

[132] H. Winful, *Self-induced polarization changes in birefringent optical fibers.*, Appl. Phys. Lett. **47**, 213 (1985).

[133] F. Keilmann, *Scattering-type near-field optical microscopy.*, J. Electron. Microsc. (Tokyo) **53**, 187 (2004).

[134] A. Bek, R. Vogelgesang, and K. Kern, *Apertureless scanning near field optical microscope with sub-10nm resolution.*, Rev. Sci. Instrum. **77**, 043703 (2006).

[135] A. Garcia-Etxarri, I. Romero, F. J. G. de Abajo, R. Hillenbrand, and J. Aizpurua, *Influence of the tip in near-field imaging of nanoparticle plasmonic modes: Weak and strong coupling regimes.*, Phys. Rev. B **79**, 125439 (2009).

[136] S. Karaveli and R. Zia, *Spectral tuning by selective enhancement of electric and magnetic dipole emission*, Physical Review Letters **106** (2011).

[137] T. H. Taminiau, S. Karaveli, N. F. van Hulst, and R. Zia, *Quantifying the magnetic nature of light emission*, Nature Communications **3**, 979 (2012).

[138] M. Kasperczyk, S. Person, D. Ananias, L. D. Carlos, and L. Novotny, *Excitation of magnetic dipole transitions at optical frequencies*, Physical Review Letters **114** (2015).

[139] a. T. O'Neil, I. MacVicar, L. Allen, and M. J. Padgett, *Intrinsic and Extrinsic Nature of the Orbital Angular Momentum of a Light Beam*, Phys. Rev. Lett. **88**, 53601 (2002).

[140] A. M. Yao and M. J. Padgett, *Orbital angular momentum: origins, behavior and applications*, Advances in Optics and Photonics **3**, 161 (2011).

[141] N. Shvartsman and I. Freund, *Vortices in random wave fields: Nearest neighbor anticorrelations.*, Physical review letters **72**, 1008 (1994).

[142] J. F. Nye, *Lines of circular polarization in electromagnetic wave fields*, in *Proceedings of the Royal Society of London A: Mathematical, Physical and Engineering Sciences*, volume 389, pages 279–290, The Royal Society, 1983.

[143] H. He, M. Friese, N. Heckenberg, and H. Rubinsztein-Dunlop, *Direct observation of transfer of angular momentum to absorptive particles from a laser beam with a phase singularity.*, Physical review letters **75**, 826 (1995).

[144] R. W. Schoonover and T. D. Visser, *Polarization singularities of focused, radially polarized fields.*, Optics express **14**, 5733 (2006).

[145] M. P. J. Lavery, F. C. Speirits, S. M. Barnett, and M. J. Padgett, *Detection of a spinning object using light's orbital angular momentum.*, Science (New York, N.Y.) **341**, 537 (2013).

[146] X.-L. Cai, J.-W. U. o. B. Wang, M. J. Strain, B. Johnson-Morris, J.-B. Zhu, M. Sorel, J. L. O'Brien, M. G. Thompson, and S.-Y. Yu, *Integrated Compact Optical Vortex Beam Emitters*, Science **338**, 363 (2012).

[147] D. L. Andrews, *Structured light and its applications*, (2008).

[148] E. Flück, M. Hammer, A. M. Otter, J. P. Korterik, L. Kuipers, and N. F. Van Hulst, *Amplitude and phase evolution of optical fields inside periodic photonic structures*, Journal of Lightwave Technology **21**, 1384 (2003).

[149] J. Leach, M. R. Dennis, J. Courtial, and M. J. Padgett, *Laser beams: knotted threads of darkness*, Nature **432**, 165 (2004).

[150] J. Nye and F. J. Wright, *Natural Focusing and Fine Structure of Light: Caustics and Wave Dislocations*, American Journal of Physics **68**, 776 (2000).

[151] I. Freund, *Optical Möbius strips in three-dimensional ellipse fields: I. Lines of circular polarization*, Optics Communications **283**, 1 (2010).

[152] T. F. Krauss, *Slow light in photonic crystal waveguides*, Journal of Physics D: Applied Physics **40**, 2666 (2007).

[153] M. Sandtke and L. Kuipers, *Slow guided surface plasmons at telecom frequencies*, Nature Photonics **1**, 573 (2007).

[154] L. Yang, C. Min, and G. Veronis, *Guided subwavelength slow-light mode supported by a plasmonic waveguide system.*, Optics letters **35**, 4184 (2010).

[155] D. Lin, P. Fan, E. Hasman, and M. L. Brongersma, *Dielectric gradient metasurface optical elements*, Science **345**, 298 (2014).

[156] N. Yu and F. Capasso, *Flat optics with designer metasurfaces.*, Nature materials **13**, 139 (2014).

[157] A. Minovich, A. E. Klein, N. Janunts, T. Pertsch, D. N. Neshev, and Y. S. Kivshar, *Generation and near-field imaging of airy surface plasmons*, Physical Review Letters **107** (2011).

[158] W. Braunbek and G. Laukien, *Einzelheiten zur Halbebenen-Beugung*, Optik **9**, 174 (1952).

[159] I. Söllner, S. Mahmoodian, S. L. Hansen, L. Midolo, A. Javadi, G. KiršanskÄ, T. Pregnolato, H. El-Ella, E. H. Lee, and J. D. Song, *Deterministic photonâemitter coupling in chiral photonic circuits*, Nature nanotechnology **10**, 775 (2015).

[160] A. a. Sukhorukov, S. Ha, A. S. Desyatnikov, A. V. Lavrinenko, and Y. S. Kivshar, *Slow-light vortices in periodic waveguides*, Journal of Optics A: Pure and Applied Optics **11**, 094016 (2009).

[161] N. Rotenberg, B. le Feber, T. D. Visser, and L. Kuipers, *Tracking nanoscale electric and magnetic singularities through three-dimensional space*, Optica **2**, 540 (2015).

[162] A. De Hoogh, N. Rotenberg, and L. Kuipers, *Optical singularities in plasmonic fields near single subwavelength holes*, Journal of Optics **16**, 114004 (2014).

[163] H. Liu and P. Lalanne, *Microscopic theory of the extraordinary optical transmission.*, Nature **452**, 728 (2008).

[164] a. Bek, R. Vogelgesang, and K. Kern, *Apertureless scanning near field optical microscope with sub-10 nm resolution*, Review Of Scientific Instruments **77**, 43703 (2006).

[165] E. Hendry, T. Carpy, J. Johnston, M. Popland, R. V. Mikhaylovskiy, A. J. Lapthorn, S. M. Kelly, L. D. Barron, N. Gadegaard, and M. Kadodwala, *Ultrasensitive detection and characterization of biomolecules using superchiral fields*, Nat Nanotechnol **5**, 783 (2010).

[166] R. Mitsch, C. Sayrin, B. Albrecht, P. Schneeweiss, and A. Rauschenbeutel, *Quantum state-controlled directional spontaneous emission of photons into a nanophotonic waveguide.*, Nature communications **5**, 5713 (2014).

Optical singularities and nonlinear effects near plasmonic nanostructures: Summary

For millenia, light has inspired humankind and has been the source of major technological advances. The first technologies that used light increased our understanding of many processes and phenomena by improving our own visual perception. By the clever use of optical elements such as lenses and mirrors, we could build telescopes to observe distant planets and microscopes to study the cells of which our bodies are composed. Modern light-based technologies have not only allowed us to improve the quality and resolution of optical imaging techniques, but we have also learned how to create smart and artificial light sources and obtain energy from the most powerful light source available to us, the sun. Furthermore, less obvious technologies which also utilize light, include the communication through optical fibers, and the light-mediated sensing of chemical compounds down to the detection sensitivity of single molecules. What all the above named applications have in common, is that they are based upon our ability to control light.

It was noticed since antiquity that light can interact differently with different materials. Depending on the atomic constitution of materials, light could pass through or be reflected, could be absorbed or emitted, and so on. This variety of light-matter interaction provided the means to control light via selecting and shaping materials: the perfect example are glasses that allow people with an eye-vision deficiency to see and read properly. In modern times we have been able to create artificial materials with custom-made optical properties, paving the way to new possibilities in light-matter control. One of these possibilities is the control of visible light on the nanoscale, namely at length scales below its wavelength, for miniaturization of modern technologies and the discovery of novel optical phenomena.

One promising way to manipulate light on the nanoscale is to exploit the properties of light when it interacts with metallic elements. Light can, for instance, be guided along the interface of a metal and a dielectric. These guided waves are called surface plasmon polaritons (SPPs), and they occur because the collective oscillations of free electrons of the metal interact with the light waves and vice versa. The wavelength of the SPP itself is (much) shorter than the wavelength of light, resulting in a tight confinement and strong enhancement of the field. The light fields interacting with plasmonic systems can vary more rigorously in space than normal beams; they can be much richer in structure and exhibit fascinating patterns. A variety of different plasmonic platforms have been studied or proposed in literature to create unique structured field patterns.

In this thesis, we have created structured light using various plasmonic platforms to investigate and control optical phenomena at the smallest possible scale. The phenomena on which we focused our attention were: (a) nonlinear plasmonics and (b) the rich physics behind optical singularities.

One major route to control light is via nonlinear effects. While in linear optics the frequency of light is constant, nonlinear optics can convert the frequency of light to newly generated frequencies, therefore providing novel light sources at any chosen frequency. An example of such a nonlinear effect is second-harmonic generation (SHG) where the frequency of light is doubled. Likewise, in third-harmonic generation (THG), the original frequency is tripled. Nonlinear optical effects, which are typically weak in nature, can be enhanced by increasing the light intensities. SHG and THG, for instance, depend on the intensity of the source to the power of 2 and 3, respectively. Nonlinearities can therefore benefit from the strong local intensities near plasmonic structures.

In chapter 2 we demonstrate experimentally that guided modes of plasmonic nanowires can be used for nonlinear optics. By coupling light from a near-infrared pulsed laser to the guided modes of single nanowires with variable widths, we exploit the strong plasmonic field enhancement to generate harmonic signals from the propagating plasmonic mode. We observe both second- and third-harmonic generation of light in the far field via the scattering of red and green light (2nd and 3rd harmonic) along the nanowire. From our analysis of the spatial dependence of the harmonic signals we confirm that the near-infrared SPPs, which are guided along the nanowire, are indeed the source of the harmonics.

This nonlinear plasmonics approach allows us to control the propagating light frequency along metallic nanowires. The observation of nonlinear effects (the harmonics) originating from guided SPP modes opens the way towards future applications which are based on nonlinear plasmonics. Ultimately, multiple wires could be integrated into an entire nonlinear network either for integrated logic or for controllable light sources on the nanoscale.

In this thesis, we have also controlled optical properties of light fields near plasmonic systems, such as the direction of the light fields, typically denoted as the polarization. In structured light fields, the polarization of light can change over small length scales, containing polarization features which can even be infinitely small in

size. Clear examples are points where the polarization is locally circular, named C-points. Light close around the C-point is elliptically polarized and contains all possible elliptical orientations of light, but at this exact point the polarization is perfectly circular and consequently the orientation of the ellipse is undefined. Similarly, on L-lines the polarization is linear and the handedness of light is undetermined. C-points and L-lines are examples of polarization singularities; singular, because a certain property of the polarization (e.g. handedness or orientation) at such locations becomes degenerate.

Optical singularities have infinitesimal sizes and therefore require high resolution instruments to fully image their local properties. Moreover, the polarization of light is dependent both on the amplitude and phase of light for each planar component (x and y). Hence, to identify optical singularities, a phase- and polarization-sensitive instrument is required to fully characterize and map the polarization. A near-field optical microscope allows us to map at nanometric resolution the electromagnetic field components in the proximity of optical singularities via scanning of a nano-probe along the surface of the sample.

The response of a near-field probe to the underlying electromagnetic fields is relatively intricate as it involves both electric and magnetic field components. To understand how the polarized fields near a plasmonic nanowire are imaged with a near-field microscope, in chapter 3 we perform measurements and numerical simulations of the plasmonic nanowire and the probe aperture itself. We use the optical reciprocity theorem to take the response of the aperture probe into consideration and reconstruct the theoretical expectations for the measured signals. By implementing this theorem, we find good agreement between experiments and our theoretical predictions. From the analysis of the measured signals we conclude that the collected light above the plasmonic nanowire is a combination of electric and magnetic fields, where the magnetic field contribution is significant.

In chapter 4 we present the results of our search for the simplest plasmonic system that contains polarization singularities, and that allows us to observe and control them. We investigate the polarization patterns in the near-field distributions that result from scattering of SPPs from a single subwavelength hole in a gold film. We identify polarization singularities in both near-field measurements as well as numerical calculations and find qualitatively good agreement between theory and experiments. Additionally, we show that by varying the size of the subwavelength hole or the width of the incident SPP beam we can control the position of the polarization singularities and, as a result, their field amplitude by over 3 orders of magnitude. Because the control over the polarization singularities is achievable by tuning physically adjustable parameters of the system (the hole diameter and beam width), we can expect that our results create possibilities for its use in future on-chip applications requiring structured light fields.

In chapter 5, we enrich the structure of light by considering multiple holes positioned in a gold film. We find that the plasmonic light fields scattered from two or three subwavelength holes, positioned in series, exhibit singularities. Controlling the polarization of the incident illumination beam with respect to the position of

the holes, allows us to select where these singularities are created, their charge and the topology of the field surrounding them. We find for the two-hole system, as the distance between the holes is increased, that C-points are created in multiples of eight. This quantization can be explained using symmetry arguments and conservation laws. These results demonstrate the promise of this plasmonic platform as a tool for studying and controlling fundamental properties of light fields, and may be important to applications where control over these properties is required at the nanoscale.

In this thesis we have demonstrated experimentally and numerically two major ways to control light at the nanoscale using guided plasmonic modes. One major direction has been to control the frequency of light in a plasmonic nanowire via nonlinear effects. Another direction has been the search for optical singularities in plasmonics systems and investigate optimal routes towards their control. The guided plasmonics modes used throughout this thesis can be integrated for on-chip applications that make use of frequency conversion or polarization control.

Samenvatting in het Nederlands

Al millennia lang heeft licht de mensheid geïnspireerd en gediend als bron voor belangrijke technologische voortgang. De eerste technieken die gebruik maakten van licht vergrootten ons begrip van vele natuurwetenschappelijke processen en fenomenen, simpelweg door het verbeteren van onze visuele perceptie. Door slim gebruik te maken van optische elementen, zoals lenzen en spiegels, konden we bijvoorbeeld enerzijds telescopen bouwen om hemellichamen te aanschouwen die zonder hulpmiddelen onzichtbaar waren voor het menselijk oog. Anderzijds construeerden we microscopen die het mogelijk maakten om individuele cellen te bestuderen waaruit onder andere mens en dier zijn opgebouwd. Moderne technologieën die gebruik maken van licht hebben niet alleen de kwaliteit en resolutie van optische beelden verbeterd, ze maakten het ook mogelijk om intelligente en kunstmatige lichtbronnen te creëren en energie op te wekken uit de meest krachtige lichtbron die voor ons beschikbaar is: de zon. Ook minder bekende technieken die gebruik maken van licht profiteerden van de technologische groei, zoals de communicatie door optische glasvezels en de lichtgestuurde detectie van chemische componenten, die inmiddels de precisie van slechts enkele moleculen nadert. Wat al deze technieken gemeen hebben, is dat ze afhankelijk zijn van onze mogelijkheid om licht te reguleren.

Sinds de oudheid weet men dat licht verschillend kan reageren op verschillende materialen. Afhankelijk van de atomaire samenstelling van een materiaal kan licht door materie voortbewegen of worden gereflecteerd, worden geabsorbeerd of zelfs uitgezonden. De variatie van de verschillende manieren van interactie tussen licht en materie gaf ons de mogelijkheid om licht naar onze hand te zetten. Een welbekend voorbeeld is de ontwikkeling van brillen en lenzen om mensen met gebrekkig zicht scherp te laten zien en lezen. Door het juiste materiaal op een specifieke manier te vormen kan het scherptepunt van een oog naar wens worden gecorrigeerd.

Recentere ontwikkelingen hebben het eveneens mogelijk gemaakt om kunstmatige materialen te ontwikkelen met speciaal samengestelde eigenschappen. Een van deze ontwikkelingen is het manipuleren van (zichtbaar) licht op een lengteschaal (vele malen) kleiner dan diens golflengte, de nanoschaal. Dit maakt miniaturisatie van

hedendaagse technologieën mogelijk en draagt tevens bij aan de ontdekking van nieuwe optische fenomenen.

Een veelbelovende methode om licht op de nanoschaal te manipuleren maakt gebruik van de interactie tussen licht en metaal. Licht kan bijvoorbeeld voortbewegen langs het grensvlak tussen een metaal en een diëlektrisch medium, zoals lucht. Deze gestuurde golven worden ook wel oppervlakte plasmon polaritonen genoemd en komen voort uit de interactie van collectieve oscillaties van de vrije elektronen in het metaal met lichtgolven, en vice versa. De golflengte van zo'n oppervlakte plasmon polariton zelf kan (veel) korter dan de golflengte van licht zijn, wat resulteert in een strakke begrenzing van licht in de ruimte en flink versterkte veldintensiteiten. Ook de patronen van lichtvelden rondom plasmonische systemen kunnen sneller variëren in de ruimte; het licht is rijk in structuur en kan fascinerende patronen vertonen. Tot op heden zijn verschillende plasmonische systemen bestudeerd of geopperd in de literatuur om unieke gestructureerde veldpatronen te creëren.

In dit proefschrift hebben we licht gestructureerd met verschillende plasmonische systemen om optische fenomenen te bestuderen en manipuleren op de kleinst mogelijke schaal. De fenomenen waar wij onze aandacht op gericht hebben zijn: (a) niet-lineaire plasmonica en (b) de rijke natuurkunde achter optische singulariteiten.

Een belangrijke route om licht te controleren is via niet-lineaire effecten. Anders dan in lineaire optica, waar de frequentie van licht altijd gelijk blijft, kan niet-lineaire optica de frequentie van licht omzetten naar nieuw gegenereerde frequenties. Het kan hierdoor dienen als lichtbron voor iedere gekozen nieuwe frequentie. Een voorbeeld van zo'n fenomeen is tweedeharmonische generatie, waarbij de frequentie van licht wordt verdubbeld. Vergelijkbaar met dit proces is derdeharmonische generatie, waarbij de originele frequentie wordt verdrievoudigd. Niet-lineaire optische effecten zijn van nature typisch zwak, maar kunnen versterkt worden door de intensiteit van het licht te vergroten. Tweede- en derdeharmonische generatie bijvoorbeeld, zijn afhankelijk van de intensiteit van de bron, respectievelijk tot de macht twee en drie. Deze effecten kunnen daarom profiteren van de lokaal sterke veldintensiteiten nabij plasmonische systemen.

In hoofdstuk 2 hebben we experimenteel aangetoond dat voortbewegende oppervlakte plasmon polaritonen als lokale bron kunnen dienen voor niet-lineaire optische effecten. Door infrarood licht te koppelen aan dunne gouddraden met nanometrische dimensies, bevestigd op een glazen oppervlak, hebben we de verhoogde lichtintensiteiten gebruikt rondom de draad om zichtbare harmonische signalen op te wekken. We hebben zowel tweedeharmonische generatie (rood licht) als derdeharmonische generatie (groen licht) waargenomen wat langs individuele gouddraadjes verstrooide naar het verre veld. Door middel van onze analyse van de ruimtelijke afhankelijkheid van de harmonische signalen bevestigen we dat de propagerende infrarode oppervlakte plasmon polaritonen de bron zijn van de harmonische signalen.

Deze niet-lineaire plasmonische methode stelt ons in staat om de frequentie van voortbewegend licht langs metaaldraden te beheersen. De observatie van twee niet-lineaire effecten (harmonische generatie) die beiden ontstaan uit propagerende plasmonen opent de mogelijkheid voor toekomstige toepassingen gebaseerd op niet-lineaire

plasmonica. Uiteindelijk zouden meerdere draden geïntegreerd kunnen worden tot een groter niet-lineair netwerk voor geïntegreerde optische circuits of controleerbare lichtbronnen op de nanoschaal.

In dit proefschrift hebben we ook de optische eigenschappen van lichtvelden nabij plasmonische systemen gemanipuleerd, waaronder de draairichting van lichtvelden (vaak polarisatie genoemd). In gestructureerde lichtvelden kan de polarisatie van licht variëren over extreem kleine lengteschalen. Hierin kunnen zelfs polarisatie kenmerken zitten die oneindig klein van formaat zijn. Een duidelijk voorbeeld zijn punten waar de polarisatie lokaal circulair is, bekend onder de term C-punten. Dicht rondom zo'n C-punt is licht elliptisch gepolariseerd met elke mogelijke elliptische oriëntatie. Exact op een C-punt echter, is licht perfect circulair, waardoor de oriëntatie van de ellips noodzakelijkerwijs ongedefinieerd is. Een ander voorbeeld zijn L-lijnen, waar de polarisatie lineair is en de draairichting van licht (linksom of rechtsom) ongedefinieerd is. Zowel C-punten als L-lijnen zijn voorbeelden van polarisatie singulariteiten; singulair, omdat een specifieke eigenschap van de polarisatie (zoals de draairichting of oriëntatie) op deze plekken ongedefinieerd is.

Aangezien optische singulariteiten oneindig klein zijn is een instrument met superresolutie vereist om hun lokale eigenschappen te bepalen. Bovendien is de polarisatie van licht zowel afhankelijk van de amplitude als de fase van elke lichtcomponent in het bestudeerde vlak (x en y). Om singulariteiten te identificeren is een fase- en polarisatiegevoelig instrument vereist om alle polarisatie eigenschappen in het vlak boven plasmonische sytemen volledig in kaart te kunnen brengen. Een optische nabije veld microscoop maakt het mogelijk met nanometrische precisie de elektromagnetische veldcomponenten in de nabijheid van optische singulariteiten in beeld te brengen. De techniek maakt gebruik van een nano-probe (een dunne met aluminium gecoate glasnaald waarvan het puntje is verwijderd zodat een 200 nm kleine opening ontstaat) die dicht langs het oppervlak van het sample heen en weer wordt gescand en een kleine fractie licht naar een detector stuurt.

De reactie van een nabije veld probe op de onderliggende elektromagnetische velden is echter betrekkelijk ingewikkeld, omdat zowel de elektrische als magnetische veldcomponenten een rol kunnen spelen. Om te begrijpen hoe de gepolariseerde velden nabij een plasmonische nanodraad worden afgebeeld met een nabije veld microscoop, hebben we in hoofdstuk 3 metingen met deze microscoop vlak boven de nanodraad vergeleken met numerieke berekeningen van zowel de plasmonische draad als de probe van de microscoop. Met behulp van theoretische voorspellingen zijn we in staat de gemeten signalen te reconstrueren uit de numerieke simulaties, met goede overeenkomst. Uit deze bevindingen concluderen we dat het licht boven de nanodraad dat verzameld is door de nabije veld microscoop een combinatie is van de elektrische en magnetische velden rond de draad.

In hoofdstuk 4 presenteren we de resultaten van onze zoektocht naar het meest eenvoudige plasmonische systeem dat polarisatie singulariteiten bevat. Bovendien onderzoeken we de mogelijkheden om ze te observeren en beheersen. We onderzoeken de polarisatie patronen in de nabije veldverdelingen die voortvloeien uit de verstrooiing van propagerende plasmonen aan een enkel gat in een goudlaag. We identificeren po-

larisatie singulariteiten in zowel nabije veld metingen als numerieke berekeningen. We vinden kwalitatief goede overeenkomst tussen de theorie en experimenten. We laten zien dat door de diameter van het gat of de breedte van de invallende lichtbundel aan te passen, we de positie van de polarisatie singulariteiten besturen waarbij eveneens de veldsterktes sterk toenemen. Met deze resultaten laten we zien dat controle over polarisatie singulariteiten realiseerbaar is door fysiek instelbare parameters van het systeem te optimaliseren (de diameter van het gat en de breedte van de bundel). We verwachten daarom dat onze bevindingen kunnen bijdragen aan toekomstige on-chip toepassingen en ontwikkelingen die gebruik maken van gestructureerde lichtvelden.

In hoofdstuk 5 verrijken we de structuur van licht door meerdere gaten in een goudlaag aan te brengen. We ontdekken dat plasmonische lichtvelden die verstrooien aan twee of drie gaten, gepositioneerd in serie, optische singulariteiten onthullen. We bestuderen het twee-gaten systeem in detail door de gat-tot-gat afstand stapsgewijs te laten toenemen. We ontdekken hierbij dat C-punten in veelvouden van acht ontstaan, wat te verklaren valt met symmetrie- en behoudswetten. Bovendien kan de verandering van de polarisatie alle C-punten laten verdwijnen. Deze resultaten tonen aan dat dit plasmonische systeem als gereedschap kan dienen voor het bestuderen van fundamentele eigenschappen van lichtvelden op de nanoschaal.

In dit proefschrift hebben we experimenteel en numeriek aangetoond dat we licht op de nanoschaal op twee manieren kunnen manipuleren. Enerzijds hebben we de frequentie van licht langs een nanodraad gemanipuleerd door middel van niet-lineaire effecten. Anderzijds hebben we optische singulariteiten geïdentificeerd in plasmonische systemen en een optimale route richting controle onderzocht. In dit gehele werk is gebruik gemaakt van propagerende plasmonische systemen. Implementatie van deze systemen voor on-chip toepassingen die berusten op omzetting van frequentie of controle van polarisatie is daarom mogelijk.

Notation

$\mathbf{E}$	Electric field vector
$\mathbf{H}$	Magnetic field vector
I	Intensity
A	Amplitude
θ	Phase
ω	Frequency
λ	Wavelength
c	Speed of light in vacuum
$\mathbf{k}$	Wavevector
n	Refractive index
n_{eff}	Effective refractive mode index
P	Polarization density
Z_0	Vacuum impedance
χ	Susceptibility of the material
ϵ	Permittivity
ϵ_0	Vacuum permittivity
μ	Permeability
μ_0	Vacuum permeability
ℓ_p	Propagation length
ℓ_d	Decay length
ℓ_c	Coherence length
p	Electric dipole
m	Magnetic dipole
L	Complex near-field signal
s	Topological charge of a singularity
$\alpha_{E/H}$	Electric/magnetic polarizability
α	Orientation angle of the polarization ellipse
ε	Ellipticity of the polarization ellipse

Common used abbreviations

AOM	Acoustic-optic modulater
C-point	Point of circular polarization
CCD	Charge-coupled device camera
L-line	Line of linear polarization
LED	Light emitting diode
LPR	Local plasmon resonance
NW	Nanowire
ORT	Optical reciprocity theorem
PhCW	Photonic crystal waveguide
PML	Perfectly matched layer
SHG	Second-harmonic generation
SPP	Surface plasmon polariton
TE	Transverse electric
THG	Third-harmonic generation
TM	Transverse magnetic

List of Publications

This thesis is based on the following publications:

1. *Harmonics generation by surface plasmon polaritons on single nanowires*,
   A. de Hoogh, A. Opheij, M. Wulf, N. Rotenberg and L. Kuipers,
   ACS Phot. **3**, 1446 (2016).
   (Chapter 2)

2. *Imaging of electric and magnetic fields near plasmonic nanowires*,
   I.V. Kabakova, A. de Hoogh, R.E.C. van der Wel, M. Wulf, B. le Feber and L. Kuipers,
   Sci. Rep. **6**, 22665 (2016).
   (Chapter 3)

3. *Optical singularities in plasmonic fields near single subwavelength holes*,
   A. de Hoogh, N. Rotenberg and L. Kuipers,
   J. Opt. **16**, 114004 (2014).
   (Chapter 4)

4. *Creating and Controlling Polarization Singularities in Plasmonic Fields*,
   A. de Hoogh, L. Kuipers, T.D. Visser and N. Rotenberg,
   Photonics **2**, 553 (2015).
   (Chapter 5)

Other publications by the author:

1. *Wavelength-selective addressing of visible and near-infrared plasmon resonances for SU8 nanolithography*,
   A. de Hoogh, B. Hommersom and A.F. Koenderink,
   Opt. Express **19**, 11405 (2012).

2. *Layering, freezing, and re-entrant melting of hard spheres in soft confinement*,
   T. Curk, A. de Hoogh, F.J. Martinez-Veracoechea, E. Eiser, D. Frenkel, J. Dobnikar and M.E. Leunissen,
   Phys. Rev. E **85**, 021502 (2012).

3. *Ultrafast plasmonics on gold nanowires: confinement, dispersion, and pulse propagation*,
   M. Wulf, A. de Hoogh, N. Rotenberg and L. Kuipers,
   ACS Phot. **1**, 1173-1180 (2014).

4. *Core-shell plasmonic nanohelices*,
   N.D. Kosters, A. de Hoogh, H. Zeijlemaker, H. Acar, N. Rotenberg and L. Kuipers.
   (submitted)

Acknowledgements

If I was asked up to seven years ago what my career path would have looked like, I would have given numerous broadly varying answers, but a PhD in physics would most certainly not have been one of them. I believe that recognizing all help one receives over a period of time is as important as the actual fruits that are harvested. During my time as a PhD, as well as on the long way towards it, I was blessed to meet a lot of people that were important to me and that supported me in my challenges, decisions and success. Here, I wish to thank all of you that contributed positively to this work. And I foremost want to emphasize that it is not only the people that had a prominent role in my career or life, but also those that just gave me the right advice that directed me to the place I needed to be and the people that provided some positivity or strength when I needed it. To me, the (sum of) small contributions have been just as significant. Rather than mentioning long endless lists of names, I would like to thank everyone that knows they contributed in such and include a personal message for each in their copy of this thesis.
My inspirators can be roughly divided into four categories. First, I had the blessing to meet a number of people that motivated me, for instance by helping me to overcome my fear of becoming a physicist and managing to get the best out of me. Second, the teachers, who brought me to learn, understand and implement the scientific method and taught me specific experimental or numerical techniques as well as some textbook physics I had not been educated in. On a more personal level, there were people that supported me with a lot of practical things. And finally the people that provided me with some great distractions at the critical moments where I just needed a moment to breathe and think about anything else but science.

Kobus, I remember approaching you as a master student, shyly asking your opinion about a 'life scientist' who wanted to drastically switch topics and aspired to become a PhD in a nanophotonics related field. You both motivated me to apply for a PhD in this direction, and took the risk by hiring me under your supervision. (In Amolf terms, you turned me from the 'bright' side into the the 'dark' one.) During my PhD you have pushed me over my limits, and as a result have cranked up my capabilities to get the impossible done, independently and well planned. After this baptism of

fire, nothing can scare me away. In addition, your perfectionism has made me a better writer, presenter and even storyteller. Thank you for these contributions. Lastly, a small apology for having exploited the lab as an atelier for my 'knutselprojectjes' voor de personeelsvereniging.
Being part of the NanoOptics group has enabled me to get deep into this research topic. Apart from the useful weekly meetings, all post-docs and particularly fellow PhDs were always willing to lend a hand in the lab and/or help with tricky data analysis. Furthermore, our joint adventures enriched the number of campfire stories I have in my repertoire. I would like to express my great appreciation to everybody that is or was part of this group and has supported me the past years.
Nir, as my daily contact, I believe we had an ideal agreement where we exchanged knowledge and insight for pretty pictures. Thanks for supporting me in making the output of our group more colorful and shiny. I would like to address that your moral support on my first few conference talks was important to me. Irina, Matthias and Boris, I'd like to thank you for our fruitful collaboration on near-field measurements of plasmonic nanowires, which lead to a nice publication and chapter 3 in this thesis. Irina, I also appreciate that you were willing to take a prominent role in one of the interviews with me on Dutch television.
A special thanks to all assistants, technicians, cleanroom, software and ICT specialists for the quick help whenever necessary. Hinco, apart from being our talented and smart group technician, you have helped me out with two important other things. I want to thank you for the entire catwoman construction you built around the optical table to make the setup more accessible for me. Second, without you I could not have made a life-sized meters long paper-maché dragon and let it fly free in the AMOLF hall. Another thing I can cross of my bucket list. Sabine and Esther, I owe both of you big time for assisting me the past years with some professional and personal challenges. Thank you for assisting Kobus and me in complying with PhD regulations. Proposition 11 is for you.
Ruben, we've been through quite some together and I am grateful for not having gone through all of it alone. It has been a turbulent time for both of us, which lead to some unforgettable memories I can write entire chapters about. I believe one of the most memorable experiences to me was that we indirectly ended up at the MT-meetings for hanging our secret painting of batman and superman behind an entire office window. At least now is revealed why paintings and posters spanning the office windows are no longer allowed at AMOLF. Aron, also with you I have had the pleasure to experience and share some great escapades. You were, likely, my most important teacher in the lab and have moreover helped me numerous times unraveling code mysteries. Besides work, we have also been on some adventures together. One unforgettable memory forced us in a hospital in Munich to figure out whose German was the least bad in a dire situation. To both of you, thank you for the help and support, the adventures, and also for being my paranymphs.
Lastly, I want to thank the bachelor and master students I have supervised on their research projects, Nicolaas, Dolfine and Oliver, for revealing the things I did not yet fully understand and lots of gezelligheid. It was a pleasure working with you.

I'm not the only one recognizing that AMOLF is a unique place, with warm and friendly people, qualified support staff always willing to help, and a large group of very talented and inspiring scientists. I would lie if I said I wasn't intimidated being a part of this group most of the time. Although intimidating, AMOLF creates a special type of family bond between colleagues, even after leaving the nest. I have experienced that ex-AMOLF colleagues have supported me - sometimes over great distances - up to the final point of proofreading chapters of this thesis and discussing ideas on cover designs. Likewise, after having partially left AMOLF myself I could count on new group members to check on typos. Those involved, I warmly acknowledge your support.
I've had an amazing time being part of the personeelsvereniging, which allowed me to organize the most creative events and unabashedly photoshop group leaders into Harry Potter characters, as well as fill AMOLF with some art and crafts. It feels strange to leave AMOLF after so many years, but I am glad that I did not fall far from the nest, and that my new colleagues at the FOM bureau already welcomed me with open arms.

This final paragraph I would like to dedicate to a special group of people, who stayed in close contact with me during the most isolating phases over the past years. I am truly thankful for the warmth, strength and love I have received. Together with my beloved animals, you have kept my oxytocin levels balanced. Thanks to my friends that joined me for climbing, (pole) dancing, rollerblading, mountain biking, concerts, dinners, music sessions, storytelling nights, and so on. Tot deze groep behoort ook mijn familie, en in het bijzonder mijn ouders, die me de afgelopen jaren vanuit alle vier de categorieën gesteund hebben, waarvoor mijn diepste dank. Dit boek is voor jullie.

Anouk de Hoogh